ISSN en trámite

Geofísica Internacional

Revista Trimestral Publicada por el Instituto de Geofísica de la Universidad Nacional Autónoma de México

México
Volume 52 Number 1
January- March
2013

— Geofísica Internacional —

GEOFÍSICA INTERNACIONAL, Año 52, Vol. 52, Núm. 1, enero - marzo de 2013 es una publicación trimestral, editada por la Universidad Nacional Autónoma de México, Ciudad Universitaria, Alcaldía Coyoacán, C.P. 04150, Ciudad de México, a través del Instituto de Geofísica, Circuito de la Investigación Científica s/n, Ciudad Universitaria, Alcaldía Coyoacán, C.P. 04150, Ciudad de México, Tel. (55)56 22 41 15. URL: http://revistagi.geofisica.unam.mx, correo electrónico: revistagi@igeofisica.unam.mx. Editora responsable: Andrea Rostan Robledo. Certificado de Reserva de Derechos al uso Exclusivo del Título: 04-2022-081610251200-102, ISSN: en trámite, otorgados por el Instituto Nacional del Derecho de Autor (INDAUTOR). Responsable de la última actualización Saúl Armendáriz Sánchez, Editor Técnico. Fecha de la última modificación: 31 de diciembre 2012, Circuito de la Investigación Científica s/n, Ciudad Universitaria, Alcaldía Coyoacán, C.P. 04150, Ciudad de México.

Geofísica Internacional

Vol. 52, Núm. 1, enero-marzo de 2013

Contents

Geofísica
Internacional

A possible case of Sporadic Aurora in 1843 from Mexico.

José Manuel Vaquero, María Cruz Gallego, Fernando Domínguez-Castro

Geofísica Internacional (2013) 52-1: 5-20

Original paper

Hydro-climatic variability and forest fires in Mexico's northern temperate forests

José Návar* and Liliana Lizárraga-Mendiola

Received: December 14, 2011; accepted: August 08, 2012; published on line: December 14, 2012

Resumen

Los cambios globales en las temperaturas pueden estar modificando el ciclo hidrológico de las cuencas forestales. Este reporte tuvo como objetivos estimar las variables del ciclo hidrológico interceptación, I, la evapotranspiración actual, E, y potencial, Et, la escorrentía, Q, y los cambios en el contenido del agua del suelo, θ; así como evaluar si las variables del ciclo hidrológico están presentando tendencias u oscilaciones que pudieran estar asociadas al calentamiento global en cuencas forestales del centro de Durango, México. El procedimiento del balance de masas sirvió para calcular las variables diarias del ciclo hidrológico con el uso de los sub-modelos de I y Et para evaluar finalmente la Q y θ. Los datos se sujetaron a un análisis de regresión y a técnicas auto-regresivas y de promedios móviles, ARIMA, para evaluar la significancia estadística de las tendencias. El valor acumulado del valor estándar de z magnificó y los modelos ARIMA proyectaron estadísticamente bien las oscilaciones mensuales y anuales de las variables del ciclo hidrológico. Las ecuaciones de regresión y las tendencias de los modelos ARIMA mostraron que las variables mensuales y anuales de P, I, E y Et, Q, y θ no siguen tendencias claras en tiempo con significancia estadística; éstas a su vez, siguen oscilaciones que pudieron ser predichas adecuadamente con modelos ARIMA. Se encontró una asociación consistente ($p \leq 0.05$) entre θ y el número de incendios y la superficie forestal incendiada a pesar de las diferentes escalas en las cuales se evaluaron estas variables. El análisis muestra que el calentamiento global está contribuyendo a incrementar la variabilidad hidrológica estacional al aumentar los pulsos de sequía y humedad en tiempo. Sin embargo, se requiere de investigaciones adicionales para probar esta hipótesis con el uso de series de tiempo más largas, con otro tipo de técnicas estadísticas y con la incorporación de otras variables en el análisis.

Palabras clave: análisis de regresión, modelos auto-regresivos con promedios móviles, precipitación, interceptación, evapotranspiración, escorrentía y contenido del agua del suelo, incendios forestales, plagas y enfermedades.

Abstract

Global warming is likely modifying the hydrological cycle of forested watersheds. This report set as objectives to: a) assess the hydrological variables interception loss, I, potential and actual evapo-transpiration, E, Et, runoff, Q, and soil moisture content, θ; b) evaluate whether these variables are presenting consistent trends or oscillations that can be associated to global warming or climate variability; and c) relate θ to the number of wildfires and the burned area in Durango, Mexico. A mass balance approach estimated daily variables of the water cycle using sub-models for I and Et to calculate Q and θ for a time series from 1945 to 2007. Regression and auto-regressive and moving averaging (ARIMA) techniques evaluated the statistical significance of trends. The cumulative standardized z value magnified and ARIMA models projected statistically similar monthly and annual time series data of all variables of the water cycle. Regression analysis and ARIMA models showed monthly and annual P, I, E, and Et, Q, and θ do not follow consistent up or downward linear tendencies over time with statistical significance; they rather follow oscillations that could be adequately predicted by ARIMA models ($r^2 \geq 0.70$). There was a consistent statistical association ($p \leq 0.05$) of θ with the number of wildfires and the area burned regardless of the different spatial scales used in evaluating these variables. The analysis shows seasonal variability is increasing over time as magnifying pulses of dryness and wetness, which may be the response of the hydrological cycle to climate change. Further research must center on using longer time series data, testing seasonal variability with additional statistical analysis, and incorporating new variables in the analysis.

Key words: regression analysis, autoregressive moving average models, precipitation, interception loss, evpo-transpiration, runoff, soil moisture content; forests fires, pests and diseases.

J. Návar*
Professor, Natural Resource Management
CIIDIR-IPN Unidad Durango
Sigma 119, Fracc. 20 de Noviembre II, 34220
Durango, Dgo., México
*Corresponding author: jnavar@ipn.mx

L. Lizárraga-Mendiola
Professor, Universidad Autónoma de Hidalgo
Departamento de Ingeniería Civil
Email: lililga.lm@gmail.com.

Introduction

Global warming by the continued build up of greenhouse gasses, GHG, in the atmosphere is predicted to lead to significant changes in climate (Ritter, 2009). The IPCC (2001; 2009) reported how Earth temperature has increased in the last century in contrast to the previous 200 years. Transient increasing temperatures of 0.6-0.8^{0}C in the last 150 years may already be magnifying climate as Held and Sodden (2006) predicted robust hydrological responses to global warming by additional increases of GHG in the atmosphere. In the present, instrumental records show increased precipitation of 0.5 to 1.0% per decade in much of the Northern Hemisphere mid and high latitudes; in contrast to the subtropics where rainfall has decreased during the 20th Century by 0.3% per decade (Folland *et al*., 2002).

Forests, as oceans regulate and buffer climate changes at the expenses of increased pressure. The world forests influence climate through physical, chemical, and biological processes that affect planetary energetics, the hydrologic cycle, and atmospheric composition. The complex and non-linear forest-atmosphere interactions are issues widely studied since these connections can be dampened or amplified (Bonan, 2008). The effect of regional warming and consequent increases in water deficits as likely contributors to the pervasive boost in tree mortality rates of forests of western United States is one issue of these interactions recently reported (van Mantgem *et al*., 2009). Recent drought-related and warming has also been implicated as contributing to pulses or episodes of regional forest dieback such as those caused by bark beetle outbreaks in southwestern North America (Breshears *et al*., 2005; Raffa *et al*., 2008) and northern Mexico (SEMARNAT, 2005). Increased pulses of wildfire activity in the Rocky Mountains temperate forests has also been associated to increased spring and summer temperatures (Westerling *et al*., 2006).

Forest fuels, heat and oxygen are necessary for a fire to burn. Ground (organic soil, duff, and moss), slash (litter), living trees and miscellaneous (grass) are classifications of forest fuels (Reinhardt and Crookston, 2003). Drought desiccates all kinds of fuels; living fuels, large dead fuels, deep duff layers, and organic soils and it has an obvious effect on wildfires; spread rates and fire intensities. Intense wildfires occur when drought and frosts happen continuously since these perturbations add large amounts of young foliage onto the soil; and the burn probability increased with the presence of young fuels in Portugal (Fernandes *et al*., 2012).

In northern Mexico, increased tree mortality rates have not been documented so far. However, significant pulses of wildfire events have been recorded during the last three decades (SEMARNAT, 2005). Although these pulses of tree mortality have been associated to drought elsewhere, there is no information on the drought episode itself, its magnitude, frequency, and how it could be related to global or regional warming. Large wildfires in the region are believed to have increased in extent, frequency, magnitude and duration due to the likely effect of land-tenure changes and the suppression of frequent light fires (Fulé and Covington, 1997; Drury and Veblen, 2008) although the potential effect of global warming cannot be ruled out. Consensus has been that increasing temperatures causing soil dryness beyond normal thresholds are responsible for the pervasive tree mortality rates as well as for tree mortality by wildfire activity. However no evidence of soil dryness and its magnitude has ever been reported.

In spite of this information, little research has gone toward determining whether environmental changes are contributing to chronic, long-term shifts in variables of the hydrological cycle as an aid to quantify water deficits in Mexico's northern temperate forests in order to assess global warming impacts. Neither has the water deficit issue been documented in the region and associated to global warming-related events. Since forests regulate the hydrological cycle by redistributing precipitation; climatological drought reported as a reduction of precipitation in contrast to its mean value is different than soil water deficit that is the most important variable for tree survival and dieback. Therefore, this report aimed at: a) evaluating the variables of the hydrological cycle daily interception loss, potential and actual evpotranspiration, runoff and soil moisture content; b) assessing whether the mean values of these variables in addition to instrumental precipitation and pan evaporation are transiently changing over time; c) relating large-scale climatic events to wildfires, and d) associating assessments of soil moisture content to wildfires in a forested watershed near El Salto, Durango, Mexico.

The hypothesis tested was that variables of the hydrological cycle do not follow consistent trends in dryness or water deficits. If the null hypothesis is rejected, then these findings suggest forests of Northern Mexico are under increasing drought-related stress that could lead to the potential increased continuous mortality rates as those observed in western North America by van Mantgem *et al*. (2009). The acceptance of the null hypothesis would lead to the conclusion that cycles or oscillations in hydrological variables cause forest stress that produce pulses of tree mortality such as those noted by increased wildfire activity reported by Breshears *et al*. (2005) in southwestern U.S.A as well as those observed for

the studied Mexico's northern temperate forests (SEMARNAT, 2005). Both types of disturbances can happen simultaneously but they have never been reported in Mexico's northern temperate forests. The forest ecosystem responses to climate change must be understood and reported as an aid to potentially convey sustainable practices to buffer climate change and/or variability impacts on forests.

Materials and Methods

Description of the study area

This study was conducted at the watershed 'La Rosilla', which drains into the 'La Rosilla II' reservoir; both located at the Ejido La Victoria, Municipality of Pueblo Nuevo, Durango, Mexico. The watershed covers an area of 944 ha and spans 23° 44´ 00" north latitude and 105° 27´ 00" west longitude, at the southwestern portion of the Sierra Madre Occidental mountain of Durango, Mexico (Figure 1).

The watershed sits within the Hydrologic Region No 11 (Presidio-San Pedro), in the uplands of the Rio Presidio basin. The main stem of the river is named Arroyo Quebrada El Salto, a tributary of the Rio Presidio (CFE, 1998).

La Rosilla watershed features several microclimates, according to the Köppen climatic classification scheme and modified for Mexico by García (1987): a) in the highlands, the temperate-cold, humid climate, with summer rains and mean annual temperature between 5 to 12°C is classified as C(E)(W_2); the rest of the ejido presents a temperate, humid climate with summer rains, and mean annual temperature ranging from 12 to 18°C. Summer rains are characterized by thunderstorms concentrated between July to September. Mean annual rainfall depth and temperature at the climatic station of El Salto is approximately 900 mm and 9.3°C.

Most of the watershed is covered by temperate forests with mixtures of pines, oaks, and other conifers. Main distributed pine species are *Pinus cooperi*, *P. durangensis, P. engelmannii, P. teocote, P. herrerae, P. leiophylla* and *P. ayacahuite*. The most frequent oak species observed are *Quercus sideroxyla*, *Q. durifolia, Q. rugosa* and *Q. candicans*. *Juniperus* spp., *Cupressus* spp., *Pseudotsuga* spp. and *Abies* spp. are other temperate conifer species that make up the forest community within the watershed. Other broad leaf species found within these forests are *Arbutus* spp and *Alnus* spp. The lower strata are conspicuous and dominated by manzanita (*Arctostaphylos pungens*) and encinilla (*Quercus striatula*).

The hydrological model to evaluate its components

The components of the water cycle in the forested watershed used a model based on the mass balance approach (Návar, 2008). The model physically computes changes in θ as a function of the difference between inputs and outputs (model 1). Input is P and outputs are I, Et (transpiration, T, and evaporation of water from the soil, Es) and Q (surface runoff and leakage to aquifers); see Equations (1), (2), (3), (4), and (5). This model assumes that θ above field capacity leaks down into shallow perched water tables that eventually transforms into discharge via subsurface, surface, and aquifer discharge. The intrinsic assumption is

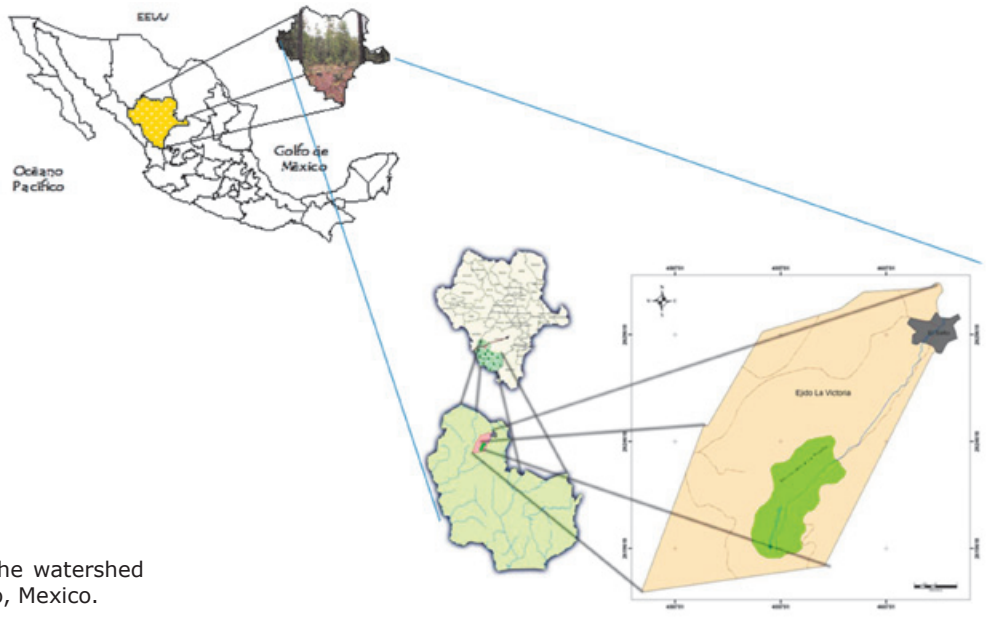

Figure 1. Location of the watershed "La Rosilla" Durango, Mexico.

that there is little or no Hortonian surface runoff, and it appears to be correct for most forested soils for most of the time, since high average final infiltration rates of the order of close to 130 mm h^{-1} had been measured (Dueñez *et al*., 2006). Only 7% of the rains that occur annually and close to 30% of rains that have a frequency of a two-year return period produces surface runoff in Mexico's northern forested watersheds (Dueñez and Návar, 2005; Dueñez *et al*., 2006).

$$E - S = \frac{\partial A}{\partial t}; E = P \quad (1)$$

$$S = (I + Ev + Tr + Qs + Qp); Et = (Ev + Tr) \quad (2)$$

$$P - (I + Et + Qs + Qp) = \frac{\partial A}{\partial t} \quad (3)$$

$$Q = Qs + Qp; \quad (4)$$

$$Q = P - (I + Et) \pm \frac{\partial A}{\partial t} \quad (5)$$

Precipitation, P, is conventionally recorded in rain gauges set at the climatic station El Salto, Dgo., Mexico. Leakage, percolation, or deep infiltration, Qs, equals to discharge, Q, since surface runoff, Qs ≈ 0. Interception loss is the amount of rainfall that wets canopies and litter (foliage, bark, and litter) and returns to the atmosphere via evaporation without contributing to soil moisture.

The revised Gash analytical model (Gash *et al*., 1995; Valente *et al*., 1997) was used to predict I since it is simple, flexible, and requires few parameters that can be easily derived. The model has been reformulated to give a better description of the evaporation flux from sparse forests and appropriately tested for forests of northeastern temperate forests (Návar, 2012). Gash *et al*. (1995) introduced the following analytical model of rainfall interception (6):

$$\sum_{j=1}^{n+m} I_j = n(c)P'_G + (c\bar{E}_c / \bar{R})\sum_{j=1}^{n}(P'_{Gj} - P'_G) + (c)\sum_{j=1}^{m} P_{GJ} + qS_c + p_t \sum_{j=1}^{n-q} P_{GJ} \quad (6)$$

Where: $\underline{I}$ is the interception loss depth, $\underline{m}$ is the number of small storms insufficient to saturate the canopy (e.g., < $\underline{P'_G}$), $\underline{n}$ equals the number of events which saturate the canopy (e.g., > $\underline{P'_G}$) and $\underline{q}$ equals the number of storms which saturate the stems, $\underline{P_{Gj}}$ is gross rainfall, $\underline{st}$ is the trunk storage capacity, $\underline{pt}$ is the proportion of rainfall reaching the trunks, $\underline{P'_G}$ is amount of rainfall necessary to fill the canopy storage capacity.

$$P'_G = -\frac{\bar{R}Sc}{\bar{E}c}\ln\left[1 - \frac{\bar{E}c}{\bar{R}}\right] \quad (7)$$

Where: $\underline{\bar{E}c}$ = the evaporation rate during the storm per unit area of cover, $\underline{Sc}$ = the canopy storage capacity per unit area of cover, R = the average rainfall rate onto the canopy.

The coefficient and parameter values for the Gash revised analytical model used in this research are reported in Table 1.

Table 1. Coefficient and parameter values for the reformulated Gash analytical model of rainfall interception for temperate forests of northeastern Mexico (Source: Návar, 2011; 2012).

	Statistics	
Parameters	Average	Confidence Interval
S	1.0272	0.5196
C	0.9500	0.9500
Sc	1.0813	0.5469
A	0.0848	0.0277
R	12.6500	4.4200
Ec	1.0191	0.1163
Pt	0.0068	0.0006
St	0.0037	0.0029
St/pt	0.5441	5.1250
P'G	1.1273	0.5543

Evapo-transpiration, Et, is the amount of water that leaves the soil via evaporation from the soil surface, Ev, and via transpiration, Tr, as a vital process conducted by plants. An estimator of Et is measured in conventional pan evaporimeters; and it is named potential evaporation because water is fully available for climate to evaporate. Actual evapo-transpiration, Etp, is the evapo-transpiration weighted by soil moisture content (θi), plant (Ftv), and climatic (Fc) factors. For example, soil factors that control Etp are the current soil water content, θi, the soil water content at wilting point, θpmp, and the soil water content at field capacity, θcc. The plant factor

is a function of the type of vegetation, density, age, etc. The climatic factor is controlled by evapo-transpiration. Actual evapo-transpiration is estimated using these factors as in equation (8):

$$Et = \frac{Ln\left[100 * \frac{\theta_i - \theta_{pmp}}{\theta_{cc} - \theta_{pmp}}\right]}{Ln(101)} * E * Fc * Ftv \quad (7)$$

Details of the soil, plant and climatic factors can be found in several hydrology and soil physics books (Hillel, 1982; Viessman *et al*., 2007). In this study, twelve soil samples were collected and distributed within the watershed for laboratory analyses to estimate the field capacity, wilting point, soil bulk density, and soil specific density. On site, the depth of soil and litter layer was also measured. The coefficient and parameter values for the soil components of sub model 8 are reported in Table 2.

Where: ASNM = Altitude above sea level (m); P = slope (%), PMO = depth of litter layer (mm); PS = depth of soil (cm); DA = soil bulk density (g cm^{-3}); DR = soil specific density (g cm^{-3}); CC = field capacity (%); PMP = wilting point (%).

The model was run in a time difference of one day to estimate the current soil moisture content; e.g., $\theta_i = \theta_{i-1} \pm$ [Precipitación $_{i-1}$ – Intercepción $_{i-1}$ – Etp_{i-1} – Q_{i-1}]. Where: the $_{i-1}$ refers as the day before day i. Again, discharge was estimated as the soil moisture content that runs off and that is mathematically described as the amount of soil moisture content above field capacity and this amount of water is subtracted immediately to attain the soil water content at field capacity. Since at this time there is a lack of information on the shape and rate of recession flow, the time of concentration, time to peak, peak flow, etc., hydrographs cannot be derived at this point with this model.

Information to develop the reformulated interception loss model of Gash was obtained from measurements conducted on mixed, pine-oak temperate forests of Nuevo Leon, Mexico by Návar (2011; 2012). The climatic factor, Fc, was estimated to be 0.75 in agreement with findings carried out by Penman (1986). The plant factor, Ftv, was estimated to be 1.25.

The mass balance model (1) has been indirectly validated by associating thresholds of the number of days below certain soil moisture content with the number of wildfires and the area

Table 2. Soil physical parameters of soil samples collected in "La Rosilla" watershed of Durango, Mexico (Source: Silva-Flores, 2007).

Site No	N Latitude	W Longitude	ASNM (m)	P (%)	PMO (mm)	PS (cm)	DA (g/cc)	DR (g/cc)	θCC (%)	θPMP (%)
1	23° 43' 19.2''	105° 25' 02.2''	2728	25	45	32.0	0.77	2.28	61.17	32.71
2	23° 43' 21.9''	105° 25' 55.3''	2660	15	30	30.0	0.76	2.13	65.03	34.77
3	23° 43' 19.5''	105° 25' 55.5''	2658	30	8	7.0	0.83	2.25	40.65	21.73
4	23° 43' 06.8''	105° 25' 21.5''	2739	5	52	16.0	0.83	2.20	46.01	24.60
5	23° 43' 04.2''	105° 25' 18.0''	2727	40	60	11.5	0.78	2.25	52.11	27.86
6	23° 43' 01.1''	105° 25' 16.0''	2703	50	20	24.3	1.00	2.24	33.69	18.01
7	23° 42' 52.1''	105° 24' 57.1''	2815	15	35	43.0	0.81	2.27	68.62	36.69
8	23° 42' 54.4''	105° 24' 57.4''	2807	5	32	41.5	0.76	2.28	59.84	32.00
9	23° 42' 46.7''	105° 25' 07.0''	2797	5	35	10.0	0.75	2.29	47.94	25.63
10	23° 42' 43.6''	105° 25' 15.2''	2783	2	30	23.0	0.76	2.20	58.50	31.28
11	23° 43' 02.2''	105° 24' 59.2''	2715	30	33	7.5	0.77	2.27	48.85	26.12
12	23° 43' 12.8''	105° 24' 50.3''	2706	2	25	5.0	1.00	2.23	33.96	18.16
Average			2736	19	34	20.9	0.82	2.24	51.36	27.46
Standard Deviation			53.64	16.17	13.86	13.46	0.82	0.05	11.60	6.20
Confidence Interval (α=0.05)			30.351	9.150	7.840	7.613	0.050	0.026	6.565	3.511

burned by wildfires with very good degree of precision (Návar-Cháidez, 2011). In this report, further validation of this model is provided using the burned area and the number of forest wildfires as dependent variables and the average soil moisture content as the dependent variable. Návar (2008) also calculated daily, monthly and annual discharge into "La Rosilla II" reservoir with good preliminary expectations since accountability was precise by quantifying for changes in reservoir storage, losses to deep recharge, evaporation, and supply. At this time, there are no measurements of soil moisture content, interception, or discharge in the studied watershed, therefore the model could not be directly checked and validated.

Data analysis

Daily measurements and assessments of precipitation, interception loss, potential and actual evaporation, runoff, and soil moisture changes summed or averaged over a month or over a year provided monthly and yearly measurement and assessments of each variable. Conventional regression analysis using least square techniques tested the hypothesis for trends; e.g., Y = a + bX; where Y = is the variable of the hydrological cycle and X is just a consecutive number (1 to 756 for monthly or 1945 to 2007 for annual data); a, B are statistical parameters to be estimated using SAS v 8.1. The null hypothesis that B = 0 was tested; if Ho is true then no statistical significant tendencies are shown by the variable. That is, the time series is stationary in its first momentum. In addition, ARIMA models fitted to monthly and annual data statistically tested for trends. Monthly and annual hydrologic data variables were smoothed using a moving average of t=3; then the ARIMA models were fitted to this data set. The Southern Oscillation Index, SOI, an index of the El Niño/Southern Oscillation, ENSO, was related to the variables of the hydrological cycle using regression analysis.

The magnification of variability

In order to magnify oscillations or cycles, the data was analyzed by accumulating the standardized z parameter as in model (8):

$$\int_{i=1}^{n}\left(\frac{x_i-\overline{x}}{\sigma}\right)\cdot\partial i=\sum_{i=1}^{1}z_1\ for\ t=1;$$

$$for\ t=2;\sum_{i=1}^{2}z_1+z_2;$$

$$\sum_{i=1}^{n}z_1+z_2+...+z_n \qquad (8)$$

Where: x_i = the hydrological variable at time t=i; $\overline{x}$= mean value of the hydrological variable; σ = the standard deviation of the hydrological variable of interest.

Procedure

The variables of the hydrological cycle were estimated with model (1), (2), (3), (4), (5), (6), and (7). Regression analysis and ARIMA models tested the hypothesis that B = 0. ARIMA models fitted the data for prediction purposes in addition to detect patterns and oscillation on the hydro-climatic data. The cumulative z departures magnified oscillations and cycles. Hydro-climatic cycles and oscillations were then associated to pulses of disturbances on forests such as increasing wildfire events; as well as to the ENSO related events such as the SOI. Trends could then likely be associated to pervasive perturbations such as continuous forest dieback or increased tree mortality rates in Mexico's northern temperate forests.

Results

Regression equations

The slopes, standard errors, F values and probabilities larger than F for all regression equation are shown in Table 3.

Where: S error= standard error; F = value of the Fisher F density function; P>F = probability calculated from the F value to the infinite; Eta = actual evapo-transpiration.

For the regression equations, all probability data had values larger than 0.05; therefore the null hypothesis (e.g., B = 0) was accepted for monthly and annual data. That is, the slope values statistically approached a value of 0. Hence, the hydrological variables do not show consistent up or down monotonic linear trends or tendencies in the mean value that can be linked to continuous global warming or climate change that can be further related to increasing forest disturbances for the study period (1945-2007). The effect of climate change may be on shifts of the frequency and magnitude of these variables; on the second momentum (the variance); in the magnitude of pulses or dryness and wetness, etc. However, at this time there is not sufficient information to test these other indications of climate change. The mean monthly and annual P, I, E and Et, Q, and θ values remain quite constant throughout the study period. Probabilities of between $0.12 \leq P>F \leq 0.19$ were estimated for annual Q, annual Et, annual I and annual P.

The statistics for the best fitted ARIMA models with a trend are depicted in Table 4.

Table 3. Statistics of regression equations between hydrological variables and annual (n=64) or monthly (n=756) continuous values.

	Monthly Data				Annual Data			
Variable	Slope	S Error	F	P > F	Slope	S Error	F	P > F
Precipitation	0.0136500	0.013500	1.02	0.31	2.6279	1.6879	2.42	0.12
Interception	0.0014900	0.001480	1.02	0.31	0.2866	0.1846	2.41	0.13
Evaporation	0.0006700	0.004778	0.02	0.88	0.7886	0.9296	0.72	0.40
Actual Eta	0.0048000	0.006090	0.62	0.43	1.0446	0.7326	2.04	0.16
Runoff	0.0000350	0.000031	1.32	0.25	0.0060	0.0040	1.75	0.19
Soil Moisture Content	0.0000094	0.000013	0.52	0.47	0.0001	0.0001	0.54	0.47

Table 4. Quality statistics for best ARIMA models fitted with monthly (n=756) and annual (n=64) hydrologic variable data for a Mexico's northern temperate forest site.

	Monthly Data				Annual Data			
Variable	Model	R_2	Sx	P > t	Model	R_2	Sx	P > t
Precipitation	ARIMA(3,0,1)	0.88	26.8	0.26	ARMA(3,0,1)	0.61	76.2	0.72
Interception	ARIMA(3,0,3)	0.90	2.32	0.11	ARMA(3,0,1)	0.61	8.34	0.73
Actual Eta	ARIMA(2,0,1)	0.91	9.20	0.42	ARMA(2,0,0)	0.51	33.1	0.65
Runoff	ARIMA(3,0,1)	0.69	0.07	0.21	ARMA(2,0,1)	0.64	0.64	0.72
Soil θ.	ARIMA(3,0,0)	0.83	0.02	0.49	ARMA(2,0,1)	0.58	0.0008	0.40

Where: SX = standard error; R^2 = coefficient of determination; P > t = probability calculated from the t value to the infinite for the linear trend of each model; Eta = Actual evapo-transpiration; θ. = Moisture content; ARIMA = auto-regressive integrated with moving average models with a linear trend; (n, 0, p) = number of auto-regressive and moving average parameters, respectively with a lack of seasonal tendencies, 0.

For all ARIMA models, the probability larger than t was > 0.05. Therefore, ARIMA models did not account for statistical significant linear trends or tendencies. However, the linear trend improved quality statistics of all models that it is useful for prediction purposes. Most models required only 2 or 3 auto-regressive and 1 moving average parameter to fit data well. The variance explained by the models (e.g., the R^2) was larger for monthly, with a mean value of 0.84 than for annual (R^2 = 0.59) data. That is, ARIMA models fitted better monthly than annual data perhaps because of the number of data values (n = 756 for monthly and n = 64 for annual data) or the consistent seasonal variability in the monthly data sets.

Raw hydrologic, smoothed and modeled data are depicted in Figure 2 for monthly and in Figure 3 for annual data for precipitation, interception loss, actual evapo-transpiration, runoff and soil moisture content, respectively.

The ARIMA models for annual data did not fully display variability because they predict the smoothed time series. However, oscillations and cycles are well noted in the annual and monthly time series, respectively. The magnification of cycles and oscillations are better observed in Figure 4.

Cycles and oscillations describe the data better than linear trends or tendencies in the hydrological variable datasets. The intra and inter-annual variability can be observed by the up and downs of all hydrological variables in Figures 2, 3, and 4. For example for precipitation, the dry season (November-May) repeats itself every year. The inter-annual variability is noted because it takes on the average every 1, 2 or sometimes 3 years annual precipitation to repeat itself. That is, larger or smaller figures than the average are expected every 1, 2 or 3 years.

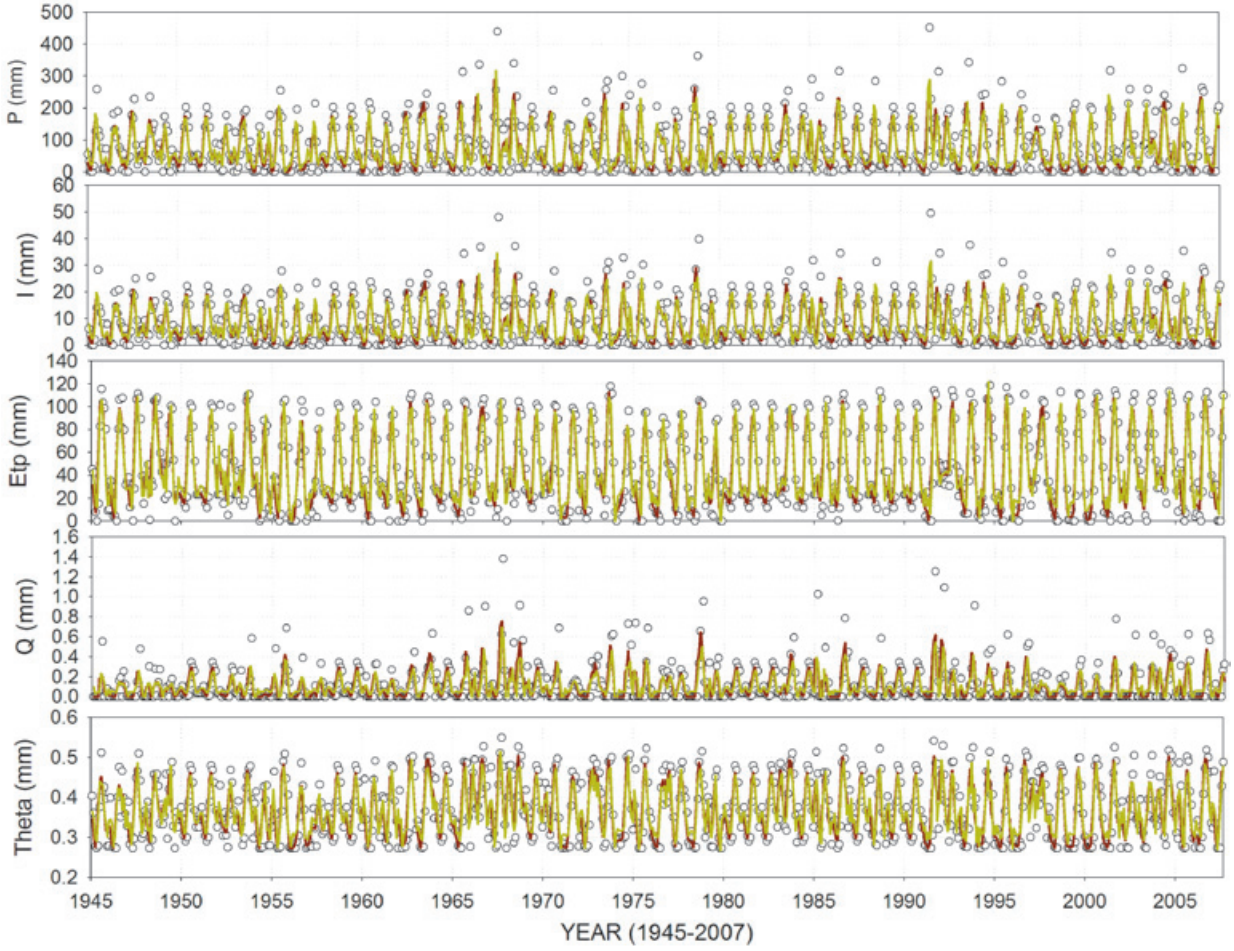

Figure 2. Monthly data values, smoothed series, and ARIMA models for predicting precipitation (P), interception loss (I), actual evapo-transpiration (Etp), runoff (Q), and soil moisture content (Theta) for a Mexico's northern temperate forest site (Note: brown dark lines are smoothed raw data and brown light lines are ARIMA models).

The decadal drought episode of the 1950's (1945-1963) is well depicted in all these time series of Figures 3 and 4 because of a consistent reduction in precipitation, interception loss, and runoff. Actual evapo-transpiration and soil moisture content show the large dry effect of the 1950's was dampened a few years later, from 1955-1962. The 1990's drought spell is observed in precipitation, interception loss and runoff. Actual evapo-transpiration remains quite constant during this period and soil moisture content diminishes from 1987-1997 and from 1998 to 2004. Longer time scale oscillations that ended and started somewhere between 1963-1965 are noted in these time series. However, information for longer time series is required to verify these potential cycles. The water deficit expressed as soil moisture content below the average does not appear to show well defined temporal cycles beyond the intra-annual variability. However, well defined downward tendencies in different time periods (1950's, early 1980's, early 1990's, and from 1993-2004) and of different duration (9, 4, 3, and 11) are observed in Figure 4.

Time series for the 1945-2005 dry season (January-May)

The annual time series of the hydrological variables for the dry season (January-May) is depicted in Figure 5.

The mean soil moisture content values attain a figure very close to the wilting point (0.27 cm cm^{-1}) during 1994-1996 and 1998-2001 (Figure 5). Quite wet soil moisture content during the dry seasons is found during 1949-1952; 1966-1970; 1980-1985. Years 1992 and 1997 had high unseasonal soil moisture content immersed within a prolonged drought during the dry season. Precipitation, actual evapo-transpiration, and runoff were quite small during 1974-1977; 1988-1991; 1993-1996; and 1998-2001. On the other side, potential evapo-transpiration and the difference between Etp-Eta showed high values during these last time periods.

The number of days with soil moisture content values smaller than 0.30 or 0.35 showed upward

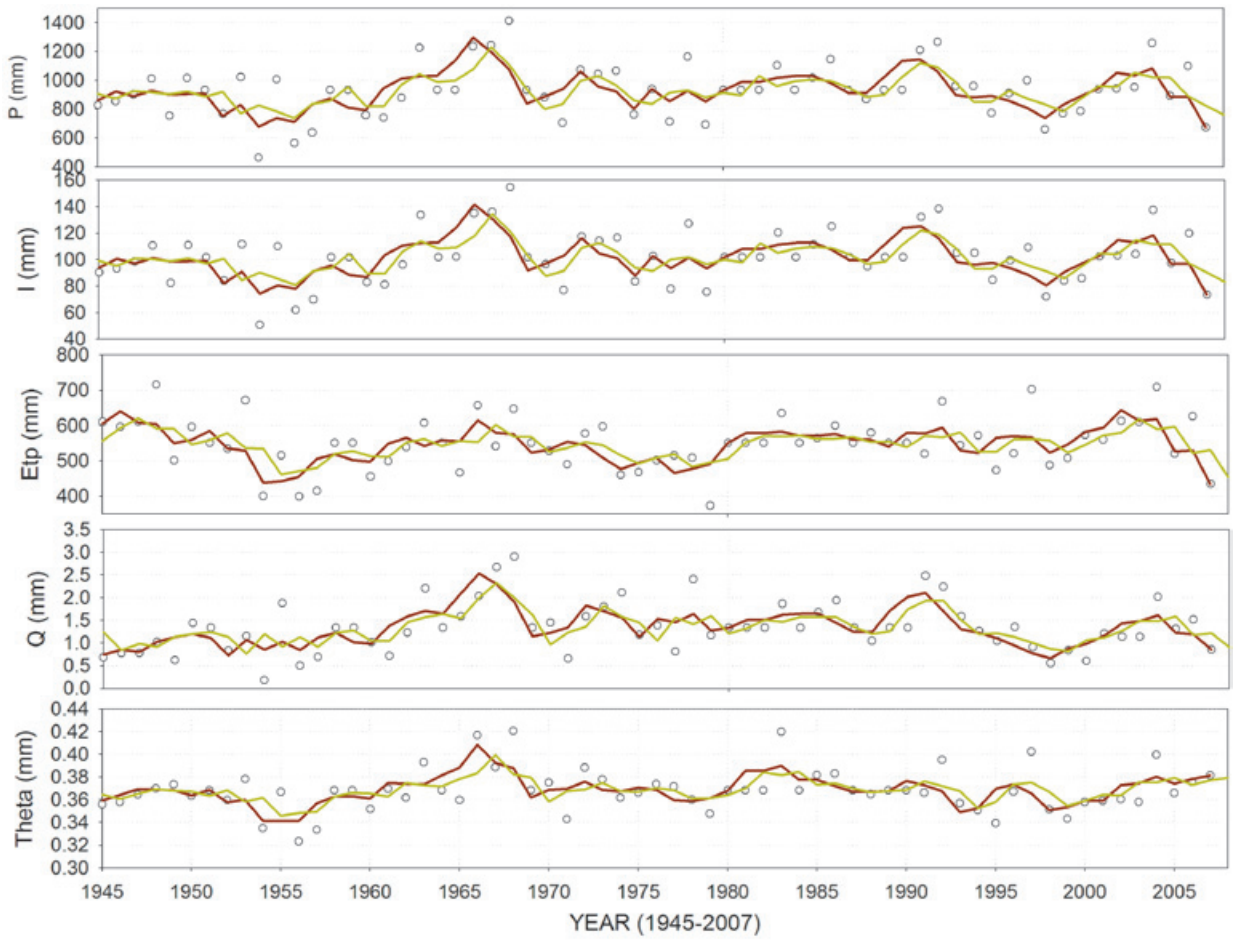

Figure 3. Annual data values, smoothed series, and ARIMA models for predicting annual precipitation (P), interception loss (I), actual evapo-transpiration (Etp), runoff (Q), and soil moisture content (Theta) for a Mexican northern temperate forest site (Note: brown dark lines are smoothed raw data and brown light lines depict ARIMA models).

tendencies across time but with no statistical significance (p=0.42 and p=0.34, respectively). However, the number of runoff events is statistically increasing over time (p=0.038). A value of θ = 0.30 cm cm^{-1} is quite close to the wilting point for these forest soils, that is, θ_{pmp} = 0.27 cm cm^{-1} (Table 2). Soils with moisture content near the wilting point (θ = 0.30 cm cm^{-1}) persisted during the 1990's. In eight years, the number of days with 0.30 cm cm^{-1} was larger than 105 out of 151 for the period of 1998-2001, more than 122 days out of 151 had soil moisture content values smaller than 0.30 cm cm^{-1}. This is a drought spell lasting four consecutive years with soils near the wilting point during most of the dry season.

Associating soil moisture content to wildfires

The area burned by forest wildfires and its predicted exponential decaying 3-parameter function are depicted in Figure 6. The equation projects a large burned area (e.g., > 30,000 ha) with soil moisture content near the wilting point; a sharp decrease in burned area with increased soil moisture content until it reaches a steady, constant burned area with θ ≥ 0.32. Average soil moisture content values during the dry season accounts for by 43% of the total burned area variation in the State of Durango, Mexico. The soil moisture content near the wilting point (e.g., < 0.30 cm cm^{-1}) produce a mean burned area of close to 30,000 ha while soil moisture contents of between 0.32 ≤ θ ≤ 0.41cm cm^{-1} produce only a mean burned area of close to 5,000 ha. A lack of biomass density on top of soils, sources of ignition, or a combination of both may have accounted for by the small area burned by forest fires in soils near the wilting point.

The number of forest wildfires also decays as a function of soil moisture content, although the variance accounted for by the equation was only 33% (Figure 6). Two sets of data can be observed in Figure 6; the first one for more than

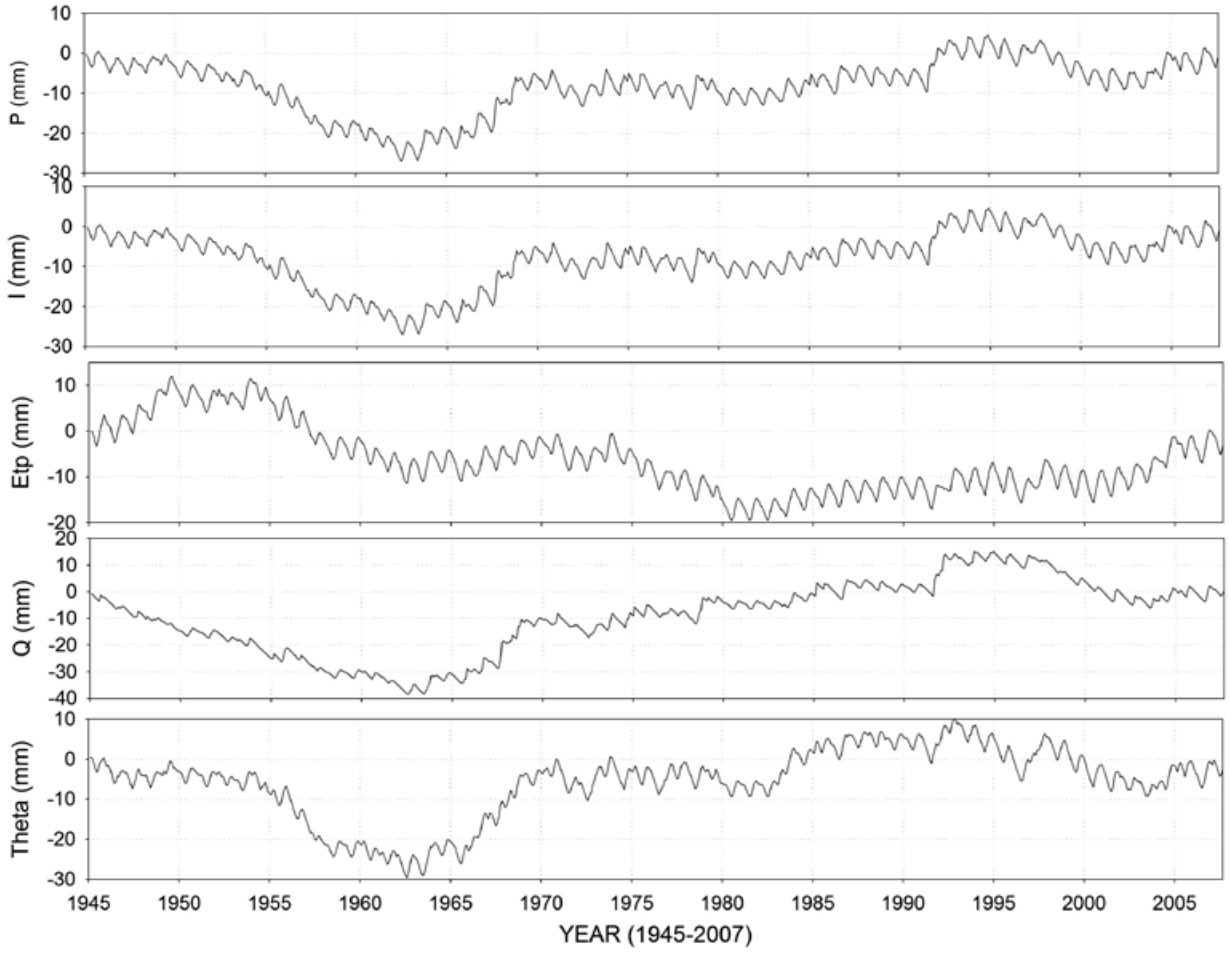

Figure 4. Cumulative standardized deviations of monthly data for precipitation (P), interception loss (I), actual evapo-transpiration (Etp), runoff (Q), and soil moisture content (Theta) for a Mexico's northern temperate forest site.

300 wildfires and the second one for less than 230 wildfires. The former data set has a quite small ($\theta \leq 0.30$ cm cm^{-1}) and the later one has a large soil moisture content variability ($0.28 \leq \theta \leq 0.41$ cm cm^{-1}). Other sources of information such as wind speed, direction, the amount of biomass on the forest floor, ignition sources, etc. may account for fewer fires per unit time during dry soil moisture conditions in the second data set.

Climate variability and its association to wildfires

Spectral density analysis, autocorrelograms and cumulative standardized deviations on hydro-climate variables showed statistically significant peaks ($p \leq 0.05$) at three time scales; 1-2; 3-7; and 9-11 years. The annual Southern Oscillation Index, SOI, was significantly associated to dry seasonal values for soil moisture content ($r^2=0.08$; $p=0.05$), precipitation ($r^2=0.11$; $p=0.02$), interception loss ($r^2=0.11$; $p=0.02$), actual evapo-transpiration ($r^2=0.108$; $p=0.02$), and the difference between Et and Etp ($r^2=0.12$; $p=0.02$). The first four variables had negative slopes unlike the last one. Smaller soil moisture content, precipitation, interception loss, and actual evapo-transpiration and larger Et-Etp values are expected with the presence of El Niño/Southern Oscillation. La Niña/Southern Oscillation produces the opposite effect, according to the regression equations. Although this association is statistically significant, the amount of variation explained by these synoptic climatic phenomena is less than 12% leaving a great deal of unexplained variation.

The PDO raw data did not predict well dry seasonal soil moisture content ($p=0.11$), precipitation ($p=0.14$), interception loss ($p=0.14$), pan evaporation ($p=0.11$), actual evapo-transpiration ($p=0.11$), runoff ($p=0.29$) unlike the difference between pan evaporation and actual evapo-transpiration, Et-Etp ($p=0.03$). The PDO produces a negative effect in the Et-Etp values; in contrast to the El Niño/Southern Oscillation phenomenon. That is, these two

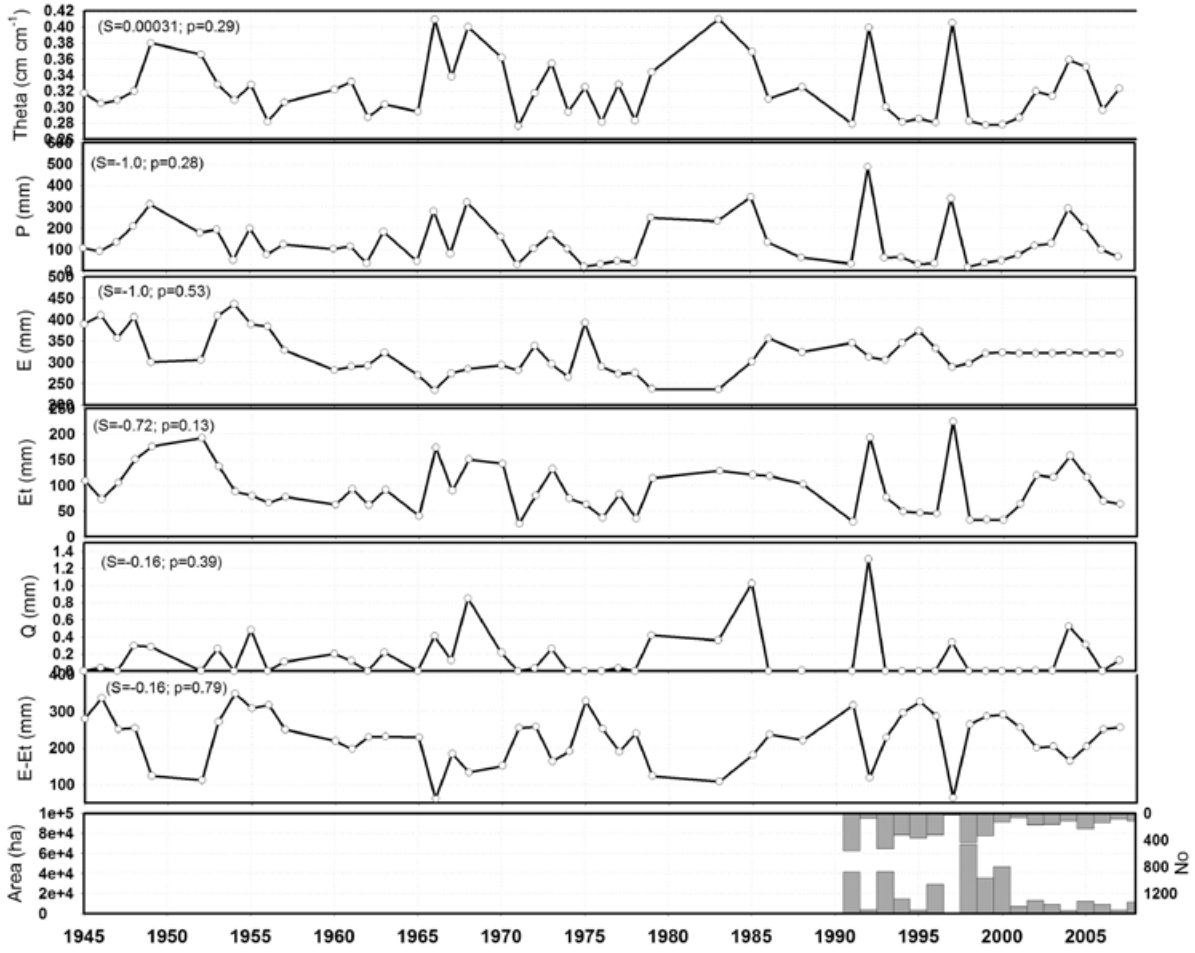

Figure 5. Time series of hydrological variables during the dry season (January-May) for a forest site near El Salto, Durango, Mexico (Note: P = precipitation; I = interception loss; Eta = actual evapo-transpiration; Q = runoff; Theta = soil moisture content). Note the Man-Kendall sen slope value and its probability is also depicted within each figure.

climatic phenomena appear to somehow offset each other during the 1945-2007 studied time series.

The combined effect (ENSO, PDO) was not statistically significant for dry seasonal soil moisture content (p=0.10), precipitation (p=0.06), interception loss (p=0.06), unlike for actual evapo-transpiration (p=0.05), and the difference between Et-Etp (p=0.03). The ENSO is negatively related and the PDO is positively related for the first four variables and the inverse is correct for the difference between Et-Etp, respectively. Positive values of El Niño/Southern Oscillation and negative values of PDO reduce the soil moisture content, precipitation, interception loss, and significantly reduce actual evapo-transpiration but increase the difference ET-Etp.

Discussion

A lack of statistical significant trends or tendencies in mean values of variables of the hydrological cycle is consistent across instrumental and estimated data sets. This finding show the mean value of the studied hydrological variables with these techniques appears be only slightly related to the effect of global warming over time since the probability was near 0.10 for the annual time series. A different approach to test the effect of global warming on the hydrological variables is by relating it to the variance, the frequency and shifts in the magnitude of these variables. Climate change may dampen its effect as pulses of change of different magnitude and time interval since forests and oceans may regulate and buffer this effect. These are issues that require further study. For example, dry pulses can be observed at the temporal scales; seasonal, inter-annual, every 3-7 years; and every 10-13 years and likely every 70-80 years. Further studies on the frequency, magnitude, and intensity of these pulses may shed more light into the effect of global warming on hydro-climate variables at El Salto, Durango, Mexico.

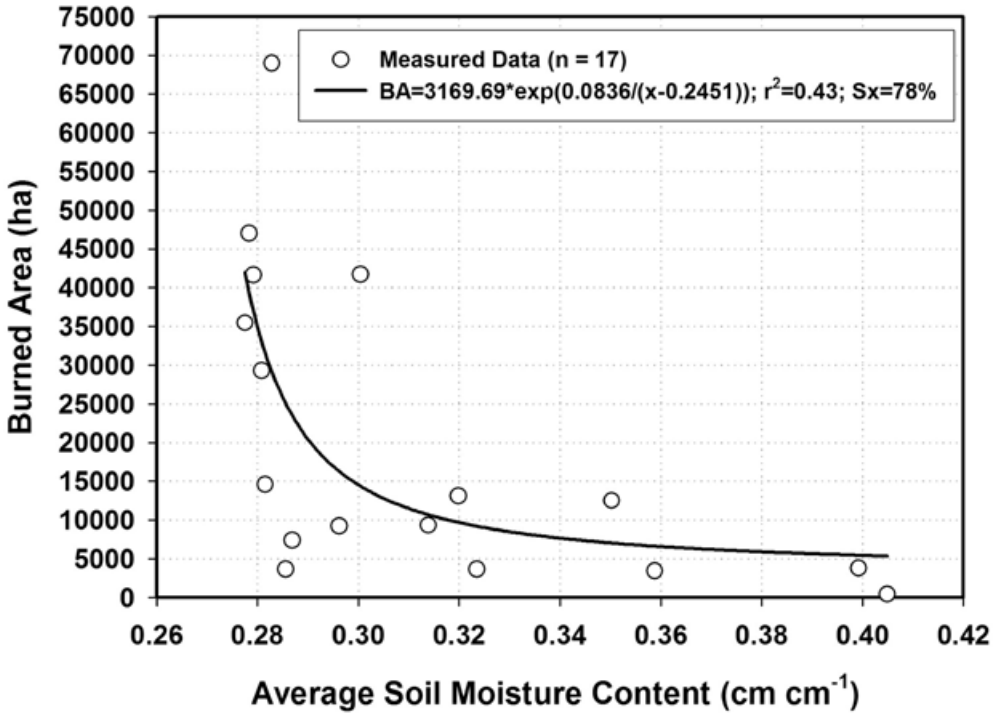

Figure 6. The measured and predicted area burned by forest wildfires as a function of seasonal soil moisture content in the State of Durango, Mexico for the period of 1990-2007.

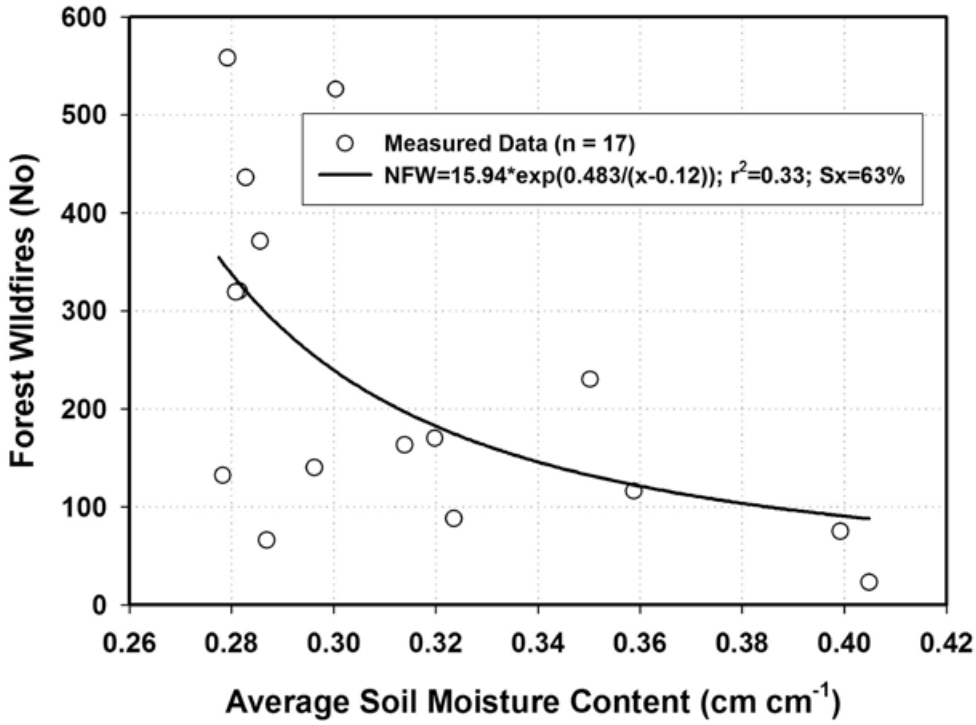

Figure 7. The measured and predicted number of forest wildfires as a function of seasonal soil moisture content for a forest site near EL Salto, Durango, Mexico.

A simple argument would then be that the number of observations is a shortcoming for testing correctly the hypothesis B = 0. For example, for the annual variables precipitation, interception loss, and weighted actual evapo-transpiration the probability of rejecting the null hypothesis was close to 10%. That is, in the near future the hypothesis of no shifts in the mean values would probably be rejected as more hydro-climatic data is recorded. A second approach to increase the number of observations is to reconstruct paleoclimate by using several techniques, amongst which dendrochronology is an important methodology for this case studies (Cleaveland *et al*., 2003; Stahle *et al*., 1999; González-Elizondo *et al*., 2005; Návar-Cháidez, 2012).

The pervasive continuous forest decline or increased rates of forest loss as those found over western North America by van Mantgem *et al*. (2009) are explained by regional warming and consequent continuous increases in water deficits. Data analysis for this report shows the 1990's reported more frequent water deficits in Mexico's northern temperate forests than any other time recorded in this analysis. Further data will show if this dry pulse would repeat itself in the near future as a more important sign of climate change. In the meantime, continuous tree mortality rates have not been recorded in the region, independent sources of data such as the volume of harvested dead trees shows also a lack of statistical significant linear trends over the years for the State of Durango, Mexico (SEMARNAT; 2005). A large pulse of harvested dead trees was recorded during 2002 and the future would also tell whether this record breaks as a consequence of magnified pulses of dryness by climate change.

Soil moisture content is probably the best indicator of water deficit in forests because of its regulating effect on the hydrological cycle. This variable is the single most important one to assess how trees can be potentially stressed by droughts. Pan evapo-transpiration and the difference between Et-Etp, on the other hand are likely the best indicators of global warming as water evaporation is a function of temperature. None of these variables showed consistent linear tendencies or trends in the mean values of this data set that can be straightforwardly associated to global warming. Pulses of up and downward cycles or oscillations were the norm in this case study.

The hydrological variables studied showed instead short term tendencies or oscillations that can be associated to pulses of tree mortality by increased wildfire activity as those recorded for southwestern North American dry forests by Breshears *et al*. (2005) and Mexico's northern temperate forests during later last and early this century (SEMARNAT, 2005); as it has been also observed for other ecosystems as well (Raffa *et al*., 2008). In Durango, Mexico, large-scale (> 40000 ha) forests wildfires in number and area burned occurred during 1989, 1991, 1993, 1995, 1996, 1998, 1999, and 2011 for the period of 1970-2011 (SEMARNAT, 2012). Years 1998 and 2011 recorded the largest area (> 70000 ha) burned by wildfires in type, number and area burned. Years 1998 and 2011 reported the driest years in terms of soil moisture content, the later one with close to 250 consecutive days with 0 precipitation. The former one with an average soil moisture content of 0.28 cm cm^{-1} and approximately 10% of likelihood of occurrence in the number of dry days (127 and 151 out of 151) with soil moisture content values near the wilting point (e.g., of less than 0.30 and 0.35 cm cm^{-1}, respectively), and seasonal precipitation was the smallest ever recorded (18 mm) during the dry season (January-May). Wildfire events of 1998 and 2011 would probably have been magnified by the antecedent and widespread frosts that recorded below -15^{0}C in the region. Frosts of this magnitude make trees shed their leaves in a time-scale of weeks and kills herbaceous understory fuels that carry large fires. All this litter-foliage provides an important dry biomass source for starting fires. In addition, the wildfires of 1998 were combined with strong Pacific Ocean dry winds that hit the country in most of late winter and spring of 1998 (CNA, 1998).

The following three years (1999, 2000, and 2001) remained consistently dry (Figure 5) during the dry season; with a mean value of 0.28 cm cm^{-1}; with less than 18% of probability of the occurrence of these events and number of days with less than 0.30 and 0.35 cm cm^{-1} was more than 122 days per each year, a statistic well above the average. By the year 2000, seasonal actual evapo-transpiration reached one of the smallest values ever recorded (32.6 mm) because of a lack of soil moisture content to evapo-transpirate soil water. This translates that almost always soils were close to the wilting point and left little or no soil water for evapo-transpiration during the dry season. The stress caused by this dry episode (1998-2001) was sufficient to weaken trees and to make them prone for bark beetle outbreaks that spread all over the Mexico's temperate forests. Note that this hydrological study was conducted on a specific site near El Salto, Durango, Mexico. However bark beetle infested simultaneously much of the Mexico's northern forests in a reported area of close to 50,000 ha stressing the importance of large scale perturbations that can be monitored at short spatial scales. It is important to note that during the period of 1993-1996, the number of dry years during the dry season was also above the average with 1997 being the only wet year in between these two dry episodes (only 6 and 34 days reported θ values < 0.30 and 0.35 cm cm^{-1}, respectively).

The drought spell of the 1990's appeared to be stronger than that of the 1950's. For the later decade, the number of dry days was just on the average number of dry days for the entire time series, close to 90. Only 1956 and 1957 reported n > 108 dry days. Breshears *et al*. (2005) for southwestern North American woodlands reported extensive bark beetle infestations in 2002-2003 and stressed that it was also highly likely that this last episode may have had warmer conditions than the drought episode of the 1950's. Preliminary analysis of this data for Durango, Mexico shows that the 1950's and the 1990's had 353 and 320 mm and 250 and 243 mm of potential evapo-transpiration and Et-Etp, respectively, indicating the former drought spell was warmer than the second one. The 1950's drought spell was less dry than that of the 1990's. However, this is a matter of further study with this and other additional sources of information.

Large-scale climatic events causing these oscillations and potential tendencies have been well documented in the last two to three decades. Although the inter-annual variability requires additional sources of information in order to be more explicitly described; the annual position of the Bermuda High in the North Atlantic Ocean combined with the northward seasonal displacement of the Inter-tropical Convergence Zone, ITCZ, may partially control this variability.

The second dry-wet cycle (3-7 years) correlates well with indices of El Niño/Southern Oscillation, ENSO, as it has been found for other places and datasets (Cavazos and Hastenrath, 1990; Cleaveland *et al*., 2003; Stahle *et al*., 1999; Méndez-González *et al*., 2008). Hydrological data for this study exhibits statistically significant spectral peaks in the ENSO frequency band near periods of 4 years as it has been found for instrumental and proxy precipitation records of Durango, Mexico as well (Stahle *et al*., 1999). In northern Mexico, the ENSO causes severe and prolonged summer droughts and wet winters (Cavazos and Hastenrath, 1990; González-Elizondo *et al*., 2005) with total reduced annual rainfall and it has a direct control on all variables of the hydrological cycle as well. For example during the decade of the 1990's two ENSO events occurred (1992 and 1998) with the second one being the strongest of the last century.

The third quasi decadal discharge dry-wet variability is evident in all ARIMA models, spectral density analysis, as well as in the hydrological variable data sets. The northeastern Pacific Ocean cooling - warming cycle, called the Pacific Decadal Oscillation, PDO, appears to be slightly related to this phase for northern Mexico (Jones, 2003). Quasi-decadal sequences repeated in the time series and ARIMA models during the 1950's and 1990's. The cooling of the northeastern Pacific Ocean surface waters brings above average rainfall and discharge to northern Mexico (Návar-Cháidez, 2012). The PDO effect has also been noted in Utah although its control is not consistent over time and appears insignificant during periods of instrumental recorded data (Tingstad and MacDonald, 2010). Weak associations between annual discharge and PDO variability can be explained since the latter manifests mostly in the North Pacific region and can persist over several decades. Mantua *et al*. (1997) described periods of 15-25 years and 50-70 years and dry spells last at the most 15 years (1950's) for this time series data.

Longer time-scale climatic events are also causing oscillations and likely tendencies in the hydrological variables studied that appeared to end and start during 1963. The Atlantic Multidecadal Oscillation, AMO, is a climate pattern of SST anomalies in the North Atlantic with a recurring period of 65-80 years (Knight *et al*., 2006). Positive AMO index values have been associated with drought in the continental U.S. during the 20th Century (Enfield *et al*., 2001). This cycle appears to control all hydrological variables when calculating and plotting the cumulative Z index time series data (Figure 4). However, instrumental precipitation data and evaluated variables are not sufficient at this time to statistically correlate this tendency.

The future decadal drought spell would occur likely under warmer temperature and probably under dryer soil moisture conditions as potential climate change progresses and larger, magnified pulses of drought-induced vegetation die-off could be expected as explained by Breshears *et al*. (2005) for southwestern U.S.A. Increased dieback pulses would be the temperate forest ecosystem response to drought and associated increased wildfire activity; since the number of dry days near the wilting point ($\theta \leq 0.30$ cm cm^{-1}) is steadily increasing over time during the dry season as well. The number of runoff events is also statistically increasing over time, then, potential climate change would appear is erratically increasing seasonal hydrological variability in the region as it has been also reported for other places but this is a matter of further studies.

Conclusions

This report analyzed variables of the hydrological cycle of a Mexico's northern forested watershed using a mass balance model; tested whether these mean values of these variables are transiently changing over time or changes obey to climate variability oscillations of different magnitudes and durations; and associated hydrological variables, large-scale climate events, and forest wildfires

in the region. Regression techniques and ARIMA models provided a better understanding of these changes and how they are associated to recent forest wildfires that have spurred into the region. Long-term linear trends or tendencies in mean values were absent in the studied time series, and oscillations of different magnitude and duration featured these data sets (1945-2007). Soil water deficits or drought spells could then be associated to forest fires that occurred in the last two decades. Future research may center on how these drought spells are controlling tree growth in such a way that eventually growth slows leading to the weakening of trees and finally to promoting die-off by wildfires.

Acknoeledgemnts

I would like to thank M.C. Ramon Silva F. for his help at excavating soil samples in the La Rosilla II watershed. This research was funded by the IPN through research grant given to J. Návar during 2012. The author is a COFAA scholar.

Bibliography

Bonan G.B., 2008, Forests and climate change: forcing, feedbacks, and the climate benefits of forests. *Science,* 320, 5882, 1444-1449.

Breshears D.D., Cobb N.S., Rich P.M., Price K.P., Allen C.D., Balice R.G., Romme W.H., Kastens J.H., Floyd M.L., Belnap J., Andeson J.J., Myers O.B., Myere C.W., 2005, Regional vegetation die-off in response to global-change-type drought. Proc. Natl. Acad. Sci. U.S.A., 102, 15144, 1599-1612.

Cavazos T., Hastenrath S. 1990, Convection and rainfall over Mexico and their modulation by the Southern Oscillation. *International Journal of Climatology,* 10, 377-386.

CFE, Comisión Federal de Electricidad, 1998, Manifiesto de Impacto Ambiental Modalidad General de La Presa La Rosilla II. Elaborado en convenio con CNA. Durango, México.

Cleaveland M.K., Stahle D.W., Therrell M.D., Villanueva-Diaz J., Burns B.T., 2003, Tree-ring reconstructed winter precipitation and tropical teleconnections in Durango, Mexico. Climate Change, 59, 369-388.

CNA, Comisión Nacional del Agua. 1998. Condiciones climáticas en la República Mexicana durante 1998, México, D.F.

Drury, S.A., Veblen T.T., 2008, Spatial and temporal variability in fire occurrence within the Las Bayas Forestry Resesrve, Durango, Mexico. Plant Ecology, 197, 299-316.

Dueñez-Alanís J., Navar J., 2005, Estimación de la frecuencia y magnitud de los escurrimientos superficiales en bosques de coniferas de Durango. Divulgación 4, 6, 42-43.

Dueñez-Alanís J., Gutiérrez J., Pérez L., Návar J., 2006, Manejo silvícola, capacidad de infiltración, escurrimiento superficial y erosión. Terra Latinoamericana, 24, 233-240.

Einfield D.B., Mestas-Nuñez A.M., Trimble P.J., 2001, The Atlantic Multidecadal Oscillation and its relationship to rainfall and river flows in the continental U.S. Geophysical Research Letters 28, 10, 2077-2080.

Fernandes P.M., Loureiro C., Magalhaes M., Ferreira P., Fernandes M., 2012, Fuel age, weather and burn probability in Portugal. International Journal of Wildland Fire http://doi.org/10.1071/WF10063.

Folland CK., Karl TR., Salinger M.J., 2002, Observed climate variability and change. Weather 57: 269-278.

Fulé P.Z., W.W., Covington, 1997, Fire regimes and forest structure in the Sierra Madre Occidental, Durango, Mexico. Acta Botánica Mexicana, 41, 43-79.

García E., 1987, Modificaciones al sistema de clasificación climática de Köppen (adaptación a la Republica Mexicana). 4ª. Edición, D.F. 130 p.

Gash J.H.C., Lloyd C.R., Lachaud G., 1995, Estimating sparse forest rainfall interception with an analytical model. Journal of Hydrology 170, 79-86.

González-Elizondo M., Jurado E., Návar J., González-Elizondo M.S., Villanueva J., Aguirre O., Jiménez J., 2005, Tree-rings and climate relationships for Douglas-fir chronologies from the Sierra Madre Occidental, México: a 1681-2001 rain reconstruction. Forest Ecology & Management 213: 39-53.

Held IM., Soden B.J., 2006, Robust responses of the hydrological cycle to global warming. Journal of Climate Change, 19, 5686-5699.

Hillel D., 1980, Fundamentals of Soil Physics. Academic Press Ltd. London. U.K.

IPCC, Intergovernmental Panel on Climate Change. 2001. Impacts, adaptation, and

vulnerability. Summary for Policy Makers. Cambridge University Press. Cambridge, UK. 17 pp.

IPCC, Intergovernmental Panel on Climate Change, 2009, Impacts, adaptation, and vulnerability. Summary for Policy Makers. Cambridge University Press. Cambridge, UK. 17 pp.

Jones D.L., 2003, El Niño, PDO, climatic cycles and drought in the Sierra Nevada. El Dorado County Water Agency. Water Resources Development and Management Plan. California. USA.

Knight J.R., Folland C.K., Scaife A.A., 2006, Climate impacts of the Atlantic Multidecadal Oscillation. *Geophysical Research Letters* 33:LI7706, doi: 10.1029/2006GL026242.

Mantua N.J., Hare S.R., Zhang Y., Wallace J.M., Francis R.C., 1997, A Pacific interdecadal climate oscillation with impacts on salmon production. Bulletin of the American Meteorological Society 78: 1069-1079.

Méndez-González J., Návar-Cháidez J.J., González-Ontiveros V., 2008, Análisis de tendencias de precipitación (1920-2004) en México. Investigaciones Geográficas 65: 38-55.

Mulholland PJ., Best, GR., Coutant CC., Hornberger GM, Meyer JL., Robinson PJ., Stemberg JR., Turner RE., Vera-Herrera F., Wetzel RG. 1997. Effects of climate change on freshwater ecosystems of United States and the Gulf of Mexico. Hydrological Processes 11: 949-970.

Návar J., 2008, Atlas Hidrológico del Estado de Durango. Inedito. 220 p.

Návar J., 2011, Stemflow variation in Mexico's northeastern forest communities: its contribution to soil moisture content and aquifer recharge. *Journal of Hydrology*, 408: 35-42.

Návar J., 2012, The performance of the reformulated Gash's interception loss model in Mexico's northeastern temperate forests. Hydrological Processes. DOI: 10.1002/hyp.9309.

Návar-Cháidez J.J., 2011, Modelación del contenido del agua de los suelos y su relación con los incendios forestales en la Sierra Madre Occidental de Durango, México. Madera y Bosques 17: 65-81.

Návar-Cháidez J.J., 2012, Modeling annual discharge for six Mexico's northern rivers. Ambiente & Agua. An Interdisciplinary Journal. doi:10.4136/1980-993X.

Penman H.L., 1986, Natural evaporation from open water, bare soils and grass. Proc. Roy. Soc. London A (194), S. 120-145.

Raffa K.F., Aukema B.H., Bentz B.J., Carroll A.L., 2008, Cross-scale drivers of natural disturbances prone to anthropogenic amplification: the dynamics of bark beetle eruptions. *Bioscience* 58, 501, 507-521.

Ritter S.K., 2009, Global warming and climate change. Chemical and Engineering News 87: 11-21.

SEMARNAT, Secretaria del Medio Ambiente y Recursos Naturales. 2005. Informe de la situación de los Incendios Forestales en México. http://portal.semarnat.gob.mx/semarnat/portal.

Stahle D.W., Cleaveland M.K., Therrell M.D., Villanueva-Díaz J., 1999, Tree ring reconstruction of winter and summer precipitation in Durango, Mexico, for the past 600 years. In: 10th Symposium Global Change Studies. American Meteorological Society. Dallas, p 205-211.

Tingstad A.H., MacDonald G.M., 2010, Long-term relationships between ocean variability and water resources in northeastern Utah. Journal of the American Water Resources Association 46, 5, 987-1002.

Valente F., David J.S., Gash J.H.C., 1997, Modelling interception loss for two sparse eucalypt and pine forests in Central Portugal using reformulated Rutter and Gash analytical models. *Journal of Hydrology* 190, 141-162.

Van Mantgem P., Stephenson N.L., Byrne J.C., Daniles L.D., Franklin J.F., Fulé P., Harmon M.E., Larson A.J., Smith J.M., Taylor A.H., Veblen T.T. 2009, Widespread increase of tree mortality rates in the western United States. *Science* 323, 521-524.

Viessman W.J., Lewis G.L., Knapp J.W., 2007, Introduction to Hydrology. Fourth Edition. Harper & Row. New York. USA: 780 p.

Westerling A.L., Hidalgo H.G., Cayan D.R., Swetnam T.W., 2006, Warming and earlier spring increase western US forest wildfire activity. *Science* 313, 5789, 940-943.

Geofísica Internacional (2013) 52-1: 21-30

Original paper

Scholte waves on fluid-solid interfaces by means of an integral formulation

Manuel Carbajal-Romero, Norberto Flores-Guzmán*, Esteban Flores-Mendez, Jaime Núñez-Farfán, Enrique Olivera-Villaseñor and Francisco José Sánchez-Sesma

Received: December 28, 2011; accepted: October 02, 2012; published on line: December 14, 2012

Resumen

El presente trabajo muestra la propagación de ondas de interfaz de Scholte en la frontera de un medio acústico (fluido) en contacto con un medio sólido elástico, para una gama amplia de materiales sólidos. Se ha demostrado que mediante un análisis de ondas difractadas en un fluido, es posible inferir las propiedades mecánicas del medio sólido elástico, específicamente, sus velocidades de propagación. Con este fin, el campo difractado de presiones y desplazamientos, debido a una onda de presión inicial en el fluido, son expresados empleando representaciones integrales de frontera, las cuales satisfacen la ecuación de movimiento. La fuente en el fluido es representada por una función de Hankel de segunda especie y orden cero. La solución a este problema de propagación de onda es obtenida por medio del Método Indirecto de Elementos Frontera, el cual es equivalente al bien conocido teorema de representación de Somigliana. La validación de los resultados se lleva a cabo usando el Método del Número de Onda Discreto y el Método de Elementos Espectrales. Primeramente, presentamos espectros de presiones que ilustran el comportamiento del fluido para cada material sólido considerado, después, mediante la aplicación de la Transformada Rápida de Fourier se presentan resultados en el dominio del tiempo, mediante simulaciones numéricas que muestran la emergencia de las ondas de Scholte.

Palabras clave: propagación de ondas, interfases fluidas-sólidas, ondas de Scholte, elementos frontera, ondas de interfaz, Funciones de Green.

Abstract

The present work shows the propagation of Scholte interface waves at the boundary of a fluid in contact with an elastic solid, for a broad range of solid materials. It has been demonstrated that by an analysis of diffracted waves in a fluid it is possible to infer the mechanical properties of the elastic solid medium, specifically, its propagation velocities. For this purpose, the diffracted wave field of pressures and displacements, due to an initial wave of pressure in the fluid, are expressed using boundary integral representations, which satisfy the equation of motion. The source in the fluid is represented by a Hankel's function of second kind and zero order. The solution to this wave propagation problem is obtained by means of the Indirect Boundary Element Method, which is equivalent to the well-known Somigliana representation theorem. The validation of the results is carried out by using the Discrete Wave Number Method and the Spectral Element Method. Firstly, we show spectra of pressures that illustrate the behavior of the fluid for each solid material considered, then, we apply the Fast Fourier Transform to show results in time domain. Snapshots to exemplify the emergence of Scholte's waves are also included.

Key words: wave propagation, fluid-solid interface, Scholte's waves, boundary elements, interface waves. Green´s functions.

M. Carbajal-Romero
E. Flores-Mendez*
Instituto Politécnico Nacional, México D.F., México.
**Corresponding author: efloresm@ipn.mx*

N. Flores-Guzmán
Centro de Investigación en Matemáticas, Jalisco s/n, Mineral de Valenciana, Guanajuato, México.

J. Núñez-Farfán
Instituto Mexicano del Petróleo, Eje Central Lázaro Cárdenas 152, Gustavo A. Madero 07730, México D.F., México.

E. Olivera-Villaseñor, F.J. Sánchez-Sesma.
Instituto de Ingeniería, UNAM, Circuito Escolar s/n, Coyoacán 04510, México D.F., México.

Introduction

The study of waves that propagate in the interface of a fluid medium and an elastic solid has its origins in the pioneering work of J. G. Scholte (1942 and 1947), and therefore, this kind of waves are known as Scholte waves. This interface wave is one of the three basic types of interface waves presented in isotropic media; sharing this classification with Rayleigh and Stoneley waves, for interfaces between vacuum-solid and solid-solid media, respectively (Rayleigh, 1885; Stoneley, 1924).

For interface waves, the concentrated energy is located at the interface and decreases exponentially with depth. However, energy decrement rate versus distance is less than for compressional and shear waves (Meegan *et al.*, 1999). This concentration of energy has enormous implications in some areas of physics and engineering. For example, Rayleigh waves are extensively studied in the earthquake engineering and seismology due to their catastrophic effects during strong seismic motions.

Some other applications for particular cases have been reported by Biot (1952), Ewing *et al.* (1957), Yoshida (1978a, 1978b), they focused mainly on the understanding of the interface waves at the ocean bottom. Specific features about wave propagation at interfaces, such as attenuation, layered medium behavior, porosity, etc., have been studied by Mayes *et al.* (1986), Nayfeh *et al.* (1988), Eriksson *et al.* (1995), Wang *et al.* (2004), and Gurevich *et al.* (2006).

In the field of numerical methods for studying this phenomenon, various formulations designed to model complex interface configurations and more realistic cases have been developed. Some of these include: Finite Element (Zienkiewicz *et al.* 1978), Finite Difference (van Vossen *et al.*, 2002; Thomas *et al.* 2000), Boundary Element (Godinho *et al.* 2001; António *et al.*, 2005; Rodríguez-Castellanos *et al.*, 2010), Spectral and pseudo Spectral Element Methods (Komatitsch and Barnes, 2000; Carcione and Helle, 2004; and Carcione *et al.*, 2005), among others.

In this paper we extend the use of the Indirect Boundary Element Method (IBEM) to study interfaces of water in contact with a wide range of solid materials, frequently used in engineering. Here, the emergence of interface waves is pointed out. This numerical technique is based on an integral representation of the stress, pressure and displacement wave fields, which can be considered as a numerical implementation of the Huygens's principle, which is equivalent, mathematically speaking, to the Somigliana's representation theorem.

The results are expressed in both time and frequency domains. The materials considered in the analysis, characterized by their wave velocities and densities, represent a wide range of materials used in engineering. In the following, the main equations used to develop the IBEM and the Discrete Wave Number Method (DWN) are summarized. Results from both formulations match satisfactorily.

Brief description of the indirect boundary element method

Equation of motion and incident fields of pressures and displacements

If we assume that the equation that governs the wave propagation in the fluid is given by the well-known equation of motion, then:

$$\frac{\partial \sigma_{ij}(\mathbf{x})}{\partial x_j} = \rho_F \frac{\partial^2 u_i(\mathbf{x})}{\partial t^2}, i,j = 1,3 \tag{1}$$

Where: ρ_F=density of the fluid. If we consider that stresses in the fluid are related to the pressure generated by the incident pulse, subsequently, one can express this last equation as:

$$\sigma_{ij}(\mathbf{x}) = -p^{0^F}(\mathbf{x})\delta_{ij}, i,j = 1,3. \tag{2}$$

Therefore, the displacement field in the fluid can be represented by its well-known form:

$$u_n^{0^F}(\mathbf{x}) = \frac{1}{\rho_F \omega^2} \frac{\partial p^{0^F}(\mathbf{x})}{\partial n} \tag{3}$$

The incident pulse at the fluid, as shown in Fig. 1a (inset), can be given as:

$$p^{0^F}(\mathbf{x}) = C(\omega) H_0^{(2)}\left(\omega\, r / c^F\right)$$

where $p^{oF}(\mathbf{x})$=incident pulse at the fluid, $\mathbf{x} = \{x_1, x_3\}$, $C(\omega)$=scale factor for the incident pulse, $H_0^{(2)}(\bullet)$=Hankel function of second kind and zero order, ω=circular frequency, c^F=compressional wave velocity in the fluid and $r=r(\mathbf{x})$ is the distance from the receiver to the source.

Integral representation for diffracted wave fields

To represent the diffracted wave fields (for pressures and displacements) in the fluid due to the incident pulse impacting the solid medium

(elastic solid wall), we suggest the following integral representations:

$$p^{d^F}(\mathbf{x}) = \int_{\partial F} G^F(\mathbf{x},\xi)\,\Psi(\xi)\,dS_\xi \qquad (5)$$

$$u_n^{d^F}(\mathbf{x}) = c_1\Psi(\mathbf{x}) + \frac{1}{\rho_F\omega^2}\int_{\partial F}\frac{\partial G^F(\mathbf{x},\xi)\Psi(\xi)dS_\xi}{\partial n} \qquad (6)$$

where,

$$G^F(\mathbf{x},\xi) = \frac{\rho\omega^2}{4i}H_0^{(2)}\left(\omega r/c^F\right) \qquad (7)$$

$\Psi(\bullet)$=force density for the fluid, $G^F(\bullet)$= Green function for the fluid, and c_1 defines the region orientation and can assume a value of -0.5, 0 or 0.5 (see explanation for c_2, given below).

The whole pressure and displacement fields in the fluid, besides, free and diffracted one, can be expressed, respectively, by:

$$p^F(\mathbf{x}) = p^{0^F}(\mathbf{x}) + p^{d^F}(\mathbf{x}), \qquad (8)$$

$$u_n^F(\mathbf{x}) = u_n^{0^F}(\mathbf{x}) + u_n^{d^F}(\mathbf{x}). \qquad (9)$$

Since the source is only applied to the fluid, it is expected that, in the solid, only diffracted waves will appear and they can be established as follows.

Consider a domain *V*, bounded by the surface *S*. If this domain is occupied by an elastic material, the displacement field under harmonic excitation can be written, neglecting body forces, by means of the single-layer boundary integral equation as follows:

$$u_i^d(\mathbf{x}) = \int_{\partial S} G_{ij}(\mathbf{x},\xi)\,\phi_j(\xi)\,dS_\xi, \qquad (10)$$

where $u_i(\mathbf{x})$=*i*-th component of the displacement at point $\mathbf{x}$, Gij($\mathbf{x};\xi$) = Green's function, which is the displacement produced in the direction *i* at $\mathbf{x}$ due to the application of a unit force in direction *j* at point ξ, ϕ is the force density in direction *j* at point ξ (the subscripts *i*, *j* are restricted to be 1 or 3 and the summation convention is applied, *i.e.* a repeated subscript implies summation over its range, 1 and 3 in this case). This integral representation can be obtained from Somigliana's identity (Sánchez-Sesma, 1991).

This integral representation allows the calculation of stresses and tractions by means of the direct application of Hooke's law and Cauchy's equation, respectively, except at boundary singularities, that is, when $\mathbf{x}$ is equal to ξ on surface *S*. From a limiting process based on equilibrium considerations around an internal neighborhood of the boundary, it is possible to write, for $\mathbf{x}$ on *S*,

$$t_i^d(\mathbf{x}) = c_2\phi_i(\mathbf{x}) + \int_{\partial S} T_{ij}(\mathbf{x},\xi)\phi_j(\xi)dS_\xi, \qquad (11)$$

where $t_i(\mathbf{x})$ is the *i-th* component of traction, c_2=0.5 if $\mathbf{x}$ tends to the boundary *S* "from inside" the region, c_2=-0.5 if $\mathbf{x}$ tends *S* "from outside" the region, or c_2=0 if $\mathbf{x}$ is not at *S*. $T_{ij}(\mathbf{x};\xi)$ is the traction Green's function, that is to say, the traction in the direction i at a point $\mathbf{x}$, associated to the unit vector $n_i(\mathbf{x})$, due to the application of a unit force in the direction *j* at ξ on *S*. The two-dimensional Green's functions for an unbounded space can be found in (Rodríguez-Castellanos *et al.*, 2007; and Ávila-Carrera *et al.*, 2009).

Boundary Conditions

In the IBEM is convenient to divide the domain into two regions (*S* for the solid and *F* for the fluid), in which proper boundary conditions that represent the problem under consideration have to be established. These boundary conditions for fluid-solid interfaces can be expressed as:

$$u_3^S(\mathbf{x}) = u_3^F(\mathbf{x}), \forall\mathbf{x}\in\partial S = \partial F, \qquad (12)$$

$$t_1^S(\mathbf{x}) = 0, \forall\mathbf{x}\in\partial S, \qquad (13)$$

$$t_3^S(\mathbf{x}) = -p^F(\mathbf{x}), \forall\mathbf{x}\in\partial S. \qquad (14)$$

Writing the boundary condition (12) as function of the diffracted field (10) for the solid and incident (3) and diffracted (6) fields for the fluid, we obtain:

$$\int_{\partial s} G_{3j}^S(\mathbf{x},\xi)\phi_j(\xi)dS_\xi = \frac{1}{\rho_F\omega^2}\frac{\partial p^o(\mathbf{x})}{\partial r}\frac{\partial r}{\partial x_3} + c_1\Psi(\mathbf{x}) + \int_{\partial F}\frac{\partial G^F(\mathbf{x},\xi)}{\partial x_3}\Psi(\xi)dS_\xi, \quad \forall\mathbf{x}\in\partial F = \partial S. \qquad (15)$$

The condition traction free (13) can be expressed from the integral form (11), obtaining,

$$c_2 \frac{1}{2}\phi_i(\mathbf{x}) + \int_{\partial S} T_{1j}^S(\mathbf{x},\xi)\phi_j(\xi)dS_\xi = 0, \forall \mathbf{x} \in \partial S. \tag{16}$$

The boundary condition (14), can be written by means of (11), (4) and (5), and then we have

$$c_2\phi_i(\mathbf{x}) + \int_{\partial S} T_{3j}^S(\mathbf{x},\xi)\phi_j(\xi)dS_\xi = -c(\omega)H_0^{(2)}(\omega r/c^F) - \int_{\partial F} G^F(\mathbf{x},\xi)\Psi(\xi)dS_\xi, \quad \forall \mathbf{x} \in \partial F = \partial S \tag{17}$$

Discretization scheme

In this section, we show the discretization of the Eqs. (15) to (17). Assuming that force densities $\phi(\mathbf{x})$ and $\Psi(\mathbf{x})$ should be constant on each element that forms the surfaces of regions *S* and *F*, respectively, and Gaussian integration (or analytical integration, where the Green's function is singular) is performed, then, Eq. (15) can be written as,

$$\sum_{n=1}^{N} {}_j(\xi_n) g_{3j}^S(\mathbf{x}_l,\xi_n) - \sum_{n=1}^{N}\Psi(\xi_n)\ k = \frac{1}{\rho_F\omega^2}\frac{\partial p^{0^F}(\mathbf{x}_l)}{\partial r}\frac{\partial r}{\partial x_3}, l = 1,N, \tag{18}$$

$$g_{3j}^S(\mathbf{x}_l,\xi_n) = \int_{S_n} G_{3j}^S(\mathbf{x}_l,\xi_n)dS_\xi \tag{19}$$

$$k = c_1\delta_{ij}\delta_{l\,\mathrm{n}} + \int_{S_n}\frac{\partial G^F(\mathbf{x}_l,\xi_n)}{\partial x_3}dS_\xi \tag{20}$$

Eq. (16) leads to:

$$\sum_{n=1}^{N} {}_i(\xi_n) t_{1j}^S(\mathbf{x}_l,\xi_n) = 0, l = 1,N, \tag{21}$$

$$t_{1j}^S(\mathbf{x}_l,\xi_n) = c_2\delta_{ij}\delta_{l\mathrm{n}} + \int_{S_n} T_{1j}^S(\mathbf{x}_l,\xi_n)dS_\xi \tag{22}$$

Eq. (17) can be expressed as:

$$\sum_{n=1}^{N} {}_j(\xi_n) t_{3j}^S(\mathbf{x}_l,\xi_n) + \sum_{n=1}^{N}\Psi(\xi_n) g^F(\mathbf{x}_l,\xi_n) = -c(\omega)H_o^{(2)}(\omega r/c^F), l = 1,N, \tag{23}$$

$$g^F(\mathbf{x}_l,\xi_n) = \int_{S_n} G^F(\mathbf{x}_l,\xi_n)dS_\xi \tag{24}$$

Eqs. (18), (21) and (23) form a system of integral equations that has to be solved and, therefore, force densities $\phi(\mathbf{x})$ and $\Psi(\mathbf{x})$ can be found. Once the force densities have been obtained, the whole displacement and pressure fields in the fluid can be found by means of Eqs. (8) and (9). For the solid, the entire traction and displacement fields can be obtained by means of Eqs. (10) and (11).

Brief description of the formulation by means of the discrete wave number

The discrete wavenumber method is one of the techniques to simulate earthquake ground motions. The seismic wave radiated from a source is expressed as a wavenumber integration (Bouchon and Aki, 1977). The main idea of the method is to represent a source as a superposition of homogenous plane waves propagating in discrete angles. As long as the medium has no inelastic damping, the denominator of the integrand becomes zero for a particular wavenumber and, consequently, the numerical integration becomes impossible. To solve this problem, a method to incorporate a complex frequency was proposed as early as the proposal of the discrete wavenumber method itself (Bouchon and Aki, 1977).

The incident pulse in the fluid, as shown in Fig. 1a (inset), can be given as:

$$p^{0^F}(\mathbf{x}) = C(\omega)H_0^{(2)}(\omega r/c^F) = \frac{C(\omega)}{\pi}\int_{-\infty}^{\infty}\frac{e^{-ikx_1 - i\eta|x_3|}}{\eta}dk \approx \frac{C(\omega)}{\pi}\sum_{n=-N}^{N}\frac{e^{-ik_n x_1 - i\eta_n|x_3|}}{\eta_n}\ k \tag{25}$$

where,

k=the wavenumber, $\eta = \sqrt{\frac{\omega^2}{c^{F^2}} - k^2}$ with $\mathrm{Im}\,\eta < 0$. If we express k in discrete values then we have $k_n = n\ \ k$ and $\eta_n = \sqrt{\frac{\omega^2}{c^{F^2}} - k_n^2}$ with $\mathrm{Im}\,\eta_n < 0$.

If we assume that the whole pressure field in the fluid is represented as the sum of free field and diffracted one, then, it can be expressed, respectively, by:

$$p^F(\mathbf{x}) = p^{0^F}(\mathbf{x}) + p^{d^F}(\mathbf{x})$$
$$= p^{0^F}(\mathbf{x}) + \sum_{n=-N}^{N} A_n e^{-ik_n x_1 + i\eta_n (x_3 - a)} \tag{26}$$

and

$$u_3^F(\mathbf{x}) = \frac{1}{\rho\omega^2}\frac{\partial p^F(\mathbf{x})}{\partial x_3}$$
$$= \frac{1}{\rho\omega^2}\left\{\sum_{n=-N}^{N} \frac{-i\ sig(x_3)}{\pi} e^{-ik_n x_1 - i\eta_n |x_3|}\Delta k \right.$$
$$\left. + \sum_{n=-N}^{N} iA_n \eta_n e^{-ik_n x_1 + i\eta_n |x_3 - a|}\Delta k \right\}. \tag{27}$$

For the solid, we assume that potential of displacement has the form $\phi = \sum B_n e^{-ik_n x_1} e^{-i\gamma_n (x_3 - a)}$ and $\psi = \sum C_n e^{-ik_n x_1} e^{-i\upsilon_n (x_3 - a)}$, $\gamma_n = \sqrt{\frac{\omega^2}{\alpha^2} - k_n^2}$ with $\mathrm{Im}\,\gamma_n < 0$. α and β are the compressional and shear wave velocities, respectively.

The displacement field for the solid can be expressed as $u = \frac{\partial}{\partial x_1} - \frac{\partial \psi}{\partial x_3}$ and $w = \frac{\partial}{\partial x_3} + \frac{\partial \psi}{\partial x_1}$. The stress field is obtained by the well-known equation:

$$\sigma_{ij}(\mathbf{x}) = \lambda\varepsilon_{kk}\delta_{ij} + 2\mu\varepsilon_{ij} \tag{28}$$

where $\sigma_{ij}(\mathbf{x})$=stress tensor, λ and μ are the Lamé's constants, ε_{ij}=strain tensor and δ_{ij} Kronecker's delta.

The boundary conditions to be applied are represented by Eqs. (12) to (14). Once the boundary conditions have been applied, the unknown coefficients A_n, B_n and C_n are obtained and the whole pressure field in the fluid is finally determined by means of the Eq. (26).

Testing and numerical examples

To test the accuracy of our formulation, we selected several interface cases considering a broad range of properties (soft to hard) of solid materials, characterized by their wave propagation velocities and densities. The material properties that were used in the calculations are shown in Table 1, where six cases are presented.

Table 1. Material properties used as validation and numerical examples.

Model	c_p (m s^{-1})	c_s (m s^{-1})	π (kg m^{-3})
Water-Pitch	2443	1000	1270
Water-Granite	6100	2977	2700
Water-Iron	5837	3247	7874
Water-Limestone	4810	2195	2500
Water-Sandstone	2670	1090	2200
Water-Plaster of Paris	3372	1872	1908
Water, for all models	1501	-	1000

Compressional wave velocity, c_p, shear wave velocity, c_s, and mass density, π, were included in Table 1. These materials were previously considered by Borejko (Borejko, 2006), who developed theoretical and experimental techniques to show the emergence of interface waves in several materials like those from Table 1. His results showed good agreement between theoretical and experimental results.

Figure 1 shows the pressure spectra for the six models analyzed for which the wave propagation velocities and densities are displayed in Table 1. For all cases, the initial pressure (source) was generated at a distance of 0.05 m (see inset in Fig.1a) from the elastic solid boundary. The receiver is placed at a horizontal distance of 1.0 m from the source (as shown in the detail of Fig. 1a). The frequency analysis is done considering a frequency increment of 150 Hz and reaching a maximum of 19200 Hz. The discretized surface is located between x_1=-3.5 m and x_1=3.5 m, within this interval spurious waves inside the zone of interest were eliminated. Moreover, 6 boundary elements per S-wave wavelength were considered.

In this figure, the results obtained by the IBEM (dotted line) and by DWN (continuous line) are displayed. There is an excellent agreement between the two methods for the frequency range studied. It can also be seen that for the models of Water-Pitch and Water-Sandstone, resonant effects are slightly manifested. However, in both cases, from the frequency of 6000 Hz, the curves describe a performance almost identical and become asymptotic. This behavior can be attributed due to the fact that their shear wave velocities are lesser than the compressional wave velocity for the fluid.

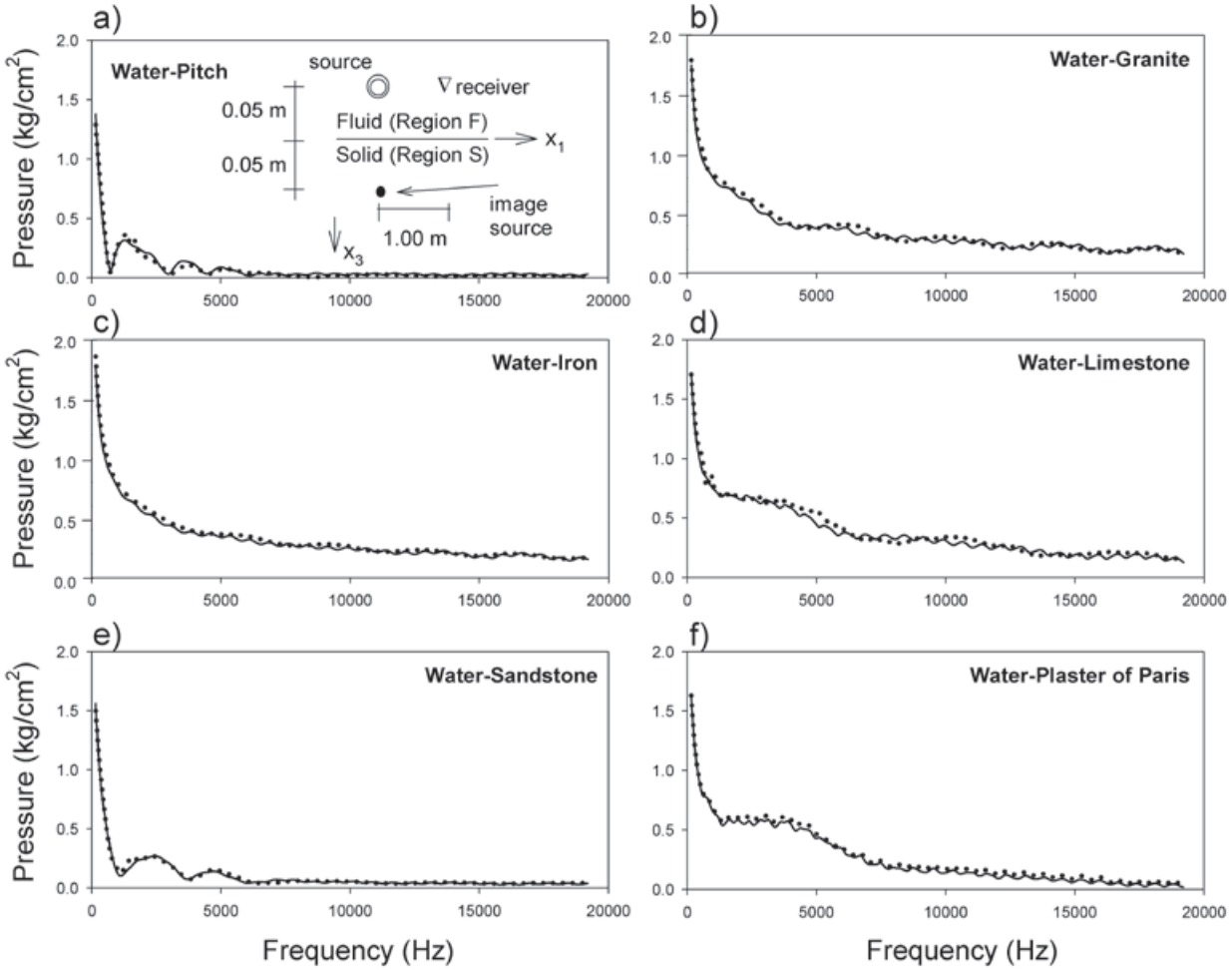

Figure 1. Pressure spectra for six interface materials shown in Table 1. The receiver is located at a=0.05 m and b=1.00 m. Results obtained by IBEM are plotted using dotted lines, while those obtained by means of DWN are drawn with continuous lines.

For all other models (Figures 1b, c, d, f) the spectrum of pressure shows a simple and monotonous behavior, describing oscillations of small-scale in every case. One can notice that for the Figure 1a and e the pressures registered are almost negligible, after 6000 Hz.

Figures 2a and b show the time response for the complete 2D Water-Pitch interface model. For this analysis, a grid of 51 x 51 receivers, spaced using a distance increment of 0.04 m, is used. Column a) shows the results of pressure in the fluid and displacements in the x_1 direction for the solid, while, column b) shows pressures in the fluid and displacements in the x_3 direction for the solid. This phenomenon is shown for three different times.

For the time t=0.000911 s, the initial wave of pressure has hit the solid boundary and a reflected wave in the fluid and diffracted waves in the solid can be seen, generating the emergence of *P* and *S* wave fronts. For the time t=0.001432 s, the above mentioned waves go away from the source while the presence of interface waves is clearly evident to this instant. These are the Scholte's waves and are highlighted using circles in Figures 2a and b. For the time t=0.001953 s, the propagation of interface waves is very visible and shows a delay with respect to the *P* and *S* wave fronts in the solid. Scholte's waves for this case propagates with a velocity of 823.5m s^{-1}.

Figures 2c includes synthetic seismograms of pressures (top figure), x_1 horizontal displacement (middle figure) and x_3 vertical displacement (bottom figure) for seven receivers located near to the interface. The first receiver is located at a horizontal distance of 0.50 m from the source and the others are separated every 0.25 m.

In the seismogram of pressures, the last wave front corresponds to the Scholte's waves, which clearly carry the most of interface energy, as expected. The same effect can be seen in the case of displacement seismograms. It is relevant

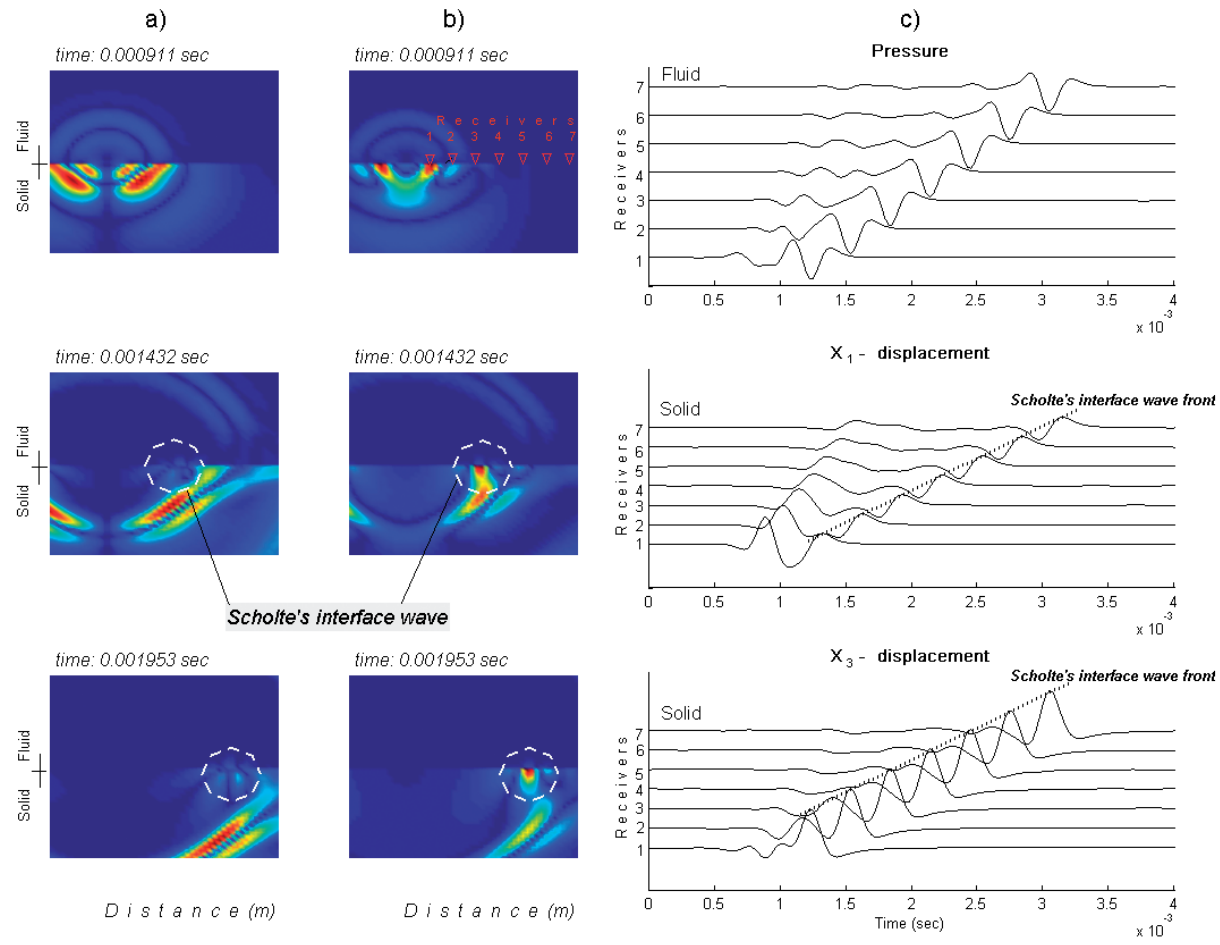

Figure 2. Snapshots by IBEM for the complete 2D Water-Pitch interface model. A grid of 51 x 51 receivers, spaced every 0.04 m, is used. Column a) shows the results of pressures in the fluid and displacements in the x1 direction for the solid, while, column b) shows pressures in the fluid and displacements in the x3 direction for the solid. Column c) displays synthetic seismograms of pressures (top figure) and displacements x1 and x3 directions respectively (middle and bottom figures).

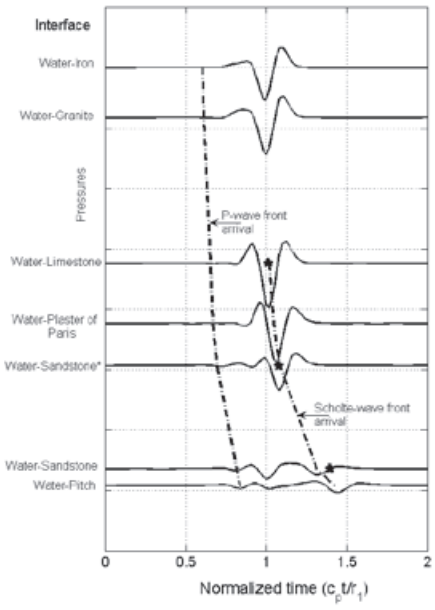

Figure 3. Pressure synthetic seismograms registered by the receiver located as shown in Fig. 1a (inset) for materials detailed in Table 1. Arrival of P and Scholte's wave fronts are also highlighted. Stars indicate arrival times for Scholte's wave fronts obtained by Strick and Ginzbarg, and Strick *et al.* (1956).

to note that for the x_3 direction displacement amplitudes are larger than those for the x_1 direction. This can also be seen in Figures 2a and b (middle and bottom).

Figure 3 displays results in time domain for the materials shown in Table 1. The material tagged with " * " was added for comparison with regard to the results published by Strick and Ginzbarg, and Strick *et al.* (Strick and Ginzbarg, 1956; Strick et al, 1956). The properties for this material (Sandstone* in Fig. 3) are c_p=3740 m s^{-1}, c_s=1645 m s^{-1} and density of 2400 kg m^{-3}. The location of the receiver is illustrated in Figure 1a, for all the cases. Synthetic seismograms in this figure were placed considering the shear wave velocity of each material. The highest speed corresponds to Steel (c_s= 3247 m s^{-1}) and the lowest to Pitch (c_s= 1000 m s^{-1}). The time is normalized with regard to the compressional wave velocity c_p=1501 m s^{-1} (velocity of water) and r_1, which is the distance from the image source and the receiver. In this figure, pressures registered by the receiver (for each material) are plotted.

The pressure waves diffracted by rigid interfaces (as Granite and Steel) show higher values, while, those diffracted by less rigid interfaces, like Sandstone and Pitch, show lower values. Additionally, for these last two cases, the wave fronts tend to be less noticeable. Arrivals of *P* and Scholte's wave fronts are indicated using dashed-dot lines.

For comparative purposes, Scholte's wave front obtained by Strick and Ginzbarg, and Strick *et al.* (1956) is also included. This is represented with stars in the figure, good agreement between the results is observed. It is clear that the Scholte's wave is evident from the Limestone and manifests a significant delay for the Pitch.

Finally, a sinusoidal interface is considered. Figure 4a shows the model used to deal with this geometry. Material properties for this case are: for the elastic medium c_p=3400 ms^{-1}, c_s=1963 ms^{-1} and ρ=2500 ms^{-1}, while for the acoustic one c_p=1500 ms^{-1} and ρ=1020 kgm^{-3}. The source time function is a Ricker wavelet with a dominant frequency of 10 Hz. The source and receiver locations are depicted in Figure 4a. Synthetic seismograms are shown in Figure 4b and c for vertical and horizontal displacements, respectively. Results by IBEM are plotted with a dotted line, while those obtained by means of the Spectral Element Method (SEM, Komatitsch *et al.* 2000), are drawn with a solid line. The agreement between both methods is good. Here, the direct wave is clearly observed since the source point and the receiver are very close to each other. Moreover, multiple reflections are presented because of the interactions between the direct wave and the sinusoidal interface, as expected; this effect is clearly seen in Figure 4b and c. The possibility of modeling arbitrary interface shapes is one of the main advantages of the IBEM. Additionally, another advantage of this method relies on the use of Green´s functions for unbounded space, which have a simple form and can be easily programmed. The use of these functions has provided accurate numerical results.

Conclusions

In this paper we extended the use of the Indirect Boundary Element Method to study the propagation of elastic waves in fluid-solid interfaces. In this numerical technique, based on the Huygens' principle and the Somigliana's representation theorem, the fields of pressures and displacements are expressed in terms of single layer boundary integral equations. Full space Green's functions for tractions and displacements are used, but they are forced to meet the proper boundary conditions that prevail at the fluid-solid interfaces.

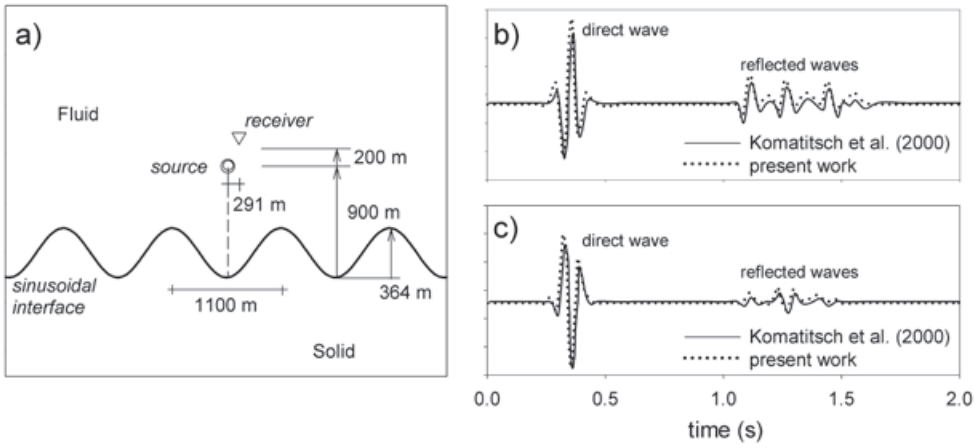

Figure 4. a) Model of a sinusoidal interface. Synthetic seismograms b) vertical displacements; c) horizontal displacements. Results by IBEM are plotted with a dotted line, while those obtained by Komatitsch *et al*. (2000) are drawn with a solid line.

A wide range of solid materials characterized by their wave velocities and densities was analyzed. In every case, the presence and propagation of Scholte's waves is noticed, highlighting the important amount of energy that they carry.

The results obtained from our numerical technique were compared with those obtained by the DWN and SEM. Therefore, we conclude that there is a good agreement between the different approaches studied.

References

António J., Tadeu A., Godinho L., 2005, 2.5D scattering of waves by rigid inclusions buried under a fluid channel via BEM, *European Journal of Mechanics A/Solids* 24, 957–973.

Avila-Carrera R., Rodríguez-Castellanos A., Sánchez-Sesma F.J., Ortiz-Alemán C., 2009, Rayleigh-wave scattering by shallow cracks using the indirect boundary element method. *J. Geophys. Eng.* 6, 221–230.

Biot M.A., 1952, The interaction of Rayleigh and Stoneley waves in the ocean bottom. *Bull. Seism. Soc. Am.* 42, 81-93.

Borejko P., 2006, A new benchmark solution for the problem of water-covered geophysical bottom. International Symposium on Mechanical *Waves in Solids,* Zhejiang University, Hangzhou, China, 15-16 may 2006.

Bouchon M., Aki K., 1977, Discrete wave number representation of seismic source wave fields. *Bull. Seismol. Soc. Am.* 67, 259-277.

Carcione J.M., Helle H.B., 2004, The physics and simulation of wave propagation at the ocean bottom. *Geophysics* 69, 825-839.

Carcione J.M., Helle H.B., Seriani G., Plasencia-Linares M.P., 2005, Simulation of seismograms in a 2-D viscoelastic Earth by pseudospectral methods. *Geofísica Internacional* 44, 123-142.

Eriksson A.S., Bostrom A., Datta S.K., 1995, Ultrasonic wave propagation through a cracked solid. *Wave Motion* 22, 297-310.

Ewing W.M., Jardetzky W.S., Press F., 1957, Elastic waves in layered earth, McGraw-Hill Book Co.

Godinho, L., Tadeu, A., Branco, F., 2001, 3D acoustic scattering from an irregular fluid waveguide via the BEM. Engineering Analysis with Boundary Elements J. 25, 443–453.

Gurevich B., Ciz R., 2006, Shear wave dispersion and attenuation in periodic systems of alternating solid and viscous fluid layers. *International Journal of Solids and Structures* 43, 7673-7683.

Komatitsch D., Barnes C., Tromp J., 2000, Wave propagation near a fluid-solid interface: a spectral-element approach. *Geophysics* 65, 623-631.

Mayes M.J., Nagy P.B., Adler L., Bonner B., Streit R., 1986, Excitation of surface waves of different modes at fluid-porous solid interface. *J. Acoust. Soc. Am.* 79, 249-252.

Meegan G.D., Hamilton M.F., Yu. Il'inskii A., Zabolotskaya E.A., 1999, Nonlinear Stoneley and Scholte waves. *J. Acoust. Soc. Am.* 106, 1712-1723.

Nayfeh A.H., Taylor T.W., Chimenti D.E., 1988, Theoretical wave propagation in multilayered orthotropic media. Applied Mechanics Division), Wave Propagation in Structural Composites 90, 17-27.

Rayleigh J.W.S., 1885, On waves propagated along the plane surface of an elastic solid. Proc. London Math. Soc. 17, 4–11.

Rodríguez-Castellanos A., Ávila-Carrera R., Sánchez-Sesma F.J., 2007, Scattering of Rayleigh-waves by surface-breaking cracks: an integral formulation. *Geofísica Internacional* 46, 241-248.

Rodríguez-Castellanos A., Flores-Mendez E., Sánchez-Sesma F.J., Rodríguez-Sánchez J.E., 2010, Numerical formulation to study fluid-solid interfaces excited by elastic waves. Key Engineering Materials 449, 54-61.

Sánchez-Sesma F.J., Campillo M., 1991, Diffraction of P, SV and Rayleigh waves by topographic features; a boundary integral formulation. *Bull. Seism. Soc. Am.* 81, 1-20.

Scholte J.G., 1942, On the Stoneley wave equation. Proc. K. Ned. Akad. Wet. 45 Pt. 1: 20–25, Pt. 2: 159–164.

Scholte J.G., 1947, The range of existence of Rayleigh and Stoneley waves. *Mon. Not. R. Astron. Soc. Geophys. Suppl.* 5, 120-126.

Stoneley R., 1924, Elastic waves at the surface of separation between two solids. Proc. R. Soc. London, Ser. A 106, 416–428.

Strick E., Ginzbarg A.S., 1956, Stoneley-wave velocities for a fluid-solid interface. 46, 281-292.

Strick E., Roever W.L., Vining T.F., 1956, Theoretical and Experimental Investigation of a Pseudo-Rayleigh Wave. *J. Acoust. Soc. Am.* 28, 794-794.

Thomas C., Igel H., Weber M., Scherbaum F., *Geophys.* 2000, Acoustic simulation of P-wave propagation in a heterogeneous spherical earth: numerical method and application to precursor waves to PKP. J. Int. 141, 6441-6464.

Van Vossen R., Robertsson J.O.A., Chapman C.H., 2002, Finite-difference modeling of wave propagation in a fluid-solid configuration. *Geophysics* 67, 618-624.

Wang J., Zhang C., Jin F., 2004, Analytical solutions for dynamic pressures of coupling fluid-solid-porous medium due to P wave incidence. *Earthquake Engineering and Engineering Vibration* 3, 263-271.

Yoshida M., 1978a, Velocity and response of higher mode Rayleigh waves for the Pacific Ocean. *Bull. Earthq. Res. Inst.* 53, 319-338.

Yoshida M., 1978b, Group velocity distributions of Rayleigh waves and two upper mantle models in the Pacific Ocean. *Bull. Earthq. Res. Inst.* 53, 1135-1150.

Zienkiewicz O.C., Bettess P., Internat. 1978, Fluid-structure dynamic interaction and wave forces, an introduction to numerical treatment. *J. Numer. Meth. Eng.* 13, 1–16.

Geofísica Internacional (2013) 52-1: 31-42

Original paper

UVB solar radiation climatology for Mexico

Mauro Valdés-Barrón*, Juan Carlos Peláez-Chávez, Roberto Bonifaz-Alfonzo, David Riveros-Rosas, Victor Velasco-Herreºra, Hector Estévez-Pérez

Received: January 31, 2012; accepted: September 04, 2012; published on line: December 14, 2012

Resumen

La medición de la radiación solar ultravioleta B de banda (UVB) debe considerarse como una prioridad debido a las implicaciones de este tipo de radiación en la salud pública en todo el país (población nacional total, 108 millones), pero esto no se lleva a cabo en la actualidad en México. Los sensores instalados, que realizan esta tarea en forma cotidiana, cubren solamente el 0.12% del país. Sin embargo, hay métodos alternativos para estimar la radiación UVB para superar la falta de datos de superficie. El más exitoso de estos se basan en la utilización de satélites de monitoreo ambiental. En el presente trabajo, se construyen los mapas UVB en todo el país mediante una sola medición de satélite diaria de UVB al mediodía en tiempo solar verdadero de 1978-2003. Las mediciones obtenidas del satélite fueron comparadas con mediciones a nivel de superficie desde una estación situada en la Ciudad de México con el fin de validar las primeras. El análisis de espectro wavelet es empleado para este fin. Una estrecha correlación se observa entre los dos conjuntos de datos. Además, no existe correspondencia cualitativa entre la distribución espacial de los datos obtenidos por satélite y la topografía de la superficie. La diferencia resultante durante todo el período mencionado es <2% de la media de la energía acumulada promedio anual.

Palabras clave: radiación solar ultravioleta, UVB, índice ultravioleta, IUV, wavelet

Abstract

The measurement of solar B band Ultraviolet radiation (UVB) should be considered a priority in Mexico due to implications on public health throughout the country (total population, 108 million), but this is not carried out at present. Installed sensors cover only 0.12% of the country. However, there are alternative methods for estimating UVB radiation to overcome the lack of surface data. The most successful of these are based on the use of satellites for environmental monitoring. In the present work, UVB maps are constructed for the entire country using a single, daily satellite measurement of UVB at solar noon from 1978–2003. Satellite-derived values are compared with the ground measurements by a surface station located in Mexico City in order to validate the former. Wavelet spectrum analysis is employed to this end. A close correlation is observed between the two sets of data. Moreover, there is qualitative correspondence between the spatial distribution of the satellite-derived data and the surface topography. The difference resulting throughout the period mentioned is <2% of the average annual cumulative energy.

Key words: solar ultraviolet radiation, UVB, ultraviolet index, wavelet.

M. Valdés-Barrón*
R. Bonifaz-Alfonzo
D. Riveros-Rosas
V. Velasco-Herrera
H. Estévez-Pérez
Instituto de Geofísica
Universidad Nacional Autónoma de México
Ciudad Universitaria
Delegación Coyoacán, 04510
México D.F., México
*Corresponding author: mauro@geofisica.unam.mx

J.C. Peláez-Chávez
Servicio Metereológico de Cuba

Introduction

Solar radiation is the main source of energy on our planet. Different spectral ranges of solar radiation are responsible for triggering several physical and biological processes, which are important to the balance of ecosystems that make up the variety of climates and biodiversity. Specifically, the B band of Ultraviolet solar radiation (UVB) is a small window of the electromagnetic spectrum (with wavelengths ranging from 0.280–0.320 microns) whose photons carry sufficient energy to break the molecules of important components of the atmosphere (ozone, carbon dioxide, nitrogen dioxide, hydrogen peroxide, formaldehyde, nitric acid, etc.). Thus, UVB radiation is linked with the majority of the photochemical processes occurring in the Earth's atmosphere.

The decrease of Ozone (O_3) in the stratosphere at medium and high latitudes has been one of the most serious atmospheric pollution problems in recent decades World Meteorological Organization (WMO, 1994) and is closely related with a severe increase in solar Ultraviolet (UV) radiation in all of the spectral bands (A, B, and C). Because of the great extent of damage to the ozone layer, this phenomenon is manifested on the Earth's surface. The O_3 reduction not only affects the atmospheric composition in terms of concentration or the absence of specific compounds or gases, but also it in general has drastic effects on the health of living beings, including humans. In particular, the amount of UVB radiation reaching the Earth's surface is increased with the decrease in the ozone-layer thickness. This parameter plays an important role in life on the Earth's surface; thus, knowing the UVB spatial and temporal distributions may help in setting up public health programs for the prevention of the short-, mid-, and long-term risks of UVB exposure.

Although in several parts of the world UVB measurements are carried out on a routine basis and are reported (hourly) to the general public (Universität Innsbruck, 2008), (University of Southern Queensland, 2008), due importance has not been afforded to this meteorological parameter in Mexico. There are some isolated cases (point measurements) in which UVB is monitored for research purposes as, for instance, the Universidad Nacional Autónoma de México (UNAM) and the Universidad de Colima (UC). Only the Metropolitan area of Mexico City (MAMC) has a network of UVB sensors, that has been established that produces measurements on a continuous basis and whose results are available to the general public (http://www.sma.df.gob.mx/simat/) (RAMA, 2008).

However, this network has a spatial coverage of merely 2,500 km^2, which is approximately 0.12% of the country. The potential beneficiaries of this activity, therefore, amount to only about 20% of the total national population.

Mexico has a very abrupt orography. Therefore, a meteorological station in many cases cannot be considered representative of the minimum area recommended by the World Meteorological Organization (WMO, 1996); considerable variations in elevation occur within very short distances, causing rapid spatial variation of climatic parameters. Therefore, to ensure continuous and effective monitoring, a surface network would certainly require >1,000 stations. The cost of UVB radiation sensors does not allow the possibility of installing such a large network, and it is also necessary to take additional costs into account, such as preventive and corrective maintenance, as well as annual calibration for the sensors.

Fortunately, there are techniques that can aid us in estimating the levels of B band solar UV radiation at ground level. These techniques range from theoretical radiative transfer models (Gutiérrez-Marco *et al*., 2007), (Kudish *et al*., 2011) to models that utilize meteorological satellite data (Peeters *et al*., 2000), (Ciren and Li, 2003), (Espinar *et al*., 2009), (Janjai *et al*., 2010). The latter is a good alternative, because in the majority of cases it allows evaluation of different meteorological parameters with a single satellite, greatly reducing the aforementioned costs. Moreover, this satellite information is available on the Internet.

In the present work, the results of an assessment of UVB radiation for Mexico are reported. UVB radiation at ground level is evaluated at solar noon. The data used for the evaluation were measured by sensors called Total Ozone Mapping Spectrometers (TOMS), which operated in three different satellites of the National Aeronautics and Space Administration (NASA) from 11/1/1978 to 12/31/2005. These sensors performed nearly constant monitoring of the ozone layer and UVB radiation (Figure 1), generating a highly reliable database for understanding the climatology of the UVB [TOMS, 2011].

Methodology

TOMS are spectrometers that can measure the total amount of ozone in the atmospheric column (from ground level to the top of the atmosphere) under any geographical and atmospheric conditions. Measurements are made in the UV region,

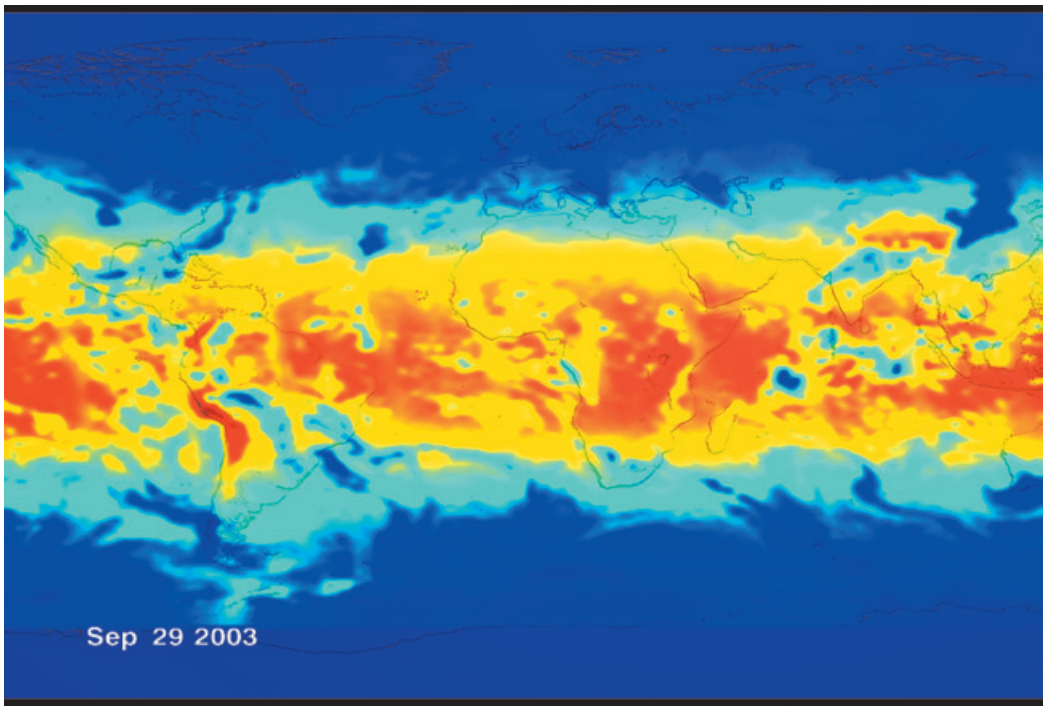

Figure 1. Example of Ultraviolet (UV) image based on data from Total Ozone Mapping Spectrometers (TOMS) during September 29, 2003. The image provides us with a global perspective on the distribution of UV irradiance on the Earth's surface. (Image from Earth Observatory, National Aeronautical and Space Administration, NASA).

where solar radiation is partially absorbed by ozone. They are performed for both incoming and reflected solar radiation. The latter is composed of a part that actually reaches the Earth's surface and is reflected, and of a part that is backscattered into space by the air molecules and clouds. From the measurement of this reflected radiation, UVB at ground level and the thickness of the ozone layer are estimated by means of approximate models (McPeters, 1996).

The instrument has a single, fixed monochromator with exit slits at six near-UV wavelengths (between 308 and 380 nm) and a scanning mirror for sampling backscattered radiation. The accuracy of TOMS was estimated at ±5%, with a spatial resolution of 1° latitude × 1° longitude. These carried out 35 measurements every 8 sec and ground coverage is 50–200 km wide on Earth, depending on the latitude for each meridian. Nearly 200,000 daily measurements cover the surface of the Earth, except for areas near the poles during seasons when the sun remains below the horizon. In practical terms, this technology allows having, in the case of UVB, a single, daily data point for 12:00 hrs TST (True Solar Time) (McPeters, 1996), (Herman, 1996), (McPeters, 1998).

Data Source

The information can be obtained in the NASA web server for TOMS (http://toms.gsfc.nasa.gov/ery_uv/euv_v8.html). It corresponds to global coverage on daily arrays that are ordered in latitudinal groups that range from 89.5° South to 89.5° North. Longitude is covered from 179.5° West to 179.5° East. The readings are expressed in milliWatts per square meter (mW/m²), and as mentioned previously, each value corresponds to a single data point at noon TST. Each reading is expressed with a group of three digits, for example, 245. The first corresponds to the exponent for each datum in scientific notation, and the last two digits comprise the reading divided by 10. For example, 245 correspond to the 4.5 × 10² mW/m² reading.

From the overall global matrix, we selected the data bound between 84° and 120° West, and 10° and 36º North, which by far contains the entire territory of Mexico. These limits are sufficiently far from the true geographical extension of the country for the interpolation of climatological values to be free of edge effects; i.e., there is no need to be concerned with distortions caused near the points on the edges

of the array. Thus, after using the data to obtain the desired contours, the area-of-interest is cut by about 3° of latitude and 3° of longitude on each end.

First, the TOMS files were transferred from the data server, one file for each day since 1978 and up to 2003. From this information, daily files for the selected coordinates were obtained. The selected data were employed to generate matrices of monthly and annual averages, and also seasonal matrices.

Using a Geographic Information System (GIS), matrices with the average monthly points were incorporated and interpolated with the Kriging's method to obtain an array, with the interpolated values in color gradation, in order to differentiate intensities and the contours for each month. Furthermore, a digital elevation model was included and the state boundaries in a Lambert Conical Conformal projection.

After obtaining the maps, measurements reported by surface stations were used to validate the information obtained by this procedure. The available surface stations comprise the Solar Radiation Observatory (ORS) of the Instituto de Geofísica (IGeof) of the Universidad Nacional Autónoma de México (UNAM) and the stations in the Red Automática de Monitoreo Atmosférico (RAMA) of the Mexico City Government. Both systems generate highly reliable information because each station meets WMO requirements. However, we decided to use the data from ORS (19º 20' 01'' ‹North Latitude, 99º 10' 54'' West Longitude at 2,268 m above sea level) because this is considered by WMO as a Regional Centre for Solar Radiation in the IV Region (AR-IV).

To make this comparison, we used a Solar Light sensor, model 501a, serial number 2010. This sensor works in a spectral window from 0.280–0.320 μm (Solar Light, 1991).

As discussed previously, information from the satellite observations is registered once a day, at true solar noon, while the surface data are measured every minute. Therefore, the surface measurements used for comparison correspond to those at 11:59, 12:00, and 12:01 TST, which were averaged in order to compensate for possible delays or advances of a few seconds with respect to the satellite observation.

Wavelet analysis

To analyze local variations of power spectrum within a single non-stationary time series at multiple periodicities, such as UVB surface data and satellite data, the Morlet Wavelet is applied here because it provides higher resolution in the periodicity and because being a complex function allows us to analyze the evolution of periodicities in the time-space and to calculate the phase between two time series (Soon *et al.* 2011).

The Morlet wavelet consists of a complex exponential function modulated by a Gaussian wavelet and is defined as:

$$e^{i\omega_o t/s} e^{-t^2/(2s^2)}, \qquad (1)$$

where t is the time with s = *period* as the wavelet scale and ω_0 is a non-dimensional frequency. Here, $\omega_0 = 6$ to satisfy the admissibility condition (Farge, 1992).

The cone of influence (COI) is the region of the wavelet spectrum outside which the edge effects become important (Torrence and Compo, 1998).

Wavelet Power Spectral Density (WPSD) is calculated for each parameter; the black thin lines in Figures 2, 3 and 4 marks the 95% confidence interval or boundaries of COI.

We use the inverse wavelet transform to obtain the decomposition of a signal and can be obtained from a time-scale filter (Mendoza and Velasco, 2011). Inverse wavelet transform is defined (Torrence and Compo, 1998) as:

$$X_n = \frac{\delta_j \delta_t^{1/2}}{C_\delta \psi_o(0)} \sum_{j=0}^{J} \frac{\mathrm{Re}\left\{W_n\left(s_j\right)\right\}}{s_j^{1/2}}, \qquad (2)$$

where δ_j is the factor for scale averaging, C_δ is a constant (δ_j = 0.6 and C_δ = 0.776, for Morlet wavelet), and ψ_0 removes the energy scaling.

The cross wavelet $W_k^{X_1X_2}(\psi)$ (XWT) was used which measures the common power spectrum between the input (X_1) and output (X_2) in physics system and is defined as (Torrence and Compo, 1998):

$$W_n^{X_1,X_2} = W_n^{X_1} W_n^{X_2}, \qquad (3)$$

where (*) denotes complex conjugation, ($W_n^{X_1}$) and ($W_n^{X_2}$) is the wavelet transforms (WT) of the time series X_1 and X_2

The arrows in the cross-wavelet spectra show the mean relative phase between the X_1 (input) and X_2 (output) series in time-frequency space: arrows at 0° (pointing to the right) indicate that both time series are perfectly positively correlated (in phase) and arrows at 180° (pointing to the left) indicate that they

are perfectly negatively correlated (180° anti-phase). It is important to point out that these two cases imply a linear relationship between the considered phenomena. Non-horizontal arrows indicate an out of phase situation, meaning that the two studied phenomena have a more complex non-linear relationship.

On the left panels of Figures 2, 3, and 4, the wavelet *global spectra* are shown, which is an average power of each periodicity in both the wavelet and the cross spectra.

The significance level of the global wavelet spectra is indicated by the dashed curves; they refer to the power of the red noise level at the 95% confidence level that increases with decreasing frequency (Grinsted *et al.* 2004).

Results and Discussion

The results of the previously described procedure are presented in Figures 2–4, in which the global wavelet spectrum is shown as a function of time.

In Figure 2, it can be observed that the global wavelet spectrum (panel C) of the surface data shows a prominent annual periodicity, with a 95% confidence interval (95% CI) defined by the red noise (red dotted line). As we can also observe (panel B), the Morlet wavelet is present throughout all time intervals (framed by a black line). In addition to the 1-year period, half-year periodicity is also present in the overall wavelet spectrum throughout the time interval (1997–2003). Additionally, there are periodicities on the order of a few days that can be observed, especially around the maxima of the time series of surface data shown in panel (A).

It should be noted that these periodicities of a few days (66, 35, 20, 9, 4 and 2) are located around the descending part of the annual maximum. The chart also provides information on the behavior of UVB intensity at the surface. As can be observed, the years 1998 and 2001 were the most intense over the period of study.

Similarly to the surface data, the global wavelet spectrum (panel C) of the satellite data (Figure 3) shows a prominent annual periodicity, with 95% reliability; as one may observe, the Morlet wavelet (panel B) is present throughout the time interval (1997–2003). There is also a half-year periodicity that is present throughout the time series, but with less intensity than in the surface data. In addition, there are periodicities of 2, 10, 15, 33, and 74 days around the maximum of the time series of surface data. However, in the satellite data, these periodicities are more spread out over the maximum.

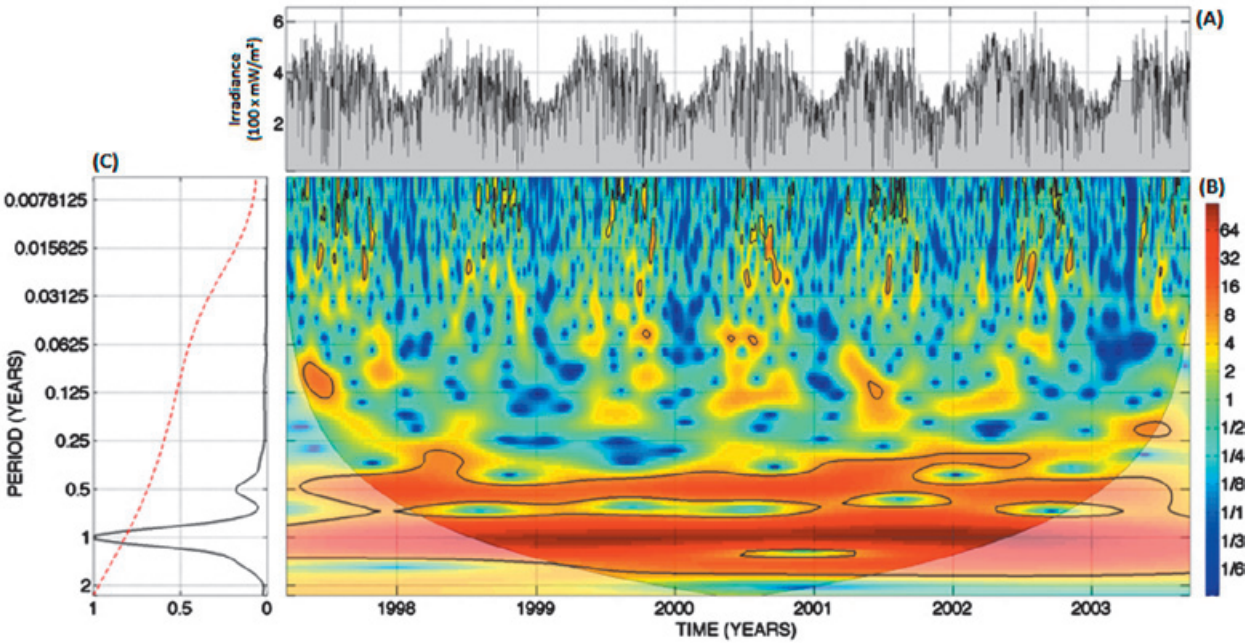

Figure 2. Wavelet spectrum for surface data. Upper graph (panel A), time series; lower right (panel B), wavelet power spectra; lower left (panel C), global wavelet spectrum.

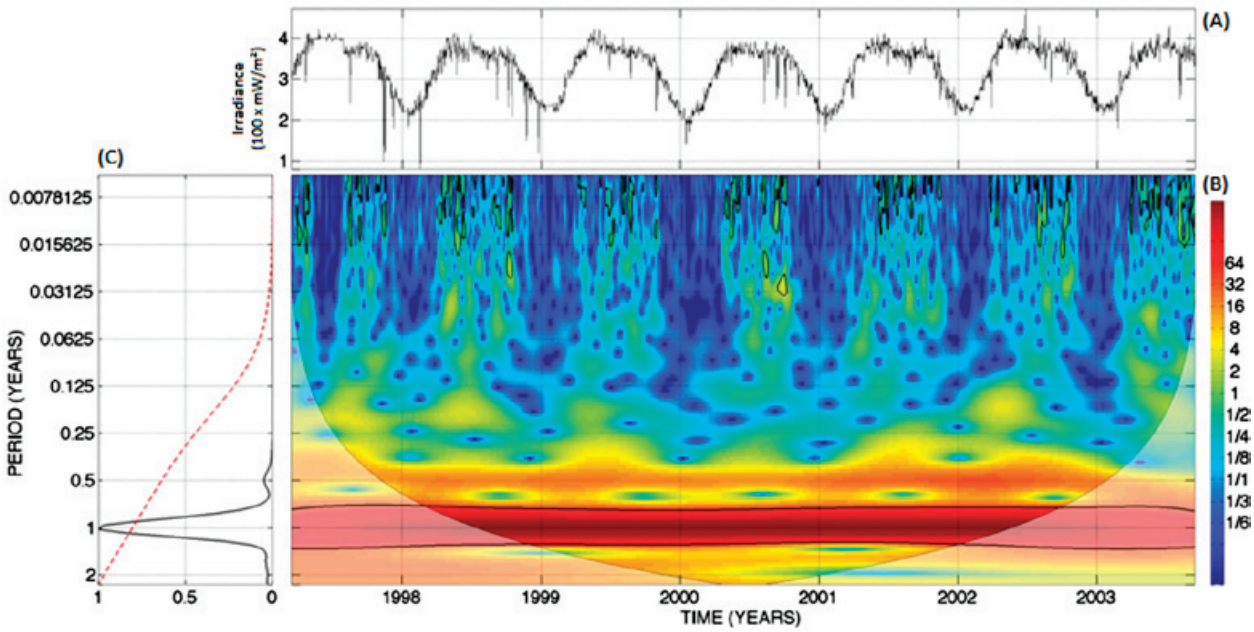

Figure 3. Wavelet spectrum for satellite data: (panel A), time series; lower right (panel B), wavelet power spectra; lower left (panel C), wavelet global spectrum.

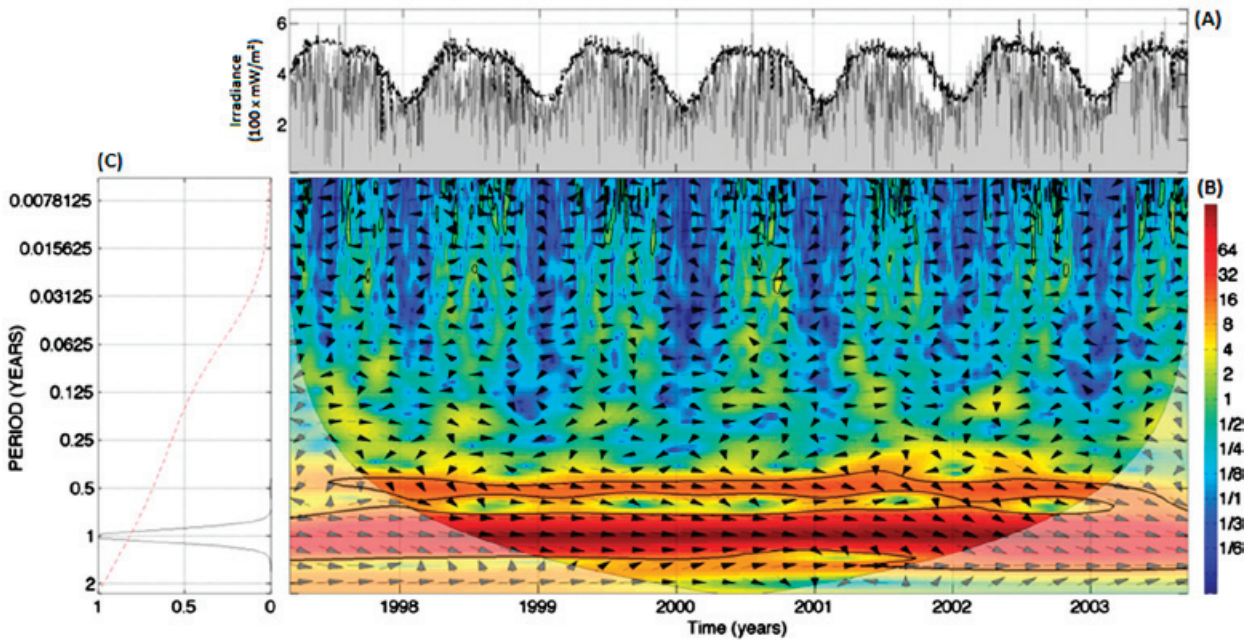

Figure 4. Cross-wavelet spectrum of surface data with satellite data. Upper graph (panel A), time series; lower right (panel B), wavelet power spectra, shown in color and a relative phase difference is indicated by the arrows.; lower left (panel C), wavelet global spectrum.

The wavelet global spectrum (panel C) from surface data and satellite data (Figure 4) shows that the common periodicity, both in phase and maximum value, is annual, with 95% reliability, with the cross-wavelet (panel B) present throughout the time interval (1997–2003). There are also other periodicities in common with <95% reliability that have a frequency of about one half year and that are also present throughout the whole period. The periodicities of 2, 9, 20, 35, and

66 days are present mainly around the maximum of the time series of surface and satellite data. The arrows show a phase lag between surface and satellite data because the former are local and point measurements, while the latter are global volumetric; while the surface data are measured at a given point on the surface of the Earth, the satellite data represents an average of the processes of extinction of UVB radiation throughout the atmosphere within an area of about 1° latitude × 1° longitude and where weather conditions can change locally. Thus, periodicities on the order of a few days are not synchronized between the two series. We can observe that for half-year periodicities under the relationship is nonlinear and complex, because the arrows indicating the phase in the two time series, shows random orientation, while for periodicities greater than half-year, the arrows are oriented from left to right indicating a linear behavior.

In panel C, values of the "classical" correlation coefficient of the information derived from surface and satellite measurements are presented. This coefficient has low values, indicating that there is a non-linear relationship between the two. This makes the advantage of the cross-wavelet (Figure 4) evident: it does not matter whether the two data sets are linearly dependent or not because the local correlation coefficient is computed independently for each of the periodicities involved; therefore, we have a high coefficient in the periodicities (few days, 6 months, and annual).

The results of wavelet analysis, is used to filter the data (for a comparison) and improve the correlation between surface data and satellite measurements. Figure 5(a) shows the comparison between these data and Figure 5(b) shows a remarkable improvement of the correlation coefficient.

We use the inverse wavelet transform (eq. 2) to obtain the time series > 1 years. Were filtered data that correspond to periodicities less than 1 year and they were identified through wavelet analysis. The correlation coefficient is significantly better after filtering the data. Before filtering the correlation coefficient was 0.3758, after filtering the correlation coefficient was 0.7462.

As an example of the results, we present the average monthly maps of one month of the winter season (Figure 6) and one month of the summer season (1978-2003) (Figure 7), where it can be seen the spatial distribution of UVB throughout the country (January and August). The green point on figures indicates the position of surface sensor in Mexico City.

During the winter, when the Sun declination reaches its maximum negative value, the solar radiation reaches the surface of the Earth with greater inclination significantly reducing the energy per unit area, so that the distribution in surface UVB predominantly responds to latitudinal pattern throughout the country, which is only modified by major topographic features (Volcanic Belt, Sierra Madre Occidental, Sierra Madre Oriental and Sierra Madre del Sur).

For the summer months the shape of the isolines is completely different, as a predominantly latitudinal distribution, going to concentrate the maximum values in the upper parts of the main topographical features (Volcanic Belt, Sierra Madre Occidental, Sierra Madre del Sur and Sierra de Baja California) with a gradient which tends to decrease to the sea level. This is because during the months around the summer solstice, the sun declination angle is positive and the sun's path at noon is near to the zenith. For this reason the sun's irradiation is greater, the solar radiation interacts less with the Earth's atmosphere, so the processes of extinction of solar radiation are reduced.

Finally, in Figure 8, we can see the different values of monthly average UVB for three sites located at similar latitude: Manzanillo City, Colima. (19° 03' N, 104° 18'W, 5 m AMSL), Tlamacas Station on the northern flank of the volcano Popocatépetl (19° 03' N, 98° 37' W, 3867 m AMSL) and Boca del Río, Veracruz (19° 03' N, 95° 59' W, 14 m AMSL) but at different altitudes (Figure 9).

Values corresponding to the station Tlamacas, always remains above the other two sites, due basically to the altitude. While less atmosphere through solar radiation, fewer extinguishing processes act on it and the amount of energy per unit area will be greater. For the other two sites (Manzanillo, Col. and Boca del Río, Veracruz), the radiation must cross more atmosphere and the extinction processes will be grater. The difference between the last two curves, is primarily due to climatic factors, among which, topography, (Boca del Río is located on a very wide coastal plain, while in Manzanillo, coastal plain barely exists); Boca del Río is much more exposed to the phenomena of "North" in winter. In summer the effects of tropical storms and tropical cyclones are more frequently in Boca del Rio in the Gulf of Mexico than in Manzanillo in the Pacific area.

An important point to note is that apparently there are only three periods in the behavior of the UVB at the surface, the first of January to March where the radiation simply increases to

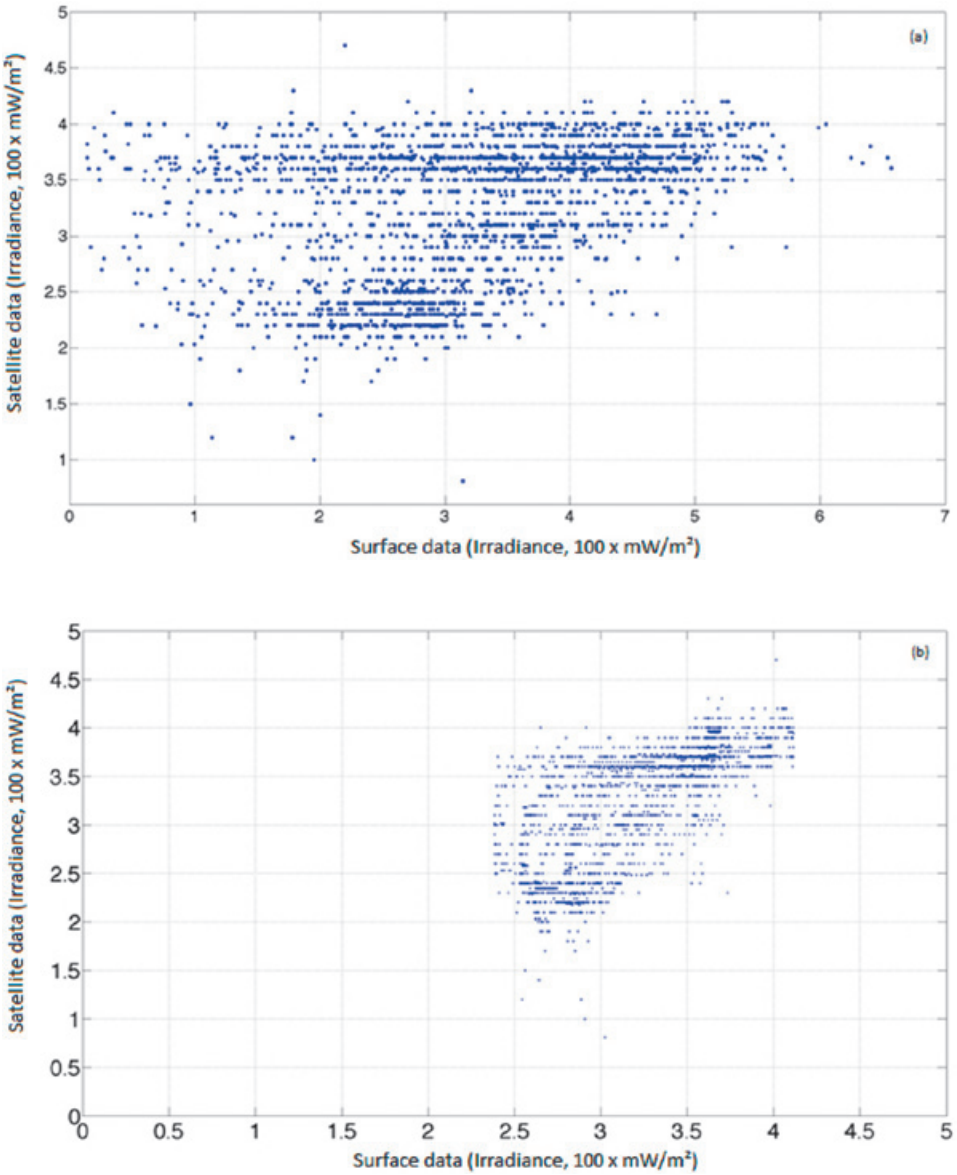

Figure 5. Comparison between surface and satellite data, upper graph (a) before filtering data, lower graph (b) after filtering data.

reach its peak in the month of March. After a period of semi-stability which runs from April to August or September where, although it has a tendency decrease, at the end of this period is stabilized. And the third and final stage, which is a clear decrease in solar irradiance during the months of October to December where in the last month has again reached its minimum values.

Finally it is important to mention that the main factors that determine the spatiotemporal distribution of solar radiation on the surface, are cloudiness and topography, and the results presented here, are influenced by these two factors, the relative distribution of UVB on the surface to the whole country can be considered highly reliable. But we must not forget one important limitation of this work, there was only a single reference point (Mexico City) to validate the UVB satellite measurements, so we cannot generalize concerning the validity of measurements on each point for the entire country, because it does not have sufficient reference points on this surface.

During the majority of autumn and winter months (January, February, March, November, and December), when solar declination is negative and the Sun's rays reach the surface in more inclined fashion, the distribution of UVB is nearly latitudinal. There are also two transition months (April and October) between this "winter" behavior and what might be called "summer", where the latitudinal distribution

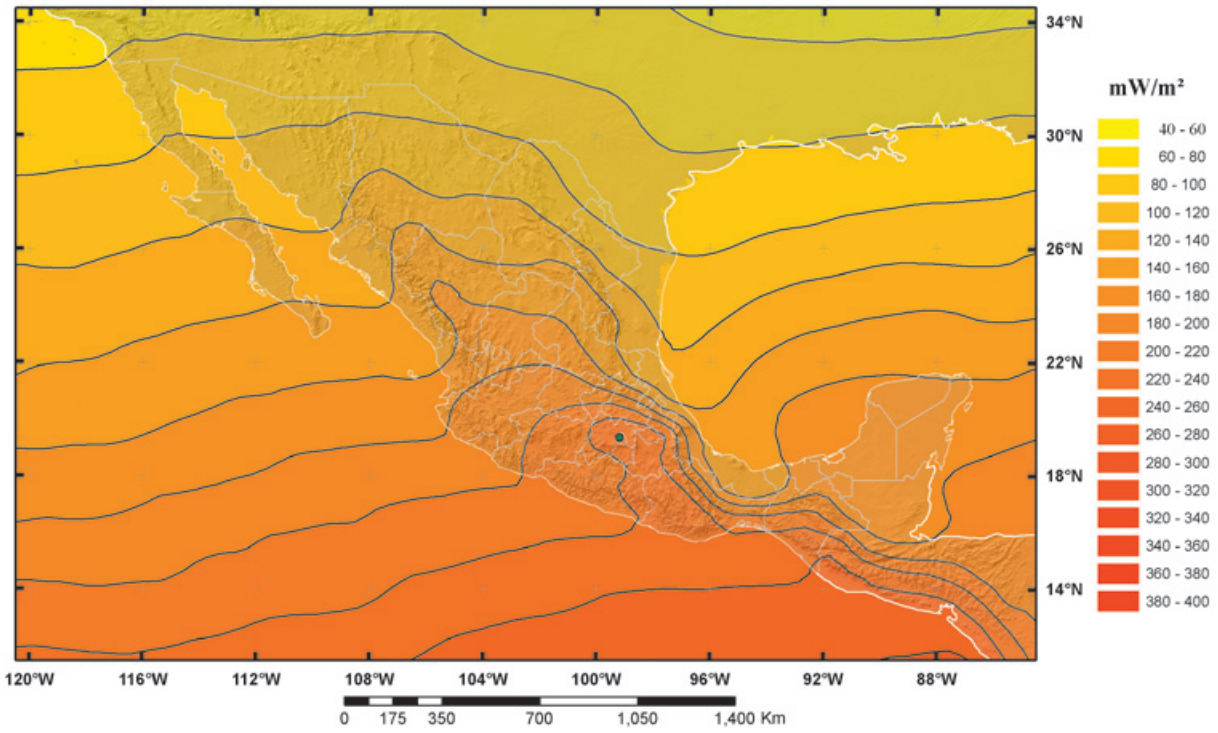

Figure 6. UVB solar Radiation. January monthly mean average (1978–2003).

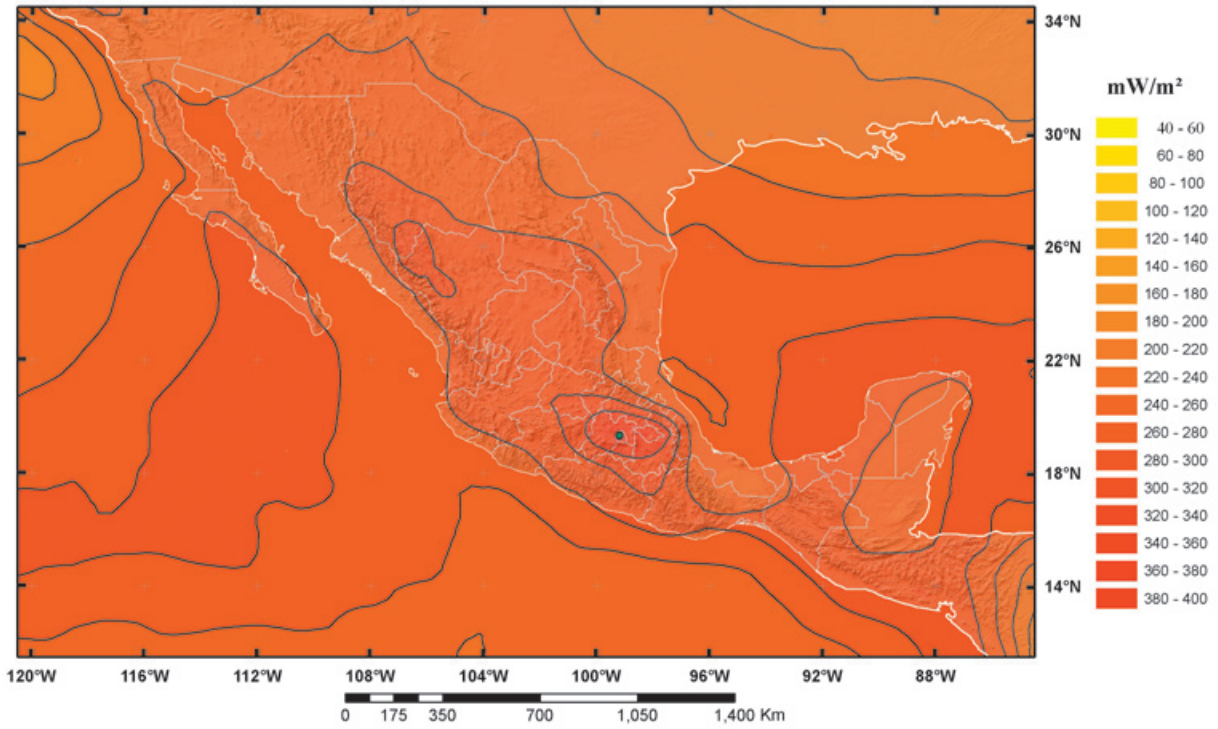

Figure 7. UVB solar Radiation. August monthly mean average (1978–2003).

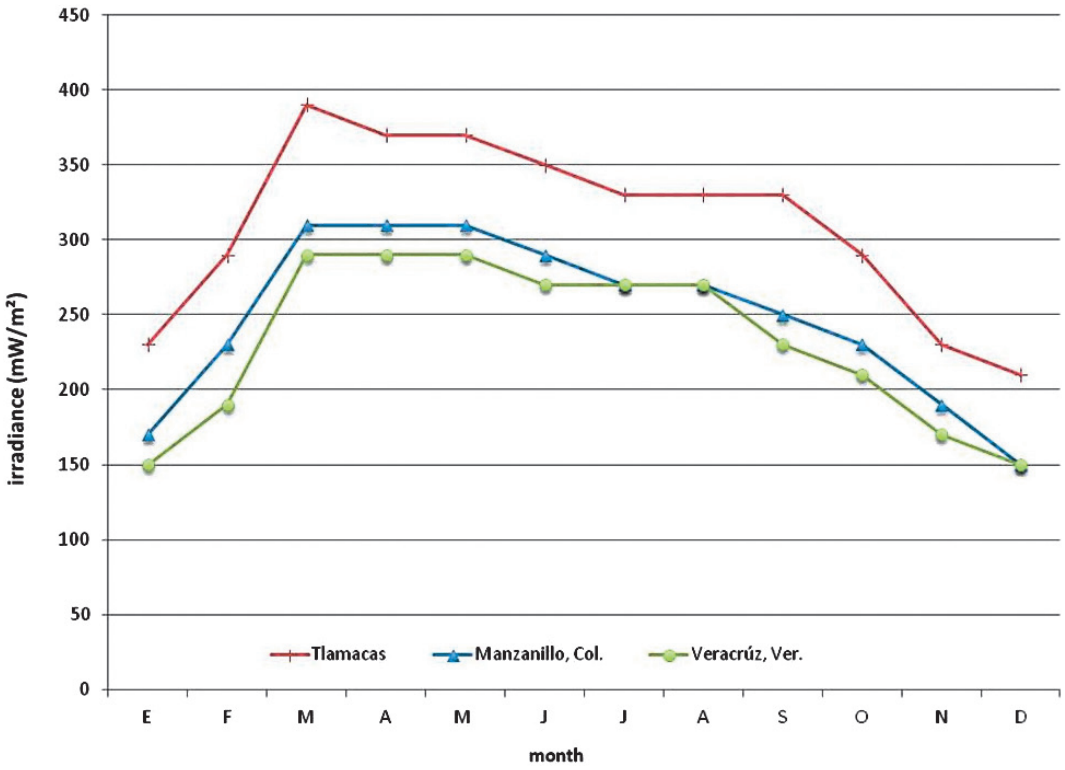

Figure 8. Monthly average UVB for three sites located at similar latitude and different altitude.

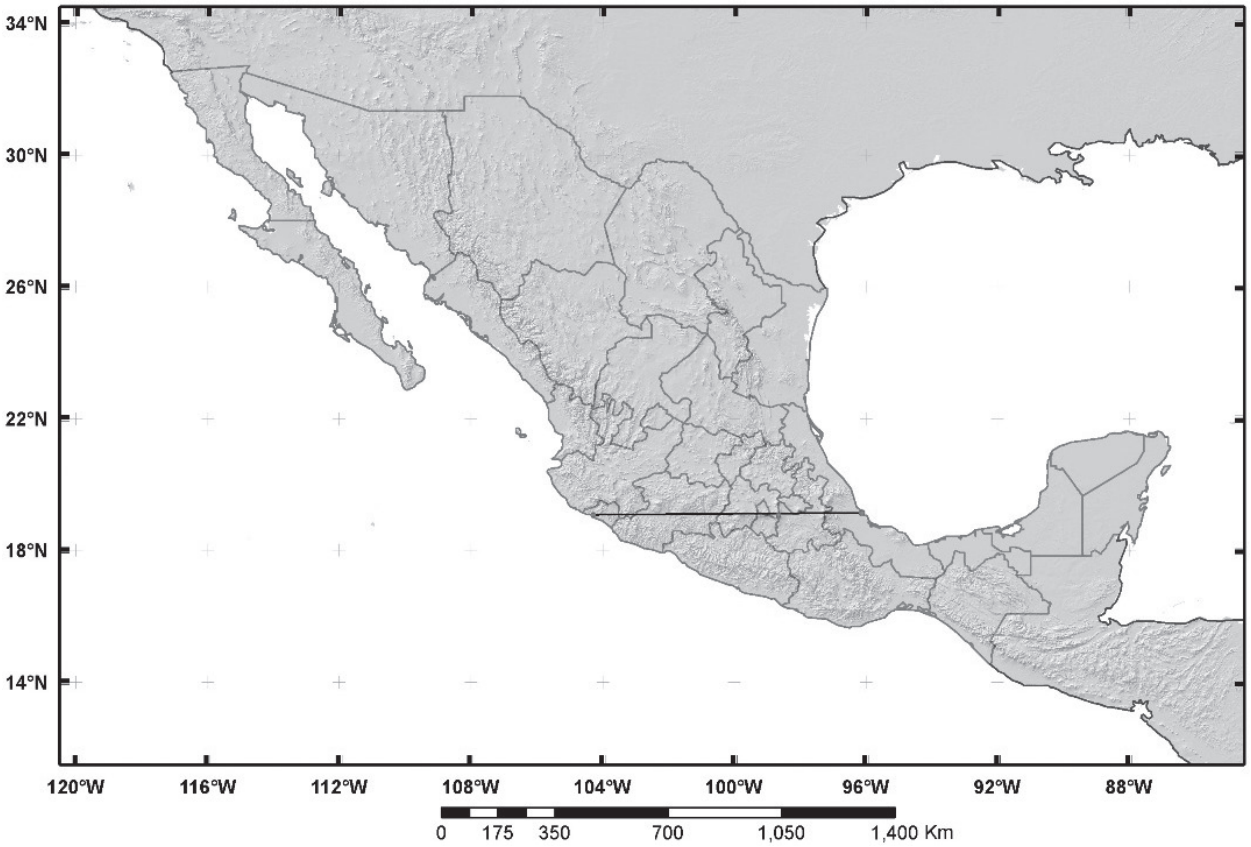

Figure 9. Transect for three sites at similar latitude (red dots). Manzanillo (left), Tlamacas (middle), Veracruz (right).

of UVB seems to disappear. The latter occurs because solar declination is positive and the rays reach the surface in a nearly vertical direction at this time of the year, reducing the optical mass of atmosphere crossed by radiation. The highest values for UVB radiation are found in the highest parts of the major topographical features of the country (*Cinturón Volcánico Transversal, Sierra Madre Occidental, Sierra Madre del Sur,* and even in the *Sierra de Baja California*).

The previously mentioned behavior may be considered as "expected", due primarily to that during the winter months, the Sun's rays reach the surface with such an inclination that higher values were close to Ecuador and smaller values are oriented toward the North Pole. There is also a small deformity in latitudinal distribution due to the *Cinturón Volcánico Transversal* and the *Sierra Madre Occidental*, major topographic features of the country, and this deformity responds to the presence of higher values than those found for the remainder of the national territory. It is necessary to recall that solar radiation undergoes extinction processes such as absorption, reflection, and scattering, and extinction grows while the optical path increases; thus, higher values are always found at higher altitudes.

This extinction process can be identified in the "summer" months, when the angle of incidence for solar radiation is close to the vertical direction over the surface of Mexico. Therefore, distribution of UVB values has greater intensity in the higher parts of Mexico, while the latitudinal distribution that characterizes the winter months is completely lost.

It is noteworthy that these maps were obtained with observations at 12:00 hrs TST, which means that they were carried out when the sun is at its highest position. In other words, the data correspond to the maximum intensity of radiation that can reach the surface on a given day; therefore, the expected maximum radiation is depicted in the maps.

Conclusions

The use of satellites for the evaluation of natural resources or environmental monitoring, specifically in the case of UVB, are of vital importance as they provide an affordable option as opposed to a network of sensors that are sufficiently dense to carry out monitoring on this scale.

While the behavior of UVB radiation can be known through models that describe radiation transfer through the atmosphere, it had never been possible to carry out such a description for the whole country, due in part to the lack of detailed information on the local composition of the atmosphere. This work represents, to our knowledge, the first assessment of the spatial and temporal distribution of solar UVB radiation for Mexico.

Satellite measurements of UVB obtained at the reference point at the ORS in Mexico City showed good correlation with surface measurements, which ensures the reliability of the satellite data at that point. Moreover, spatial and temporal distribution throughout the year is consistent with the behavior that one might expect from the geographical variation of altitude and latitude of the studied area. Therefore, the use of satellite sensors appears to be suitable for the country. This may help to identify areas with the highest values of UVB radiation, either for application in health policy and prevention of UVB overexposure, or for applications in renewable energy using this type of radiation. It would be desirable to have more ground stations for comparison for more rigorous assessment of the validity of the method.

Acknowledgments

The authors thank Mr. Ismael Velázquez-Orozco for his support in the management of computer equipment, Mr. Ernesto Jiménez de la Cuesta for his support for data processing of UVB radiation, and Dr. Camilo Arancibia-Bulnes for his comments on the manuscript.

Bibliography

Ciren P., Li Z., 2003, Long-term global Earth surface ultraviolet radiation exposure derived from ISCCP and TOMS satellite measurements, *Agricultural and Forest Meteorology*, 1-4, 120, 51-68 p., ISSN 0168-1923.

Espinar B., Ramírez L., Drews A., Georg Beyer V., Zarzalejo L.F., Polo J., Martín L., 2009, Analysis of different comparison parameters applied to solar radiation data from satellite and German radiometric stations, *Solar Energy*, 1, 83, 118-125 pp.

Farge M., Goirand E., Meyer Y., Pascal F., Wickerhauser M.V., 1992, Improved predictability of two-dimensional turbulent flows using wavelet packet compression, Fluid Dynamics Research, 10, 4-6, 229-250.

Grinsted A., Moore J.C., Jevrejeva S., 2004, Application of the cross wavelet transform and wavelet coherence to geophysical time series, Nonlinear Processes Geophys., 11, 5-6, pp 561–566.

Gutiérrez-Marco E., Hernández E., Camacho J.L., Labajo A., 2007, Analysis of UVB values in the centre of the Iberian Peninsula, Atmospheric Research, 84, 4, pp 345-352.

Herman J.R., Bhartia P.K., Krueger A.J., McPeters R.D., Wellemeyer C.G., Seftor C.J., Jaross G., Torres O., Labow G., Byerly W., Taylor S.L., Swissler T., Cebula R.P., Gu X.Y., 1996, Meteor–3 Total Ozone Mapping Spectrometer (TOMS) Data Products User's Guide, NASA Reference Publication 1393. National Aeronautics and Space Administration, Washington, DC.

Hernández Ordóñez A.E., 2000, Climatología de la Radiación Solar Ultravioleta Banda "B" en la ZMCM, Tesis de Licenciatura, Facultad de Filosofía y Letras, Universidad Nacional Autónoma de México.

Janjai S., Buntung S., Wattan R., Masiri I., 2010, Mapping solar ultraviolet radiation from satellite data in a tropical environment, Remote Sensing of Environment, 114, 3, pp 682-691.

Kudish A.I., Evseev E.G., 2011, The analysis of solar UVB radiation as a function of solar global radiation, ozone layer thickness and aerosol optical density, Renewable Energy, 36, 6, pp 1854-1860.

McPeters, R.D., Bhartia P.K., Krueger A.J., Herman J.R., Schlesinger B.M., Wellemeyer C.G., Seftor C.J. , Jaross G., Taylor S.L., Swissler T., Torres O., Labow G., Byerly W., Cebula R.P., 1996, Nimbus-7 Total Ozone Mapping Spectrometer (TOMS) Data Products User's Guide. NASA Reference Publication 1384. National Aeronautics and Space Administration, Washington, DC.

McPeters, R D., Bhartia P K., Krueger A.J., Herman J.R., Wellemeyer C.G., Seftor C.J., Jaross G., Torres O., Moy L., Labow G., Byerly W., Taylor S.L., Swissler T. and Cebula R.P., 1998, Earth Probe Total Ozone Mapping Spectrometer (TOMS) Data Products User's Guide. NASA Reference Publication 206895, National Aeronautics and Space Administration, Washington, DC.

Medizinische Universität Innsbruck, Sektion für Biomedizinische Physik, 2008, http://www.uv-index.at/.

Mendoza B., Velasco Herrera V.M., 2011, *Solar Physics*, 271, 169-182 p.

Observatorio de Radiación Solar, 2008, http://www.geofisica.unam.mx/ors/ors-red.html Instituto de Geofísica, Universidad Nacional Autónoma de México.

Organización Meteorológica Mundial (WMO), 1996, Guía de Instrumentación y Observaciones Meteorológicas, Geneva, Switzerland.

Organización Meteorológica Mundial (WMO), 1994, The International Programme on Chemical Safety (IPCS), Environmental health criteria, 160, Geneva, Switzerland.

Peeters P., Müller J.-F., Simon P.C., Gillotay D., Celarier E.A., Herman J.R., 2000, Monitoring surface UV-B irradiance from space using GOME; comparisons with ground-based measurements, Advances in Space Research, 26, 12, pp 1941-1947.

Sistema de Monitoreo Atmosférico de la Ciudad de México, 2008, http://www.sma.df.gob.mx/simat/.

Solar Light Co., Inc., 1991, *UV- Biometer, User's Manual 501*, Solar Light Co. Inc.

Soon W., Dutta K., Legates D.R., Velasco V., Zhang W.J., 2011, Variation in surface air temperature of China during the 20th century, Journal of Atmospheric and Solar-Terrestrial Physics, 73, pp 2331-2344.

Torrence C., Compo G.P., 1998, *A Practical Guide to Wavelet Analysis*. Bull. Amer. Meteor. Soc., 79, pp 61–78.

University of Southern Queensland, Toowoomba, Australia, 2008, http://www.usq.edu.au/faculty/science/depts/biophysci/weather/biometer/biometer1.htm.

Geofísica Internacional (2013) 52-1: 43-58

Original paper

Total mercury in terrestrial systems (air-soil-plant-water) at the mining region of San Joaquín, Queretaro, Mexico

Sergio Martínez-Trinidad*, Gilberto Hernández Silva, Martha Elena Ramírez Islas, Juventino Martínez Reyes, Gregorio Solorio Munguía, Sara Solís Valdez and Rocío García Martínez

Received: Frebuary 27, 2012; accepted: August 08, 2012; published on line: Decemebr 14, 2012

Resumen

La deficiente minería de cinabrio dejó a San Joaquín altas concentraciones de mercurio en terreros de mina (2.4 – 4164 mg kg^{-1}). Numerosas minas contribuyeron a la dispersión de mercurio en suelos agrícolas (0.5 – 314 mg kg^{-1}) y suelos forestales (0.2 – 69.0 mg kg^{-1}). Los sedimentos son un medio de transporte natural del mercurio, que ocasionan su dispersión, especialmente en áreas cercanas a las bocaminas (0.6 – 687 mg kg^{-1}). La cercanía de los cultivos de maíz a las minas favorece la acumulación de mercurio en sus distintas estructuras como la raíz, el tallo, la hoja y el grano (0.04 – 8.2 mg kg^{-1}), que se relacionan con la acumulación y volatilización de mercurio en suelos. El vapor de mercurio presente en la población puede indicar una volatilización constante de los terreros y suelos (22 – 153 ng m^{-3}). Los niveles de mercurio encontrados en suelos, en los granos de maíz y en el aire resultaron superiores a los estándares reportados por la Norma Oficial Mexicana y la Organización Mundial de la Salud. El mercurio en el agua de lluvia se debe principalmente a las partículas atmosféricas suspendidas y depositadas más tarde en la superficie (1.5 – 339 $\mu g\ l^{-1}$). En el agua potable se encontró disolución de mercurio (10 – 170 ng l^{-1}), siendo las concentraciones menores a las establecidas por la NOM Y OMS. La contaminación existente en la región de San Joaquín no llega a los niveles de los máximos productores de Hg en el mundo: Almadén (España) e Idrija (Eslovenia); sin embargo, se asemeja a la hallada en otros importantes distritos de segundo nivel mundial como Guizhou (China). La población de San Joaquín y su ambiente presentan una exposición constante a la contaminación del mercurio, por lo que es necesario un monitoreo a largo plazo para determinar sus alcances, en especial para el hombre.

Palabras clave: mercurio, suelos, sedimentos, terreros de mina, maíz, agua potable, lluvia, aire, San Joaquín, México.

S. Martínez-Trinidad
Posgrado en Ciencias de la Tierra
Centro de Geociencias
Campus UNAM - Juriquilla
Blvd. Juriquilla 3001, 76230
Querétaro, México
*Corresponding author:
sergiomtzt@geociencias.unam.mx

G. Hernández Silva
J. Martínez Reyes
G. Solorío Munguía
S. Solís Valdez
Centro de Geociencias
Campus UNAM - Juriquilla
Blvd. Juriquilla 3001, 76230
Querétaro, México
Email: ghsilva@geociencias.unam.mx

M.E. Ramírez Islas
Centro Nacional de Investigación y Capacitación Ambiental
Instituto Nacional de Ecología
Periférico 5000, Colonia Insurgentes Cuicuilco
Delegación Coyoacán, 04530
México, D.F., México

R. García Martínez
Centro de Ciencias de la Atmósfera
Universidad Nacional Autónoma de México
Ciudad Universitaria
Delegación Coyoacán, 04510
México, D.F., México

Abstract

Deficient management of cinnabar mining left the San Joaquín region with high concentrations of mercury in its soils (2.4 – 4164 mg kg^{-1}). Numerous cinnabar mines have contributed to the dispersion of mercury into agricultural (0.5 – 314 mg kg^{-1}) and forest (0.2 – 69 mg kg^{-1}) soils. Sediments are a natural means of transportation for mercury, causing its spreading, especially in areas near mine entrances (0.6 – 687 mg kg^{-1}). The nearness of maize crops to mines favors mercury accumulation in the different plant structures, such as roots, stems, leaves, and grain (0.04 – 8.2 mg kg^{-1}); these being related to mercury volatilization and accumulation in soils. Mercury vapor present in the settlements could indicate a constant volatilization from lands and soils (22 – 153 ng m^{-3}). The mercury levels found in the soils, in maize grain, and in the air resulted greater than the standards reported by the Official Mexican Norm (NOM) and the World Health Organization (WHO). Mercury in rainwater is due mainly to the presence of suspended atmospheric particles, later deposited on the surface (1.5 – 339 μg l^{-1}). Mercury dissolution was found in the drinking water (10 – 170 ng l^{-1}), with concentrations below those established by the NOM and the WHO. The contamination existing in the San Joaquín region does not reach the levels of the world's greatest mercury producers: Almaden (Spain) and Idrija (Slovenia). It is, however, like that found in other important second degree world producers such as Guizhou (China). The population of San Joaquín, as well as its surrounding environment, are constantly exposed to mercury contamination, thus making a long term monitoring necessary to determine its effects, especially to people.

Key words: mercury, soils, sediments, mining tailings, maize, drinking water, rain, air, San Joaquín, Mexico.

Introduction

Mercury is an element that is toxic for humans and which could be the cause of chronic diseases in the population of San Joaquín, Querétaro, Mexico. Exposure to mercury, even at low levels, is related to acute and chronic intoxication, resulting in a series of diseases that include neurological, heart attacks, central nervous system damage, kidney injuries, and autism (Li *et al*., 2008; Bose-O'Reilly *et al*., 2010). It also affects the biota and, therefore, affects the trophic chain (UNEP, 2002). In the study region, there exist very high mercury levels, beyond any standard in both humans and the environment; e.g. in bones of pre-Hispanic population (17.6 ppm), in agricultural soils (314.6 ppm), in mining tailings (4164.4 ppm), in drinking water (2 ppt), and in the air (414.8 ng m^{-3}) (Hernández-Silva *et al*., 2009).

In the environment, mercury is found naturally as cinnabar (HgS), but human activities such as mining, increases its presence within the atmospheric, terrestrial, biotical and aquatic systems (Mason, 2002; Selin, 2009). The effect of cinnabar mining represents an environment concern, since abandoned and enriched open air mining tailings are considered permanent sources of atmospheric mercury emissions. The mine drainage could contain high levels of mercury that affect the water and biota quality; therefore, cinnabar tailings increase the mercury content of the soils and sediments of the hydrographic watershed (Rytuba, 2000; Kocman and Horvat, 2011).

The mining activity has been developed since the pre-Hispanic period, because their inhabitants used cinnabar as colorant and in their religious ceremonies. Additionally, this region was a very important mercury production zone in the 60's and 70's of the last century. Mexico occupied the 4th place in production worldwide (Langenscheidt, 2006); presently, mercury mining is forbidden.

Through diverse processes such as rock weathering, erosion, lixiviation, oxidation and transportation, mercury may become established in the environment or be transported across great distances, becoming a legacy associated to soil, sediments and plants. Even after many years of mining inactivity, high amounts of mercury can be found in the environment (Parsons and Percival, 2005; García-Sánchez *et al*., 2009). On the other hand, man can be the receptor of mercury through inhalation of air particles, direct contact, or ingestion through the accumulation of this element in the trophyc chain. These mechanisms have operated in past and present times (Wasserman *et al*., 2003; Pyatt *et al*., 2005).

The objective of this work was to establish the impact caused by cinnabar mining in terrestrial systems (air-soil-plant-water) at the mining district of San Joaquín, and compare these values with concentrations reported in other highly contaminated places.

Materials and Methods

Study area

The mining region lies in the south of the Sierra Gorda of Querétaro, Mexico. It comprises 172 km^2 and is located between 99°40' and 99°30' W longitude, and 21°10' and 20°50' N latitude.

The delimitation of the study area was done by criterion of the hydrological watershed (Figure 1); the characteristics of geology, relief and edaphology; climate and vegetation were also considered. Here is a reference framework for the selection of sampling sites (Figure 2 y Figure 3).

Hg in mine tailings, soils, and sediments

Each sampling site of soils and tailings represents a sample made up of 5 subsamples taken at distances of 50 m each, and a depth of 0-25 cm. Sediment samples were collected from 100 m sections along some streams, rivers, and small alluvial terraces. Tailings were sampled from skarn and hydrothermal type mines. Soil sampling was done in function of the two predominant soil uses in the region: the forest area and agriculture. A total of 13 samples were taken from agricultural soils, 26 from forest soils, 27 from tailings, and 27 from sediments. All the samples were air dried at room temperature and sifted in a No.10 sieve (2mm). Part of the sample was ground down with an agate mortar to obtain a fine and homogeneous sample. From each sample, 0.1 g was weighed, in triplicate, and placed in a direct measure advanced mercury analyzer AMA-254, which uses an incineration technique generating mercury vapor. It is an atomic absorption spectrometer to determine mercury in solid or liquid samples without any previous treatment. Calibration of the equipment was done with standards from the MOSTAR Hungarian stream sediment standard, Slovakian reference material (ISE 982), and WEPAL monitor simple (ISE 921).

Hg in maize plants

Like in the rest of the country, the San Joaquín population consumes maize as its staple food, grown in their own seasonal rainfed plots, some of them located close to the mines. Sampling was done in the harvest time, in three different periods, October 2006 and November 2007

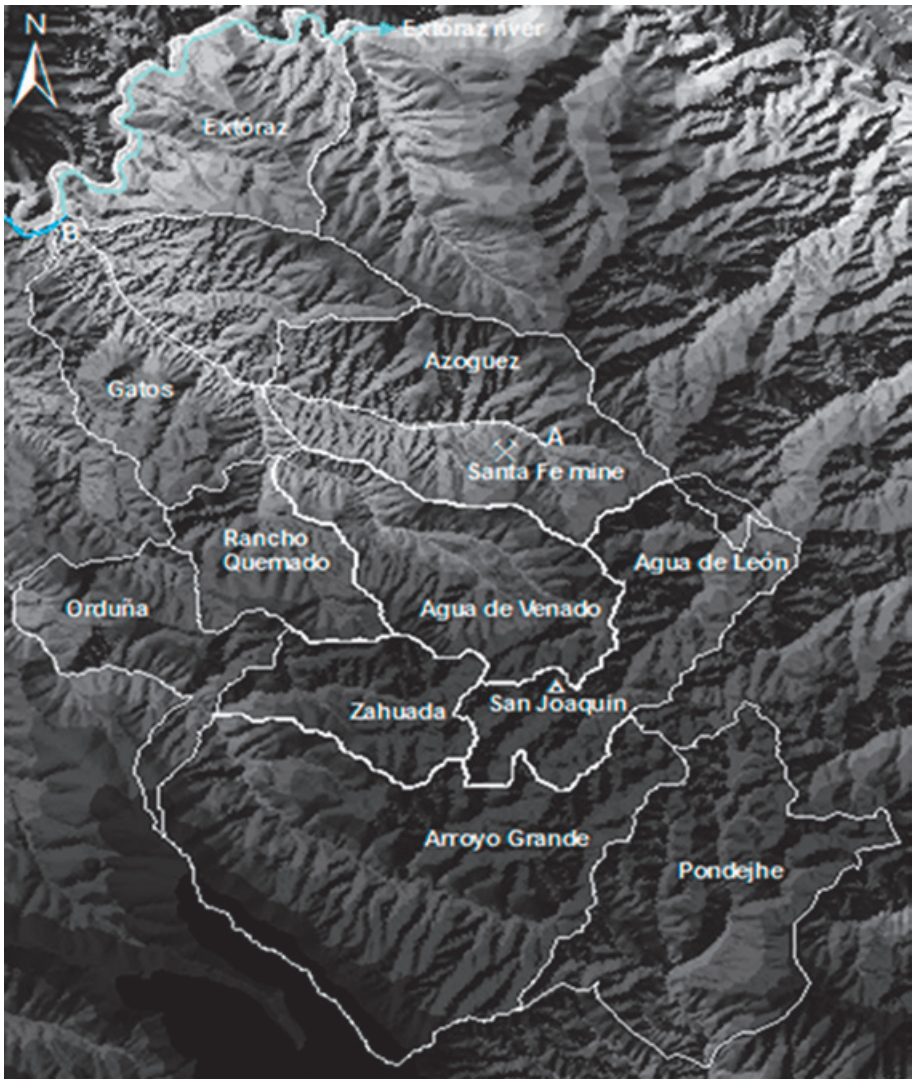

Figure 1. Micro-watersheds in the San Joaquín region. Azogues stream from its origin (A) to its river mouth with the Extóraz river (B).

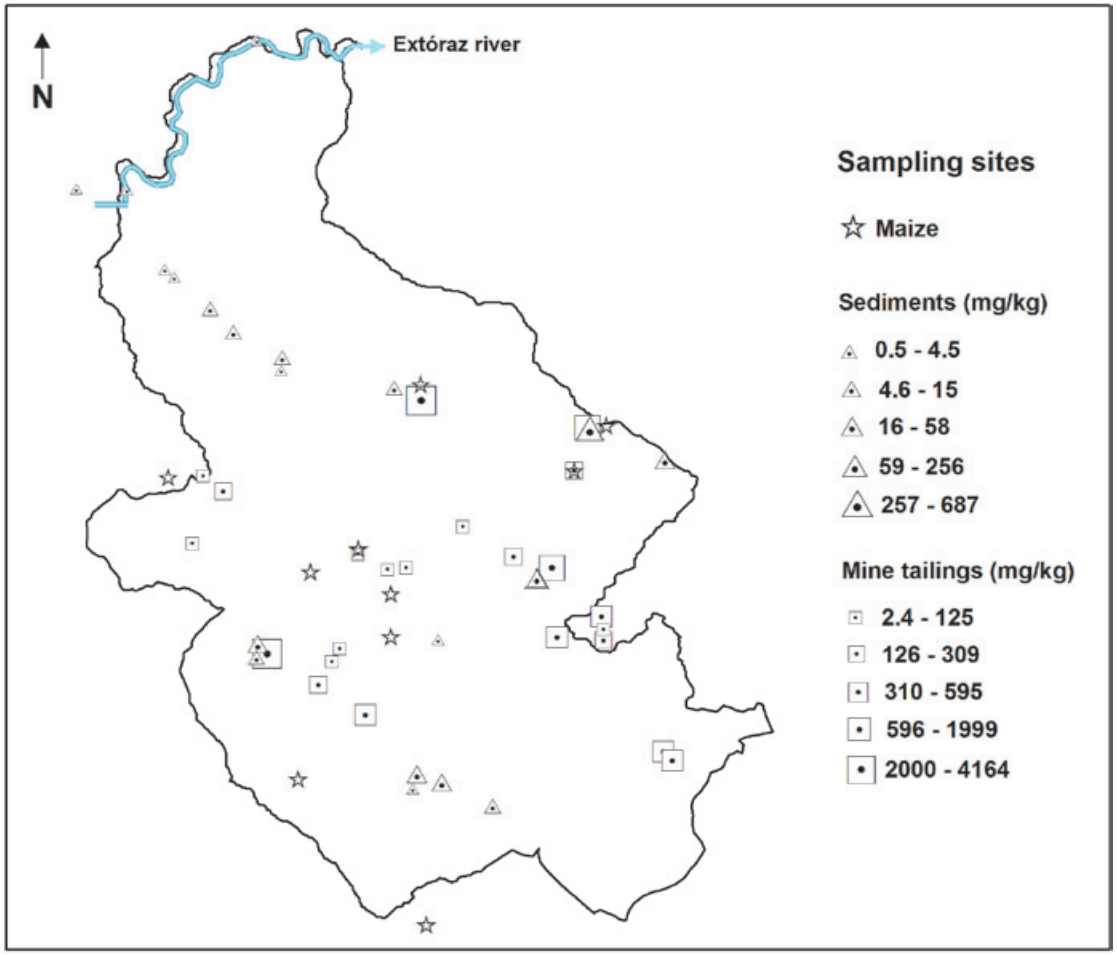

Figure 2. Sampling sites for mine tailings, sediments, and maize in the San Joaquín region. The symbol size in mine tailings and sediments indicates the concentration of mercury.

and 2010. Maize plants were collected from agricultural lands, and separated by structures into root, stalk, leaf, and grain; obtaining 15 samples from roots, 17 from stems, 11 from leaves, and 18 from grains. Each structure was washed with HNO_3 diluted to 10%, rinsed with deionized water, and dried at room temperature (22°-25°C). The plant material was ground and sifted until achieving particle size under 0.13 mm. Then, 0.1 g was weighed and 5 ml concentrated HNO_3 was added for digestion through a MARSPRESS microwave oven. Some drops of concentrated HCl were added to the digestion and taken to volume to 200 ml with 18.2 µS/cm deionized water. They were kept at 4°C until measurement. Total mercury quantification was done through induction coupled plasma mass spectrometry (ICP-MS) equipment Thermos Series X2.

Hg in rainwater

At the micro-watershed of Agua de Venado, Agua de Leon and Pondejhe of the study zone, rainwater collectors were installed for total mercury quantification. Information was also collected from a meteorological station in order to determine the predominance of the wind directions. Sample collection of rainwater was compound; each sample included water from all the events in a month. Twenty-four samples were collected from December 2009 to June 2010. The rainwater samples were filtered through a polycarbonate membrane with 0.4 µm pores, using a magnetic filtration system (Gelman 47-mm). The filtrate was acidified to pH = 1.8 with HNO_3 0.016N, and 60 ml from the sample was transferred to high density polyethylene bottles; thus, the soluble fraction

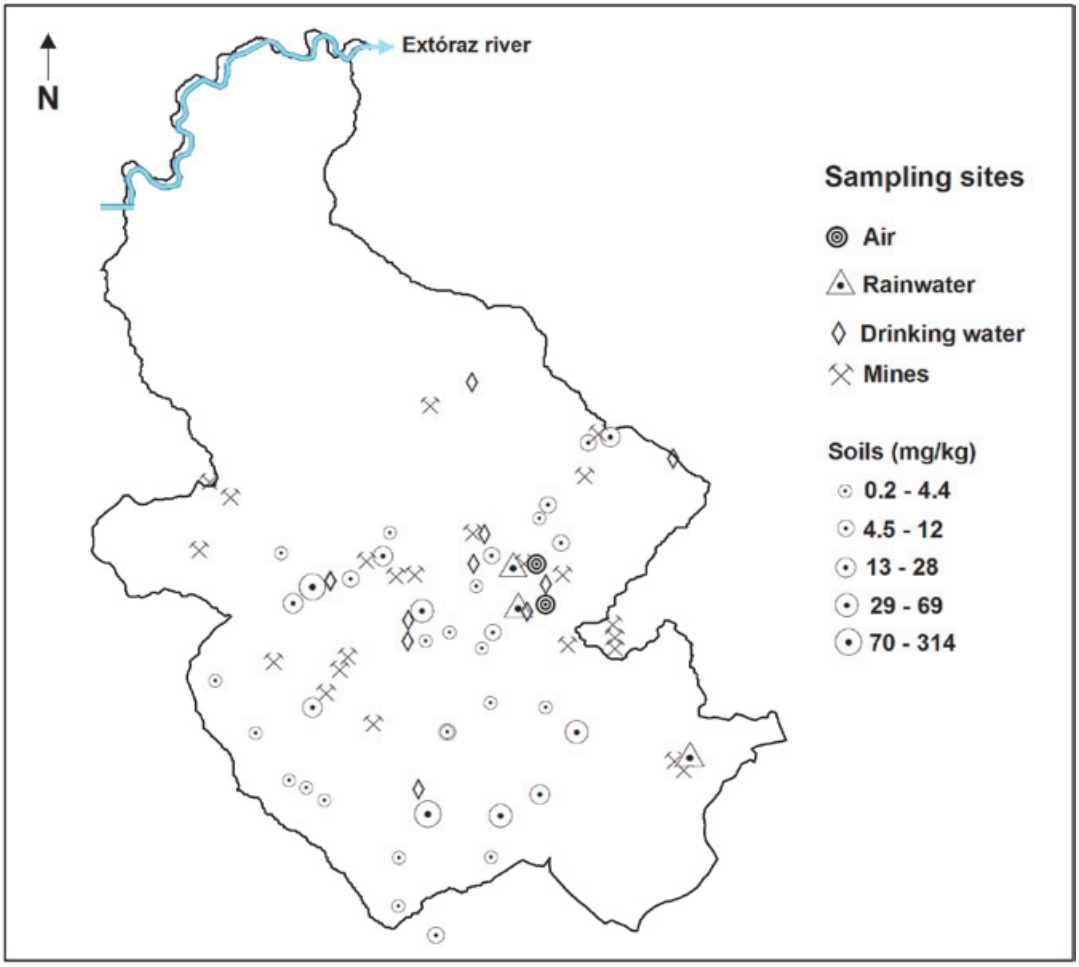

Figure 3. Sampling sites for air, rainwater, drinking water and soils in the San Joaquín region. The symbol size in soils indicates the concentration of mercury.

was obtained. The insoluble fraction is the part that remained on the filters used for the filtration process of the soluble fraction. These filters were subjected to acid digestion using 15 ml HNO_3 3M with a digestion time of 45 minutes in a MARSPRESS microwave oven. The digested samples were filtered and taken to volume to 25 ml with deionized water, obtaining a final HNO_3 acidity of 0.45N. Both fractions (soluble and insoluble) were refrigerated and kept at 4°C until quantification. Total mercury concentration was determined through inductively coupled plasma optical emission spectrometry (ICP-OES) equipment 710-ES Axial.

Hg in drinking water

Drinking water was sampled from nine settlements in the San Joaquín municipality during March and November, 2007, obtaining a total of 18 samples. The samples were collected in decontaminated nalgene bottles. Preservation of the samples was done with INSTRA nitric acid and they were refrigerated at 4°C until measurement. Total mercury quantification was done through induction coupled plasma mass spectrometry (ICP-MS) equipment Thermo Series X2.

Hg in air

The atmospheric mercury concentrations (elemental mercury in vapor phase) were measured in two sampling sites; the first one was established within the San Joaquín community taking samples continuously for 17 days (March 2011); while the second was located at the Agua de Venado area with 21 days straight measuring (April-May 2011). A TEKRAN 2537A model equipment, facilitated by CENICA INE, was used to determine ultra-trace mercury vapor.

Statistical analysis

Descriptive statistical analyses for total mercury content in the data base coming from mining tailings, soils, sediments, maize plants, rainwater, and air samples were taken into consideration. This analysis allows to determine the extent of contamination by mercury within each environmental component, as well as the detection of its maximum and minimum thresholds. For a better understanding of mercury distribution in each component, box and whiskers diagrams were used through STATISTICA Version 10 software.

Results and discussion

Mercury presents constant flow interactions within the different environmental compartments (atmospheric, terrestrial, aquatic, biotic), causing its mobilization, aspect that has influence on the quality of the environment and health of humans, while, the toxic grade is directly related to the mercury chemical phase that is found in each compartment.

Total mercury contents in the different compartments of the San Joaquín region are shown in Figure 4. This image shows the insertion dynamics of mercury in the different components. Mercury concentrations in each component change substantially, and it can be seen that the greatest contamination source of mercury is found in the open air mining tailings, adding a deficient processing of cinnabar. These tailings are exposed to climatic conditions as well as air and water erosion, which transport mercury particles both to the atmospheric and terrestrial landscape. This has repercussions on the concentration levels of mercury present in air, rainwater, forest and agricultural soils, as well as and in sediments.

The presence of crops, especially maize, near the entrance of the mines is very common. Thus the plants are exposed to mercury, accumulating it in the different structures (roots, stems, leaves, and grains). Mercury in drinking water has a direct link to human beings, and constant consumption could have some repercussion in the long term (WHO-IPCS, 2004; Cabrera-Vique *et al*., 2007). In this paper, the causes of mercury distribution are examined and the obtained concentrations are compared with other references, considered as sites with high mercury contamination (Table 1).

Total Hg in mining tailings

Hydrothermal tailings show total mercury contents ranging from 2.4 to 4164 mg kg^{-1}. It can be seen the range is quite extended; however, most concentrations are somewhere around the median (233 mg kg^{-1}), being the upper limit an extreme value in the region. As expected, the

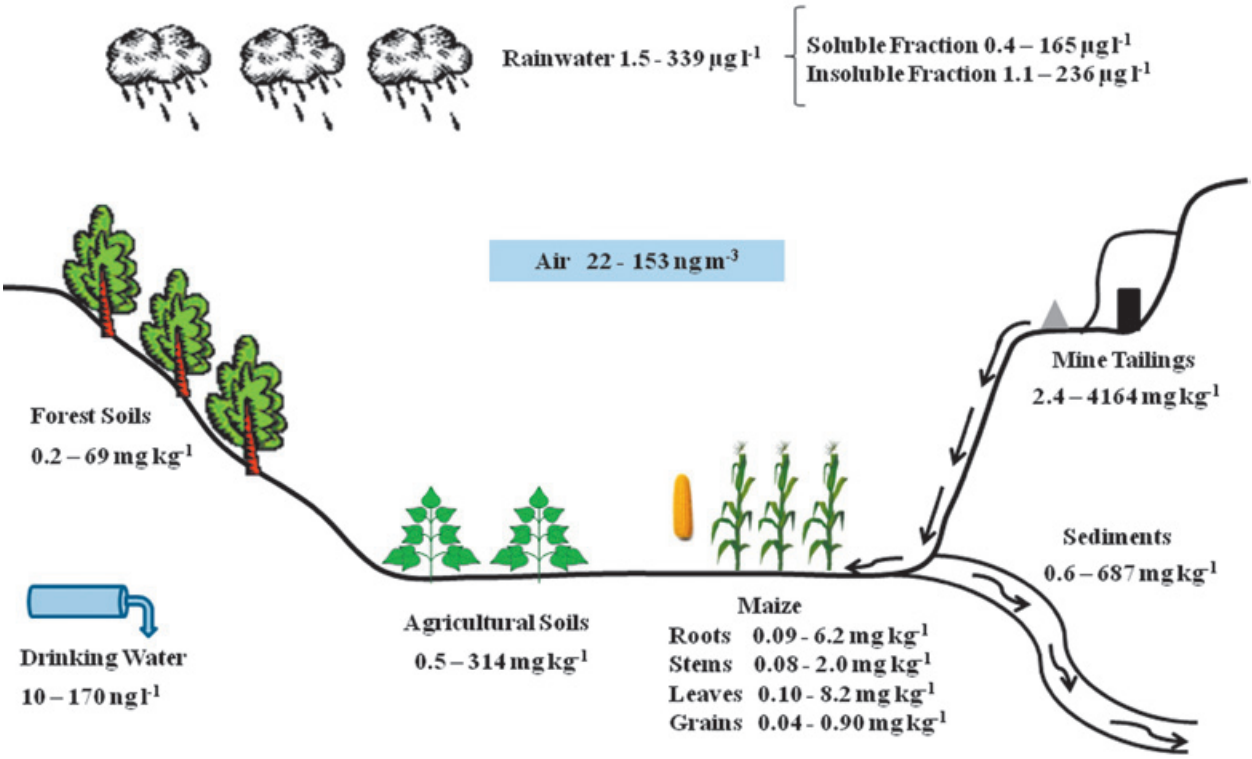

Figure 4. Distribution of total mercury content in the different compartments of the San Joaquín region.

skarn type tailings presented a lower mercury concentration than the hydrotermals, since they present concentrations from 3.7 to 25.6 mg kg^{-1}. Through time, the tailings get mixed with the soil; these kinds of materials showed high content of total mercury, ranging from 14.6 to 1448 mg kg^{-1} (Table 2). These amounts of mercury could be due to inefficient and incomplete cinnabar processing, possible re-absorption of mercury, and direct exposure of the chimney during several years (Biester *et al*., 1999; Navarro *et al*., 2009).

Nevertheless, considering the NOM (2004) with regard to concentration levels to be considered as contaminated soil (> 23.0 mg kg^{-1}), it is observed that 37% of the tailing samples analyzed showed mercury concentrations greater than the limit allowed for industrial use 310 mg kg^{-1} (Figure 5). Mercury concentration in tailings gives the San Joaquín region a high level of contamination. There are a great number of open air mining tailings, located in the surrounding areas of the abandoned mines, becoming a serious risk to people and the environment.

The highest total mercury concentration (4164 mg kg^{-1}) was similar to that reported by Qiu *et al*. (2005, 2006) in the mining district of Guizhou, China (4400 mg kg^{-1}), but lower than that of Almaden, Spain (34,000 mg kg^{-1}), considered as the place most contaminated by mercury on Earth (Higueras *et al*., 2003).

Total Hg in soils and sediments

Total mercury concentration in agricultural soils is distributed in a wide range, going from 0.5 to 314 mg kg^{-1} (Table 2), where the highest registered value clearly indicates mercury incorporation into the landscape soils. According to the NOM (2004), 46% of the soil samples analyzed showed mercury concentrations greater than the maximum limit established for agricultural use, 23 mg kg^{-1} (Figure 5).

The results show that the variations in mercury content in forest soils are lower than the maximum ranges found in agricultural soils. This could be due to the soil processes involved, whether favoring mercury adsorption or hindering its volatilization and/or transformation. Mercury accumulation in forest soils is attributed to the content of organic matter present in the organic horizon (Lacerda *et al*., 2004; Ettler *et al*., 2007); with a higher content of organic matter, the soil will have a higher capability to retain mercury.

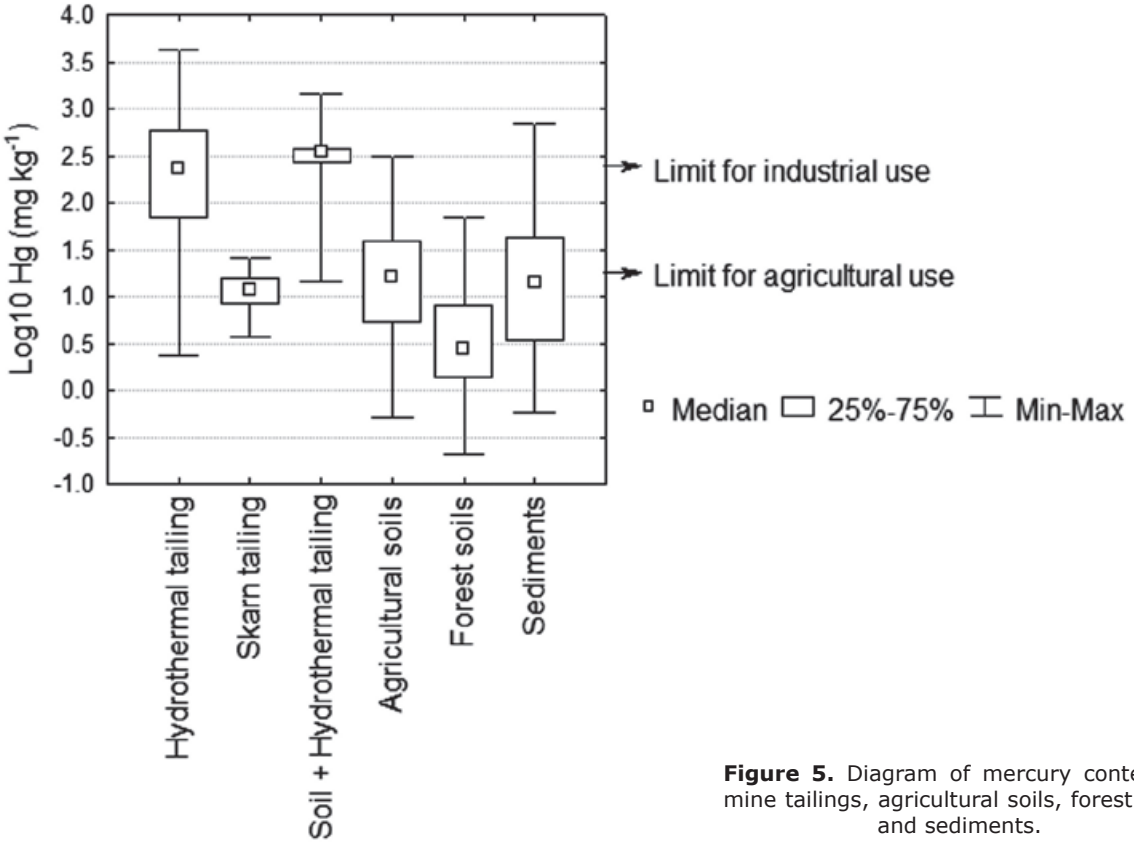

Figure 5. Diagram of mercury content in mine tailings, agricultural soils, forest soils, and sediments.

Table 1. Total mercury content in the components of different mining zones of the world well known for their mercury production.

Component	Location	Total Hg	References
Mine waste - mine tailings			
	Almaden, Spain	160 - 34000 mg kg^{-1}	Higueras *et al*. (2003)
	Idrija, Slovenia	42.6 – 1640 mg kg^{-1}	Biester *et al*. (1999)
	Wuchuan, Guizhou, China	5.7 – 4400 mg kg^{-1}	Qiu *et al*. (2005, 2006)
	San Joaquín, Qro., Mexico	2.4 – 4164 mg kg^{-1}	This study
Soils			
	Almaden, Spain	6.0 – 8889 mg kg^{-1}	Higueras *et al*. (2003
	Idrija, Slovenia	0.39 – 2759 mg kg^{-1}	Gnamusˇ *et al*. (2000)
	Wuchuan, Guizhou, China	0.33 – 790 mg kg^{-1}	Qiu *et al*. (2005, 2006)
	San Joaquín, Qro., Mexico	0.2 – 314 mg kg^{-1}	This study
Stream sediments			
	Almaden, Spain	0.5 – 16000 mg kg^{-1}	Higueras *et al*. (2006)
	Idrija, Slovenia	5.0 – 1000 mg kg^{-1}	Gosar *et al*. (1997)
	Wanshan, Guizhou, China	1.1 – 480 mg kg^{-1}	Lin *et al*. (2010)
	San Joaquín, Qro., Mexico	0.6 – 687 mg kg^{-1}	This study
Maize			
	Tongren, Guizhou, China	0.41 mg kg^{-1} (grain)	He *et al*. (1998)
	Tongren, Guizhou, China	1.58 mg kg^{-1} (leaf)	He *et al*. (1998)
	Wuchuan, Guizhou, China	0.026 – 0.56 mg kg^{-1}	Qiu *et al*. (2006)
	San Joaquín, Qro., Mexico	0.04 – 8.2 mg kg^{-1}	This study
Rainwater			
	Idrija, Slovenia	3.15 – 24.4 ng l^{-1}	Kocman *et al*. (2011)
	Wujiang, Guizhou, China	0.19 – 36 ng l^{-1}	Guo *et al*. (2008)
	San Joaquín, Qro., Mexico	1.5 – 339 μg l^{-1}	This study
Air			
	Almaden, Spain	100 - 14000 ng m^{-3}	Higueras *et al*. (2006)
	Idrija, Slovenia	<10 – 5000 ng m^{-3}	Kocman *et al*. (2011)
	Wanshan, Guizhou, China	17.8 – 1101.8 ng m^{-3}	Wang *et al*. (2007)
	San Joaquín, Qro., Mexico	22 – 153 ng m^{-3} the community)	This study (measures in
Stream water			
	Almaden , Spain	7.6 - 20300 ng l^{-1}	Berzas Nevado *et al*. (2003)
	Idrija, Slovenia	2.8 – 322 ng l^{-1}	Horvat *et al*. (2002)
	Wuchuan, Guizhou, China	22 – 360 ng l^{-1}	Qiu *et al*. (2006)
	San Joaquín, Qro., Mexico	10 - 170 ng l^{-1}	This study (Drinking water)

The land relief of the study region could be an important factor in mercury distribution, given that the forest areas are in a slope >15°, which makes them more susceptible to erosion processes, while agricultural areas are next to forest areas, and therefore are receptors of the mercury eroded by surface runoff. Almeida *et al*. (2005) mentions that hydric erosion favors re-mobilization of mercury in the surface soil layer.

Moreover, Hernández-Silva *et al*. (2009) mention that pre-Hispanic agriculture and mining could have been associated in their everyday activities, influencing mercury insertion into agricultural soils near the mines. The soils presented lower mercury contents than those of Idrija, Slovenia (0.39-2759 mg kg^{-1}), Guizhou, China (0.33-790 mg kg^{-1}), and Almaden, Spain (6.0 – 8889 mg kg^{-1}) (Gnamusˇ *et al*., 2000; Higueras *et al*., 2003; Qiu *et al*., 2005).

Total mercury concentrations in sediments varied from 0.6 to 687 mg kg^{-1} (Table 2). According to the obtained values, the mercury content in sediments has a mean value almost equal to the upper limit of the mercury concentration in forest soils, and slightly greater than the mean of agricultural soils. Sediments are a natural means of transportation of mercury loads, causing its dispersion into the drainage network. Several authors (Hines *et al*., 2000; Feng and Qiu *et al*., 2008; Lin *et al*., 2010) point out that mercury concentrations in sediments tend to decrease as they are further from the source of contamination as is demonstrated in Figure 2. The range of total mercury concentrations was similar to that found in Guizhou, China (1.1-480 mg kg^{-1}), but lower than those found in the mining districts of Idrija, Slovenia (5.0-1000 mg kg^{-1}), and Almaden, Spain (0.5-16000 mg kg^{-1}) (Gosar *et al*., 1997; Higueras *et al*., 2006; Lin *et al*., 2010).

Total Hg in maize crops

The concentrations of total mercury in the different structures of the maize plants are showed in Table 3. The structures (root, stalk and leaves) close o the mines presented a higher concentration of total mercury than those which are located farther from them, while there was no difference in the maize grain (Figure 6). The maximum concentrations in leaves (8.2 mg Kg^{-1}) and in the grains (0.9 mg Kg^{-1}) resulted higher than those reported by He *et al*. (1998); being in leaf 1.58 mg kg^{-1} and in grain 0.41 mg kg^{-1}. The total mercury concentrations found in maize plants (0.04-8.2 mg kg^{-1}) were greater than those found by Qiu *et al*. (2006) in the mining area of northeast Guizhou, China (0.026-0.57 mg kg^{-1}). In general, there was a greater total mercury accumulation in roots and leaves than in stems and grains.

Table 2. Descriptive statistic of mercury content in mine tailings, agricultural soils, forest soils, and sediments (mg/kg).

	Hydrothermal tailing	Skarn tailing	Soil + Hydrothermal Tailing	Agricultural soils	Forest soils	Sediments
N	18	5	5	13	26	27
Minimum	2.4	3.7	14.6	0.5	0.2	0.6
Maximum	4164	25.6	1448	314	69	687
Mean	721	13	488	53	8.5	67.5
Median	233	12	346	16	2.8	14
Standard Deviation	1162	8.2	554	92	15.5	148

N = Number of samples; the maximum limit established for agricultural use 23 mg kg^{-1} and industrial use 310 mg/kg (NOM, 2004).

Table 3. Total mercury in maize plant structures, samples collected near and far from the mines (mg kg^{-1}).

	Near mines[a]				Far from mines[b]			
	Root[a]	Stalk[a]	Leaf[a]	Grain[a]	Root[b]	Stalk[b]	Leaf[b]	Grain[b]
N	7	8	6	8	8	9	5	10
Minimum	0.1	0.1	0.1	0.07	0.09	0.08	0.2	0.04
Maximum	6.2	2.0	8.2	0.8	3.9	1.0	4.0	0.9
Mean	1.8	0.8	1.9	0.2	1.3	0.4	1.3	0.3
Median	0.5	0.8	0.6	0.1	0.6	0.3	0.5	0.2
Standard Deviation	2.4	0.5	3.1	0.2	1.4	0.3	1.5	0.2

N = Number of samples; the maximum limit established for maize grain 0.5 mg kg^{-1} and 0.1 mg kg^{-1} for animal feed (WHO-IPCS, 2004; Sierra *et al*., 2009).

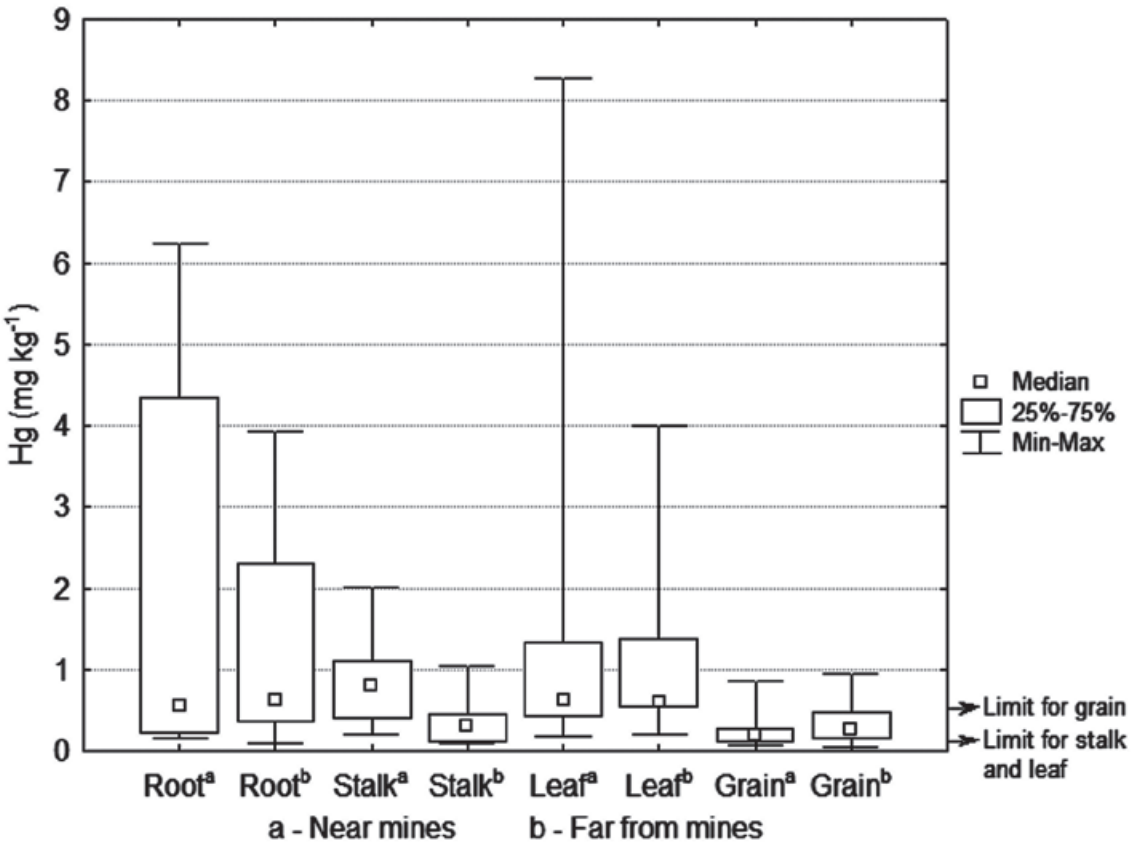

Figure 6. Diagram of mercury content in maize plants.

Plants assimilate organic and inorganic mercury through their radicle system and transport it to the foliage (Hanson *et al*., 1995). Also, Temmerman *et al*. (2009) indicate that mercury absorption through plant roots is proportional to the exposition concentration in the soil. Stamenkovic and Gustin (2009) suggest that mercury absorption in foliage occurs through the stomas, and that the accumulation is positively correlated to mercury atmospheric concentration. Another absorption mechanism happens with mercury dissolution in water, incorporating it into foliar tissue (Rea *et al*., 2004). Atmospheric contamination could be the cause of mercury accumulation in most plants (Patra and Sharma, 2000; Temmerman *et al*., 2009).

The lowest mercury contents were found in the grains, given that when achieving plant maturity (at the end of harvest) mercury accumulation decreases (Patra and Sharman, 2000). The concentrations of mercury in the maize grain ranged from 0.04 to 0.9 mg kg^{-1}, obtaining higher values to those reported by the World Health Organization of 0.5 mg kg^{-1} (Figure 6), which is the maximum limit for mercury contaminated food making them unsuitable to be sold for human consumption. In the study region, the maize plant stalk and leaf are used as cattle forage. Sierra *et al*. (2009) mention that the European legislation establishes a limit of 0.1 mg kg^{-1} of mercury for animal feed. In this work, higher concentrations than this limit were found; e.g. for the stalk 2.0 mg kg^{-1} and for leaf 8.2 mg kg^{-1}. Bioaccumulation of mercury in maize crops is an entrance source of mercury into the food chain, through foliage consumption by cattle or grains by humans (Rothenberg *et al*., 2007).

The results show that roots and foliage were more susceptible to mercury accumulation; the former because of the exposition existing with mercury concentration in the soil, and the second due to the atmospheric mercury. However, Molina *et al*. (2006) and Temmerman *et al*. (2009) point out that bioaccumulation depends on the absorption mechanism of each plant species. This would explain why in some cases the absorption rate is constant and independent of mercury concentration in the soil; that there is no relationship between mercury content in the soil and in the plant; or that the bioaccumulation of mercury in the plant does not increase even if mercury concentration in the environment increases.

Total Hg in rainwater

The removal of a contaminant from the atmosphere can happen through precipitation (wet deposition) or by dry deposition (Duce *et al*., 1983). Total mercury concentrations in rainwater ranged from 1.5 to 339 μg l^{-1}, with a mean 96 μg l^{-1}; 60 μg l^{-1} corresponding to the insoluble fraction and 36 μg l^{-1} to the soluble fraction (Table 4 and Figure 7). This agrees with Kocman *et al*. (2011) since mercury joined with atmospheric particles represents over 50% of the total mercury in the deposition, and the remaining part is dissolved in rainwater. This could suggest that the particles dragged by wind are the main mechanism of atmospheric deposition of mercury in the study area.

Duce and Hoffman (1976) concluded that particle removal by rain is approximately twice that of dry deposition. Guo *et al*. (2008) and Kocman *et al*. (2011) report concentrations from 0.19 to 36 ng l^{-1} and 3.15 to 24.4 ng l^{-1} total mercury in the rainfall of mining zones, being lower those found in this study. This behavior is due to the fact that the samples were collected in 3 to 17 rain events, involving a higher accumulation of particulate material coming from wind erosion. The sampling sites close to the mines and the wind regressive trajectories at 500 m height, indicate that the air masses can drag the particles from the mine tailings, transporting and depositing them, thus causing the soils to be enriched with this pollutant (Figure 3).

Kocman *et al*. (2011) observed an increase in mercury concentration in the rainfall samples due to the presence of cinnabar particles, as a result of eolian erosion of the surfaces containing cinnabar in the area. Notwithstanding, the particles (aerosols) are not uniformly distributed in the atmosphere, neither spatially nor temporally. This originates differences in mercury deposition, which could explain the variations in the mercury concentration in each rain event.

The results in this study are in agreement with those reported by Guo *et al*. (2008) who found a positive correlation between precipitation and mercury concentration, establishing that in the rainy season there is a greater wet deposition of mercury. The climatic and orographic conditions of the region favor changes in humidity, temperature, and solar radiation, causing high mercury volatilization in land systems (Gustin *et al*., 2003; Johnson *et al*., 2003), which could be contributing to the concentrations of atmospheric mercury.

Hg in air

Gaseous elemental mercury is the main chemical mercury species released into the atmosphere, it is characterized for being very stable and having low water solubility; it volatilizes at room temperature and is relatively inert to chemical reactions with other atmospheric components. Its residence time is about one year, so once it is released to the atmosphere it can be dispersed or transported to greater distances before being re-deposited in the terrestrial and aquatic ecosystems (Schroeder and Munthe, 1998).

The chemical reactions and the partitioning of mercury in gas and aqueous phases appear to determine mercury residence times in the atmosphere and its deposition at various latitudes (Grandjean, 2008). Kocman *et al*. (2011) mention that mercury space distribution depends on wind conditions (direction, velocity); on the other hand, the emissions of mercury of the contaminated surfaces depend on temperature. Boening (2000) mentions that the environmental variables such as pH, redox potential, water chemical composition, soil type, and geology affect mercury absorption.

Measurements of total gaseous mercury (TGM) in the air are shown in Table 4. The daily average during the 38 days of measuring was 67 ng m^{-3}, mainly ranging between 40 and 100 ng m^{-3} (Figure 7). When comparing these concentrations with those reported by Grandjean (2008) in remote areas, of 2-3 ng m^{-3} in winter, allows to observe the amount of volatilization that exists within the study area. WHO-IPCS (2004) indicate that the mercury levels in air are in a range of 2-10 ng m^{-3}. The mercury values from 40 to 100 ng m^{-3} obtained in this study, indicate that the San Joaquín population is exposed to a high concentration of mercury in the air, which can be a health hazard.

In general, the concentrations of mercury in the air within the mining populations of Idrija, Slovenia (<10 ng m^{-3}), Guizhou, China (17.8 ng m^{-3}) and San Joaquín (22 ng m^{-3}) are lower than those reported for areas where cinnabar was melted to produce mercury, getting to concentrations from 1101 to 14000 ng m^{-3} (Higueras *et al*., 2006; Wang *et al*., 2007; Kocman *et al*., 2011). The maximum value of 153 ng m^{-3} observed in the San Joaquín community is higher than the value reported for the population of Almaden, Spain (100 ng m^{-3}).

Hg in drinking water

The forms of mercury in drinking water are not well studied, but the mercuric ion is probably the predominant species, present in complexes and chelates with ligands. From the ingestion of drinking water, a small fraction is absorbed. Although the existence of methilmercury has been pointed out in drinking water under certain

Table 4. Descriptive statistic of mercury content in rainwater, air, and drinking water.

	Rainwater (μg l^{-1})			Air (ng m^{-3})	Drinking water (ng l^{-1})
	Soluble	Insoluble	Soluble + Insoluble		
N	24	24	24	38	18
Minimum	0.4	1.1	1.5	22	10
Maximum	165	236	339	153	170
Mean	36	60	96	67	61.6
Median	5.6	22.6	28	49	60.0
Standard Deviation	50.2	67.4	113	37	42.5

N = Number of samples; the mercury levels in air are in a range of 2 to 10 ng m^{-3} (WHO-IPCS, 2004); the maximum limit established for drinking water 0.001 mg l^{-1} by the NOM (1994) and 6 μg l^{-1} by the WHO-IPCS (2004).

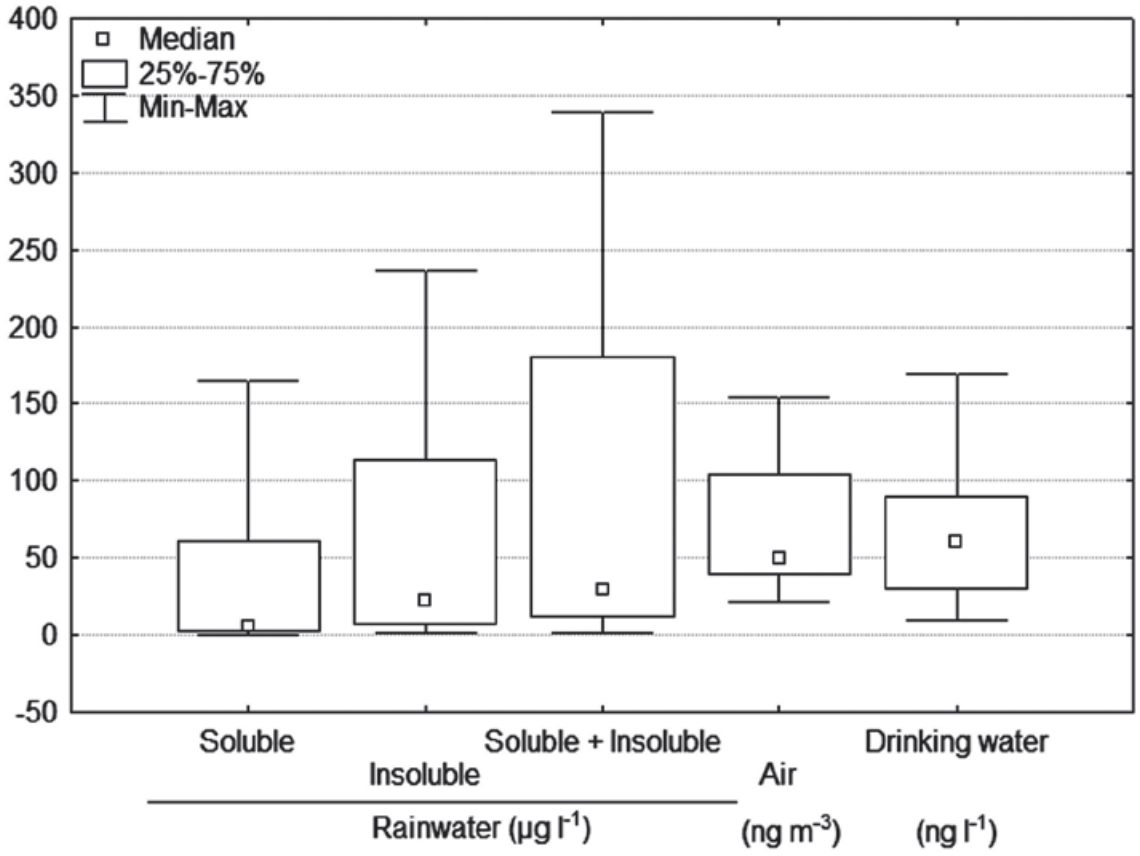

Figure 7. Diagram of mercury content in rainwater, air, and drinking water.

conditions, its presence is considered unusual enough (UNEP, 2002). Methylmercury is the result of the methylation of inorganic mercury by the microorganisms that are present in freshwater and saltwater bodies; this methylmercury produced is capable of entering the aquatic feeding chain and can be bio-accumulated within the muscular tissues of fish (Mason *et al*., 2005).

The total mercury concentrations in drinking water ranged from 10 to 170 ng l^{-1} (Table 4 and Figure 7). These contents are below the maximum limit, 0.001 mg l^{-1}, established by the NOM (1994) and the WHO-IPCS (2004) guideline value of 6 µg l^{-1}. This indicates that there is no problem in its use for human consumption. Grandjean (2008) mentions that in drinking water, the mercury concentrations are usually from 5 to 100 ng l^{-1}, becoming a minor public health concern, but the presence of mercury in the water phase in the environment can lead to serious problems, e.g. the intoxication occurred at the Minamata Bay, Japan in 1953 as a result of the ingestion of fish containing methylmercury coming from polluted waters (Harada, 1995; UNEP, 2002).

The values obtained were lower than those found in the stream water of Idrija, Slovenia (2.8 - 322 ng l^{-1}), Guizhou, China (22 - 360 ng l^{-1}), and Almaden, Spain (7.6 - 20300 ng l^{-1}) (Berzas Nevado *et al*., 2003; Horvat *et al*., 2002; Qiu *et al*., 2006). These studies point out the presence of mercury in the water, indicating high concentrations in areas surrounding abandoned cinnabar mines. Cabrera-Vique *et al*. (2007) suggest a strict vigilance of mercury content in drinking water given the alimentary habits of human beings, since they could be drinking great amounts of water.

Conclusions

The high production of mercury that happened in the region, especially in the 60's and 70's of the last century, left considerable consequences of open air mine tailings and whose dispersion is reflected in the diminishing of the quality of the different environmental compartments. The existing pollution in the San Joaquín region doesn't reach the levels of the world bigger producers of mercury: Almaden and Idrija (Slovenia); however, it is similar to the ones found in other important world second level mining districts such as: Guizhou (China).

A recurrent pattern of mercury dispersion in the landscape is the existence of high levels of mercury in soils, related to zones with a higher concentration of mine tailings, in which the management and deficient processing of cinnabar have been a constant situation. The dispersion of mercury in soils and sediments is controlled by the distance existing to the mines and the terrain slope that favors constant erosion, transporting mercury to the lower parts.

On the other hand, it is frequent to see at a short distance from the mine mouths and as an economical complement, the existence of plots with maize crops, predominantly, resulting the roots and leaves more susceptible to mercury accumulation, which results in the introduction of the element into the trophyc chain and its bio-accumulation which means a high risk for humans and fauna.

Mercury deposition in the rainwater is especially linked to the atmospheric particles that come from the mercury enriched soils, representing 63% of the deposition, the rest it is found in dissolved form. There exist mercury concentrations in the drinking water of the study area but it doesn't represent any risk to human health.

The presence of gaseous mercury circulating in the air allows to deduce that there is a continuous volatilization from the soils enriched with mercury. Therefore, the inhabitants keep a constant direct contact with this gas through inhalation. The levels found at the location are greater than the reported standards. These emissions influence mercury accumulation by maize plants.

Based on the previous, the population of San Joaquín and their environment both present a constant exposure to the pollution of mercury, so it is necessary to keep monitoring it in a long term to determine its scope.

Aknowledgments

This investigation is part of the project *PAPIIT-UNAM No. 22IN114910*. To the laboratory of soils of the *Centro de Geociencias*, *campus UNAM-Juriquilla*, Querétaro. To the Geology Institute of Hungary for the analysis performed with the AMA-254 equipment. To *Centro Nacional de Investigación y Capacitación Ambiental (CENICA) del Instituto Nacional de Ecología (INE)* for the analysis performed with the TEKRAN-2537A equipment. To *Consejo Nacional de Ciencia y Tecnología (CONACYT)* for the doctoral scholarship.

Bibliography

Almeida M.D., Lacerda L.D., Bastos W.R., Herrmann J.C., 2005, Mercury loss from soils following conversion from forest to pasture in Rondonia, Western Amazon, Brazil. Environmental Pollution, 137, 179-186.

Berzas Nevado J.J., García Bermejo L.F., Rodriguez Martin-Doimeadios R.C., 2003, Distribution of mercury in the aquatic environment at Almadén, Spain. Environmental Pollution, 122, 261–271.

Biester H., Gozar M., Müller G., 1999, Mercury speciation in tailings of the Idrija mercury mine. *Journal of Geochemical Exploration*, 65, 195–204.

Boening D.W., 2000, Ecological effects, transport, and fate of mercury; a general review. *Chemosphere*, 40, 1335-1351.

Bose-O'Reilly S., McCarty K., Steckling N., Lettmeier, B., 2010, Mercury exposure and children's health. Current Problems in Pediatric and Adolescent Health Care, 40, 186–215.

Cabrera-Vique C., Ruíz-López M.D., Javier F., 2007, Mercurio en aguas del sureste de España: posibles fuentes de contaminación. Ars Pharmaceutica, 48, 37-53.

Duce A.R., Hoffman G.L., 1976, Atmospheric vanadium transport to the ocean. Atmospheric Environment, 10, 989-996.

Duce A.R., Mohnen V.A., Zimmerman P.R., Grosjean D., Cautreels W., Chatfield R., Jaenicke R., Ogree J.A., Pellizari E.D., Wallace G.T., 1983, Organic material in the global troposphere. Reviews of Geophysics and Space Physics, 21, 921-952.

Ettler V., Rohovec J., Navrátil T., Mihaljevič M., 2007, Mercury distribution in soil profiles polluted by lead smelting. Bulletin of Environmental Contamination and Toxicology, 78, 12–16.

Feng X., Qiu G., 2008, Mercury pollution in Guizhou, Southwestern China — An overview. Science of The Total Environment, 400, 227-237.

García-Sánchez A., Murciego A., Álvarez-Ayuso E., Santa Regina I., Rodríguez-González M.A., 2009, Mercury in soils and plants in an abandoned cinnabar mining area (SW Spain). *Journal of Hazardous Materials*, 168, 1319-1324.

Gnamusˇ A., Byrne A.R., Horvat M., 2000, Mercury in the Soil-Plant-Deer-Predator food chain of a temperate forest in Slovenia. *Environmental Science and Technology*, 34, 3337-3345.

Gosar M., Pirc S., Bidovec M., 1997, Mercury in the Idrijca stream sediments as a reflection of mining and smelting activities of the Idrija mercury mine. *Journal of Geochemical Exploration*, 58, 125–131.

Grandjean P., 2008, Mercury. Institute of Public Health, University of Southern Denmark, Odense, Denmark; Department of Environmental Health, Harvard School of Public Health, Boston, MA, USA.

Guo Y., Feng X., Li Z., He T., Yan H., Meng B., Zhang J., Qiu G., 2008, Distribution and wet deposition fluxes of total and methyl mercury in Wujiang River Basin, Guizhou, China. Atmospheric Environment, 42, 7096–7103.

Gustin M.S., Coolbaugh M.F., Engle M.A., Fitzgerald B.C., Keislar R.E., Lindberg S.E., Nacht D.M., Quashnick J., Rytuba J.J., Sladek C., Zhang H., Zehner R.E., 2003, Atmospheric mercury emission from mine wastes and surrounding geologically enriched terrains. Environmental Geology, 43, 339-351.

Hanson P.J., Lindberg S.E., Tabberer T.A., Owens J.G., Kim K-H., 1995, Foliar exchange of mercury vapor: evidence for a compensation point. Water, Air and Soil Pollution, 80, 373–382.

Harada M., 1995, "Minamata disease: Methylmercury poisoning in Japan caused by environmental pollution". Critical Reviews in Toxicology, 25, 1, 1-24.

He J., Tan H., Sommar J., Xiao Z., Lindqvist O., 1998, Mercury pollution in a mining area of Guizhou, China: fluxes over contaminated surfaces and concentrations in air, biological and geological samples. *Toxicological and Environmental Chemistry*, 67, 225-236.

Hernández-Silva G., 2009, Mercurio: impacto en el hombre y la naturaleza, al sur de la Sierra Gorda de Querétaro, México. Centro de Geociencias, campus UNAM-Juriquilla, Querétaro. México.

Hernández-Silva G., Scharek P., Bartha A., Solorio-Munguía G., Vasallo-Morales L., Lugo-de la Fuente J., Tullner T., Centeri C., Martínez-Reyes J., 2009, Mercurio en suelos, sedimentos y terreros al sur de la Sierra Gorda de Querétaro, México. En: Mercurio: impacto en el hombre y la naturaleza, al sur de la Sierra Gorda de Qro. México, Hernández-Silva G. (Ed.). Centro de Geociencias, campus UNAM-Juriquilla, Querétaro. México.

Higueras P., Oyarzun R., Biester H., Lillo J., Lorenzo S., 2003, A first insight into mercury distribution and speciation in soils from the Almadén mining district, Spain. *Journal of Geochemical Exploration*, 80, 95-104.

Higueras P., Oyarzun R., Lillo J., Sánchez-Hernández J.C., Molina J.A., Esbri J.M., Lorenzo S., 2006, The Almadén district, Spain: anatomy of one of the world's largest Hg-contaminated sites. Science of The Total Environment, 356, 112–124.

Hines M.E., Horvat M., Faganeli J., Bonzongo J-C J., Barkay T., Major E.B., Scott K.J., Bailey E.A., Warwick J.J., Berry Lyons W., 2000, Mercury biogeochemistry in the Idrija river, Slovenia, from above the mine into the Gulf of Trieste. Environmental Research, 83, 129-139.

Horvat M., Jereb V., Fajon V., Logar M., Kotnik J., Faganeli J., Hines M.E., Bonzongo J.C., 2002, Mercury distribution in water, sediment and soil in the Idrijca and Soca river systems. Geochemistry: Exploration, Environment, Analysis, 2, 287-296.

Johnson D.W., Benesch J.A., Gustin M.S., Schorran D.S., Lindberg S.E., Coleman J.S., 2003, Experimental evidence against diffusion control of Hg evasion from soils. Science of The Total Environment, 304, 175-184.

Kocman D., Horvat M., 2011, Non-point source mercury emission from the Idrija Hg-mine region: GIS mercury emission model. *Journal of Environmental Management*, 92, 2038-2046.

Kocman D., Vreča P., Fajon V., Horvat M., 2011, Atmospheric distribution and deposition of mercury in the Idrija Hg mine region, Slovenia. Environmental Research, 111, 1-9.

Lacerda L.D., De Souza M., Ribeiro M.G., 2004, The effects of land use change on mercury distribution in soils of Alta Floresta, Southern Amazon. Environmental Pollution, 129, 247-255.

Langenscheidt A., 2006, La minería de la Sierra Gorda de Querétaro. Arqueología Mexicana, 13, 77.

Li P., Feng X., Shang L., Qiu G., Meng B., Liang P., Zhang H., 2008, Mercury pollution from artisanal mercury mining in Tongren, Guizhou, China. Applied Geochemistry, 23, 2055–2064.

Lin Y., Larssen T., Vogt R.D., Feng X., 2010, Identification of fractions of mercury in water, soil and sediment from a typical Hg mining area in Wanshan, Guizhou province, China. Applied Geochemistry, 25, 60-68.

Mason R.P., Sheu G-R., 2002, Role of the ocean in the global mercury cycle. Global Biogeochemical Cycles, 16, 41093.

Mason R.P., Kim E-H., Cornwell J., Heyes D., 2005, An examination of the factors influencing the flux of mercury, methylmercury and other constituents from estuarine sediment. Marine Chemistry, 102, 96-110.

Molina J.A., Oyarzun R., Esbrí J.M., Higueras P., 2006, Mercury accumulation in soils and plants in the Almadén mining district Spain: one of the most contaminated sites on Earth. Environmental Geochemistry and Health, 28, 487–498.

Navarro A., Cardellach E., Corbella M., 2009, Mercury mobility in mine waste from Hg-mining areas in Almería, Andalusia (SE Spain). *Journal of Geochemical Exploration*, 101, 236-246.

NOM-127-SSA1, 1994, Modificación a la Norma Oficial Mexicana. Salud ambiental. Agua para uso y consumo humano. Límites permisibles de calidad y tratamientos a que debe someterse el agua para su potabilización. Diario Oficial de la Federación. México, D.F.

NOM-147-SEMARNAT/SSA1, 2004, Proyecto de Norma Oficial Mexicana. Establece criterios para determinar las concentraciones de remediación de suelos contaminados por arsénico, berilio, cadmio, cromo hexavalente, mercurio, niquel, plomo, selenio, talio y vanadio. Diario Oficial de la Federación. México, D.F.

Parsons M.B., Percival J.B., 2005, A brief history of mercury and its environmental impact. In: Mercury: sources, measurements, cycles and effects, Parsons M.B., Percival J.B. (Eds.). Mineralogical Association of Canada. Halifax, Nova Scotia.

Patra M., Sharma A., 2000, Mercury toxicity in plants. The Botanical Review, 66, 379–422.

Pyatt F.B., Pyatt A.J., Walter C., Sheen T., Grattan J.P., 2005, The heavy metal of skeletons from an ancient metalliferous polluted area in southern Jordan with particular reference to bioaccumulation and human health. Ecotoxicology and Environmental Safety, 60, 295-300.

Qiu G., Feng X.B., Wang S.F., Shang L.H., 2005, Mercury and methylmercury in riparian soil, sediments, mine-waste calcines, and moss from abandoned Hg mines in east Guizhou province, southwestern China. Applied Geochemistry, 20, 627-638.

Qiu G., Feng X., Wang S., Shang L., 2006, Environmental contamination of mercury from

Hg-mining areas in Wuchuan northeastern Guizhou, China. Environmental Pollution, 142, 549–558.

Rea A.W., Lindberg S.E., Scherbatskoy T., Keeler G.J., 2004, Mercury accumulation in foliage over time in two Northern mixed-hardwood forests. Water, Air, and Soil Pollution, 133, 49–67.

Rothenberg S.E., Du X., Zhu Y-G., Jay A., 2007, The impact of sewage irrigation on the uptake of mercury in corn plants (Zea mays) from suburban Beijing. Environmental Pollution, 149, 246-51.

Rytuba J.J., 2000, Mercury mine drainage and processes that control its environmental impact. Science of The Total Environment, 260, 57-71.

Schroeder W., Munthe J., 1998, Atmospheric Mercury – an overview. Atmospheric Environmental, 32, 809-822.

Selin N.E., 2009, Global biogeochemical cycling of mercury: a review. Annual Review of Environment Resources, 34, 43–63.

Sierra M.J., Millán R., Esteban E., 2009, Mercury uptake and distribution in Lavandula stoechas plants grown in soil from Almadén mining district (Spain). Food and Chemical Toxicology, 47, 2761–2767.

Stamenkovic J., Gustin M.S., 2009, Nonstomatal and stomatal uptake of atmospheric mercury. Environmental Science and Technology, 43, 1367–1372.

Temmerman L., Waegeneers N., Claeys N., Roekens E., 2009, Comparison of concentrations of mercury in ambient air to its accumulation by leafy vegetables: An important step in terrestrial food chain analysis. Environmental Pollution, 157, 1337-1341.

UNEP, 2002, Report of the Global Mercury Assessment Working Group on the Work of its First Meeting, Geneva, Switzerland, 9-13 September 2002.

Wang S., Feng X., Qiu G., Fu X., Wei Z., 2007, Characteristics of mercury exchange flux between soil and air in the heavily air-polluted area, eastern Guizhou, China. Atmospheric Environment, 41, 5584–5594.

Wasserman J.C., Hacon S., Wasserman M.A., 2003, Biogeochemistry of mercury in the Amazonian environment. Ambio: A Journal of the Human Environment, 32, 5, 336-342.

WHO-IPCS, 2004, WHO Food Additives Series: 52. Safety evaluation of certain food additives and contaminants. World Health Organization, Geneva, Switzerland.

Geofísica Internacional (2013) 52-1: 59-72

Original paper

Study of Seismic Clusters at Bahía de Banderas Region, Mexico

Marta Rutz López, Francisco J. Núñez Cornú* and Carlos Suárez Plascencia

Received: May 03, 2012; accepted: November 26, 2012; published on line: December 14, 2012

Resumen

La costa de Jalisco y el sur de Nayarit es una región con un fuerte desarrollo turístico donde el incremento en la población es grande y se encuentran en una zona de alto potencial sísmico. Esto motivó a las autoridades de Protección Civil de Jalisco y la Universidad de Guadalajara a iniciar en el año 2000 estudios para evaluar el riesgo sísmico en la región. Este trabajo se enfocó en el estudio de la sismicidad en el área de Bahía de Banderas y la costa norte de Jalisco, área considerada un Gap Sísmico. Se realizó un análisis de los sismogramas disponibles para identificar estructuras corticales activas, su relación con la morfología superficial y la posible prolongación de estas estructuras a la parte somera de la bahía. Los datos utilizados en el presente trabajo son los registrados en el año 2003 cuando se desplegó una red sísmica en la región. El método está basado en la identificación de acumulaciones sísmicas o familias usando correlación-cruzada de los sismogramas, relocalización de sismos y modelado de planos de falla. A partir de un conjunto inicial de 404 sismos localizados, se seleccionaron 96 sismos con $M_L < 3.6$ que están relacionados con 17 estructuras continentales potencialmente activas. Se obtuvo un modelo del plano de falla para 11 estructuras. Un subgrupo de 7 estructuras se encuentra alineado paralelamente a la trinchera mesoamericana, lo cual puede ser una consecuencia de un proceso de subducción oblicuo. Los focos de los sismos se agruparon en acumulaciones sísmicas que se pueden correlacionar con fallas con dimensiones de cientos de metros, éstas pueden ser consideradas como asperezas o barreras en estructuras tectónicas con longitudes entre 10 y 30 km. Estas estructuras pueden generar terremotos someros con magnitudes entre 5.0 y 6.0, y representan una amenaza sísmica adicional en la región.

Palabras clave: Gap sísmico, placa de Rivera, bloque de Jalisco, Bahía de Banderas, familias sísmicas, correlación-cruzada.

Abstract

The coast in the state of Jalisco and south of Nayarit is located within a region of high seismic potential, increasing population, and tourism development. This motivated Civil Defense authorities of Jalisco and the Universidad de Guadalajara to launch in the year 2000 the assessment of the seismic risk of the region. This work focuses in the seismicity study of the area of Bahía de Banderas and northern coast of Jalisco, which is actually a seismic gap. We perform an analysis of available seismograms to characterize active crustal structures, their relationship to surface morphology, and possible extent of these structures into the bay shallow parts. The data consist of waveforms recorded during 2003 when the seismograph network spanned the region. Our method is based on the identification of seismic clusters or families using cross-correlation of waveforms, earthquake relocation and modeling of fault planes. From an initial data set of 404 located earthquakes, 96 earthquakes with $M_L < 3.6$ are related to 17 potentially active continental structures. We present fault plane model for 11 structures. A subgroup of 7 structures is aligned parallel to the Middle America Trench, as a possible consequence of oblique subduction. The foci of the earthquakes were grouped into clusters corresponding to fault dimensions of hundred of meters, may be considered as asperities or barriers in tectonic structures with lengths between 10 and 30 km. These structures could generate shallow earthquakes with magnitudes between 5.0 and 6.0 and represent an additional seismic threat to the region.

Key words: seismic gap, Rivera plate, Jalisco block, Bahía de Banderas, seismic clusters, cross-correlation.

M. Rutz López
F.J. Núñez Cornú*
C. Suárez Plascencia
Centro de Sismología y Volcanología de Occidente
Universidad de Guadalajara
Av. Universidad 203, Del. Ixtapa
Puerto Vallarta, Jalisco, México
*Corresponding author: pacornu77@gmail.com

Introduction

Bahía de Banderas is located in the Jalisco Block (JB) (Figure 1). This region undergoes different deformation stages from the Mezosoic to the present, producing several active linear structures due to its proximity to a triple junction. The seismic activity recorded by temporary and permanent seismic networks, as well as the structures observed in the continental crust are manifestations of the tectonic deformation that accommodates the JB.

The 1932 (M=8.2) earthquake, the largest event in Mexico during the twentieth century occurred in the JB was followed 15 days later by another large event (M=7.8). Singh *et al.* (1985) studied these events and concluded that the surface expression of the composite rupture area extends across the entire coast of the states of Jalisco and Colima. They suggested a recurrence time of 77 years for the occurrence of a major earthquakes in this region. In 1995 a Mw=8.0 earthquake near Manzanillo involved the central part of the 1932 rupture area, leaving undisturbed patches to the north and south, which are now termed the Vallarta and Colima gaps, respectively (Figure 2).

In addition to the large subduction earthquakes (M>7.6), the complexity of the region of the coast in the state of Jalisco and south of Nayarit is reflected in the existence of poorly known tectonic structures where earthquakes of moderate magnitude occur (7.0<M<7.6); for example the December 3, 1948 event occurred near the Marías Islands (Figure 2). More recently, on 14 September 2010 a thrust fault earthquake (M=6.0) followed by 25 aftershocks in 24 hours with M_L>4.0, recorded by a local seismic network, took place to the south of Marías Islands. Of particular interest is the Mw=7.4 earthquake of 22 January 2003; a shallow earthquake off the state of Colima, México, near the town of Armería. Both, the damage pattern and the surface effects of this earthquake in the neighboring states of Colima and Jalisco were stronger than those caused by recent large earthquakes in these regions and affected different areas; especially in Colima City and Zapotitlan de Vadillo, Jalisco, on the western flank of Colima volcano. An analysis of its aftershocks (Núñez-Cornú *et al*. 2004, 2010) indicates that the earthquake was caused by a continental intraplate reverse fault. These earthquakes may be related to the possible oblique subduction of the Rivera Plate.

The microseismicity at the north of Jalisco and south of Nayarit coasts was studied during the CORTES96 project (Dañobeitia *et al.*, 1997); a joint project between the Universidad de Guadalajara (UG) and the Centro de Investigación Científica y Educación Superior de Ensenada (CICESE) was carried out during 1996-1998 aimed to study the microseismicity occurring north of the JB. Based on the analysis of these results and historical data the spatial distribution of earthquakes, Núñez-Cornú *et al.*, 2002 suggested the existence of various seismogenic zones. Thus, the purpose of this work was to

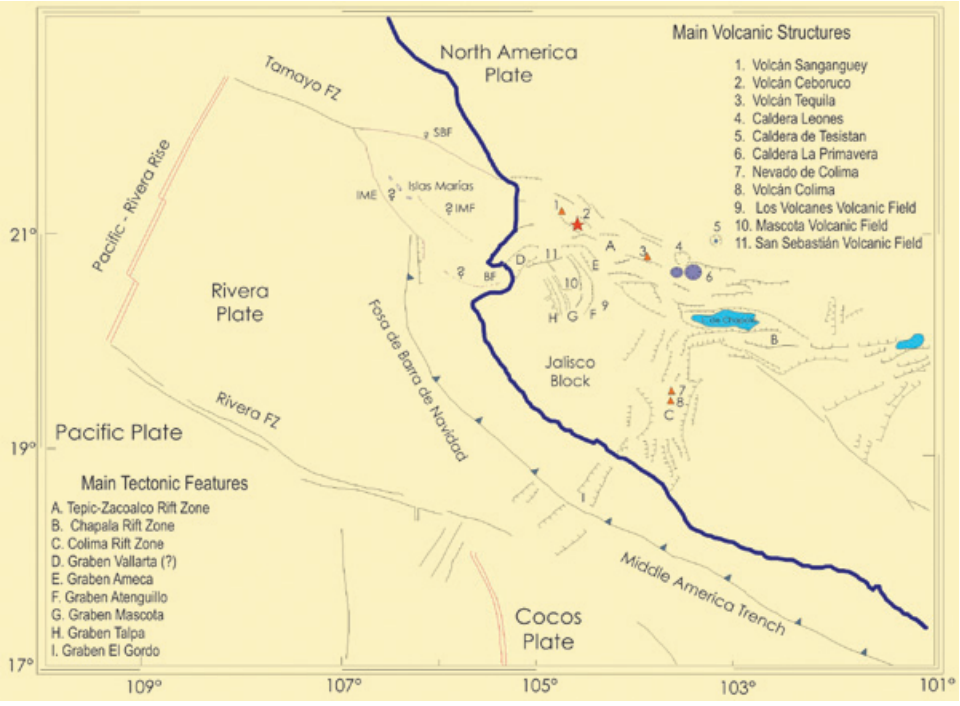

Figure 1. Tectonic frame of Jalisco Block region: SBF, San Blas Fault; IME, Islas Marias Escarpment; IMF, Islas Marías Fault; BF, Banderas Fault (Bahía de Banderas). (Modified from Núñez-Cornú *et al.* (2002).

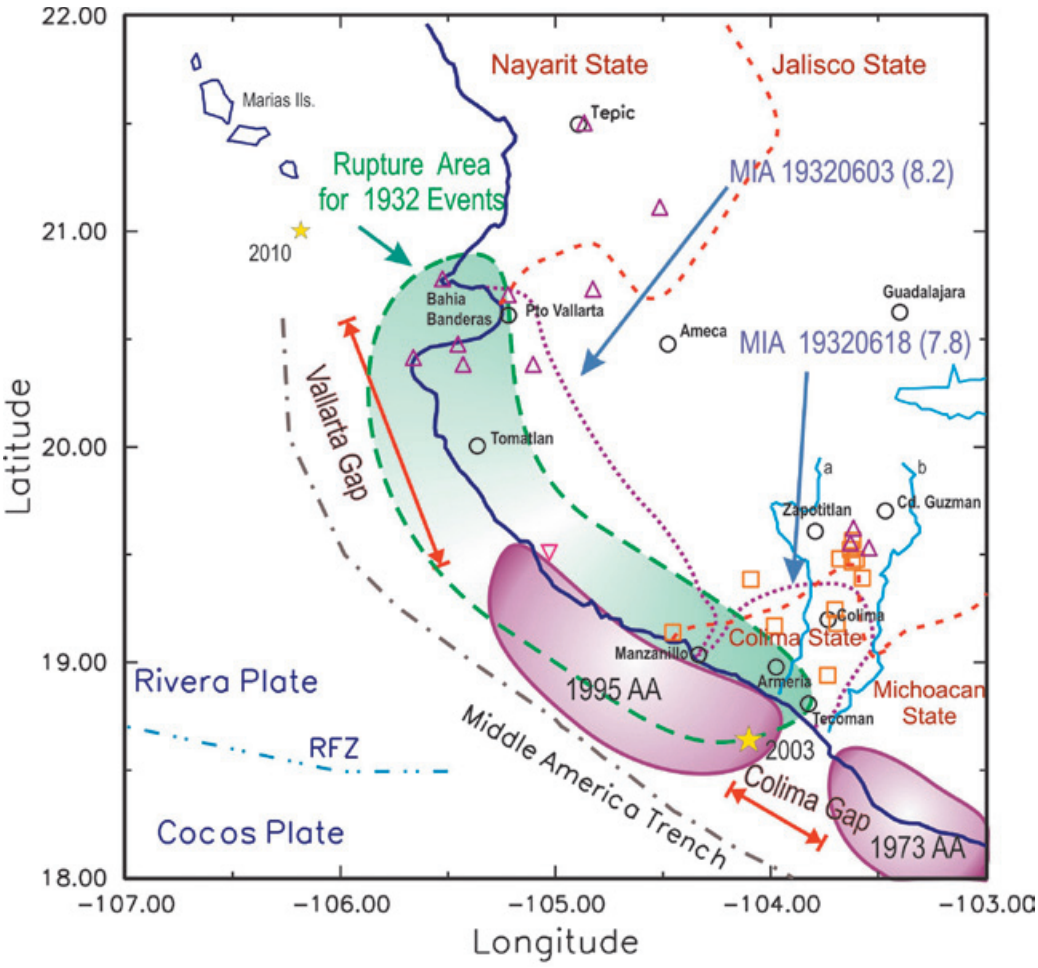

Figure 2. Seismotectonic features of the Jalisco region. RFZ: Rivera Fault Zone; a: Armería River; b: Cohuayana River; MIA: Maximum Intensity Areas for earthquakes in 1932 (dates and magnitudes indicated); AA: Aftershocks Areas. □ Seismograph station (RESCO network), △ (RESJAL network), ▽ CJIG, SSN network; ○ Cities; ☆ 2003 Epicenter of the Armería earthquake (after Núñez-Cornú *et al*., 2004); ☆ 2010 Islas Marías earthquake.

obtain a more detailed knowledge of the regional seismicity and active structures in the northern coast of Jalisco. For this purpose we used data from the Red Sismológica de Jalisco (RESJAL) deployed by Unidad Estatal de Protección Civil Jalisco (PCJal) and the Centro de Sismología y Volcanología de Occidente UG, composed of ten seismograph stations, six telemetric and four autonomous, distributed between the states of Jalisco and Nayarit (Figure 2) comprising sites on Colima and Ceboruco volcanoes. In some cases data from the Red Telemétrica de Colima (RESCO) was used.

Tectonic Setting

According to Núñez-Cornú *et al.* (2002) and others authors the North America, Pacific, Cocos, and Rivera lithospheric plates interact in the western Mexican Volcanic Belt. Several triple point locations have been proposed (Figure 1), however the seismotectonic processes still are not fully known. The existence of a tectonic unit in this region, known as the JB, has been proposed by several researchers (Luhr *et al*., 1985; Bourgois *et al*., 1988; Garduño and Tibaldi, 1991; DeMets and Stein, 1990; Allan *et al*., 1991; Ferrari *et al*., 1994; Rosas-Elguera *et al.*, 1996). The JB is limited to the east by the Colima Rift Zone, which extends northward from the Pacific coast and connects at its northern end with two other major extensional structures: the Tepic-Zacoalco Rift Zone (TRZ) (trending roughly NW-SE) defined as the northern boundary of the JB, and the Chapala Rift Zone (trending roughly E-W). The connection between the northwestern border of the JB and the continent (the Tamayo Fault System) is not well defined. This border has been related to the San Blas Fault as continuation of the TRZ, or to the Islas Marías

Escarpment [west of Tres Marías Is.] and the Banderas Fault (BF), which crosses the Bahía de Banderas and continues through the Vallarta Graben (VG) to join the TRZ (Figure 1) another possible connection to the Tres Marías Fault. The last two possibilities suggest the existence of a small block [the Tres Marías Block (?)]. Álvarez (2007) suggest that the BF and the VG are part of the same tectonic structure, and is part of the NW limit of JB. The Bahía de Banderas area may be undergoing strong crustal stresses as a convergence of the Rivera Plate (Kostoglodov and Bandy, 1995). The existence of shallow submarine hydrothermal activity in the Bahía de Banderas (Núñez-Cornú *et al.*, 2000) could be a result of these stresses.

Data

The RESJAL stations were deployed between late 2001 and 2002. The stations deployed in the study area revealed that the regions of Bahía de Banderas-Valle de Tomatlán and Ameca, formerly thought as regions of scarce seismicity, exhibit high seismic activity. A seismicity consisting of small magnitude events was observed in the Bahía de Banderas area, and of larger magnitudes in the southern coast of Jalisco and the region of Ameca (Figure 2). By 2003 a total of 404 earthquakes with local magnitudes between 0 and 5.0 were detected and located within an area bounded by the coordinates 20°N-21°N and 104°W-106°W (Figure 3). We focused the study in those areas. By 2004 telemetric stations deployed at north of Jalisco and Bahía de Banderas stop operation.

Stations BSSJ and MCUJ (Figure 3) were not operational during the last trimester of 2003 while stations YELJ and CORJ operated intermittently. During that time 400 low-magnitude earthquakes occurred in various swarms. This activity was recorded by station AGUJ and partially by YELJ; the events showed S-P times usually less than 10 s., we observed that north of parallel 21°N the seismicity was scarce.

During a preliminary revision of the data, we observed the occurrence of many earthquakes of similar waveforms. This observation was already noted during a preliminary study in 1998 (Núñez-Cornú *et al*., 2002) when on some days swarms of 20 to 30 similar waveform earthquakes were detected, mostly by the AGUJ station (Figure 3). With the deployment of additional stations the coverage improved and many of this type of earthquakes could be located. However, the earthquakes of small magnitude and were recorded by only one or two stations, locations were estimated using 3 component analysis. In the present study we relocated the earthquake foci using a method based on cross-correlation of seismic phases. This methodology improves the study of the seismic activity.

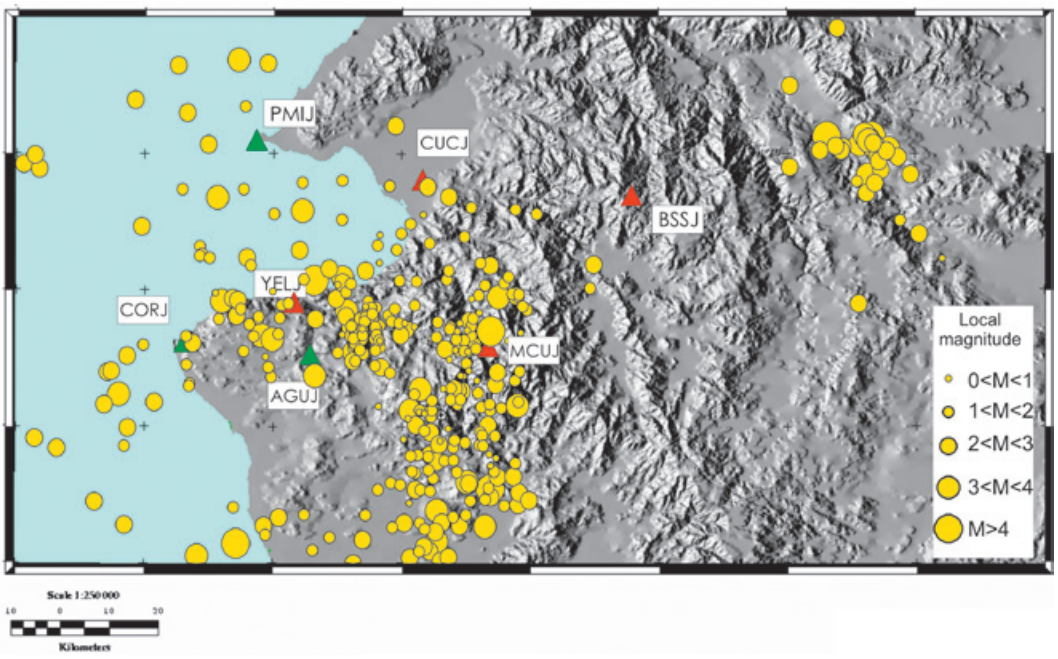

Figure 3. Seismicity in the Bahía de Banderas region in 2003, includes earthquake located with one or two stations. Red triangle: Telemetric stations; green triangle: Autonomous stations.

Correlation method

The methodology used was developed by Deichmann and García-Fernández (1992), improved by Maurer and Deichmann (1995) and applied to seismic swarms recorded by a regional network in northern Switzerland. When two earthquakes have similar waveforms we assume that the source and the propagation media are the same. If the source of a particular waveform can be determined, earthquakes with that same waveform can be located even if they are recorded by only a few stations. The sources are not considered as point sources, but rather faults with finite dimensions that can include asperities or barriers where the earthquake originates.

The cross-correlation and relocation method has been applied to other swarms data set in different locations, e.g. in Spain the 1993-1994 swarm in Almería (Stich *et al.*, 2001), the 1988-1989 swarm in Granada (Saccorotti *et al*., 2002), and the 2005 swarm in Murcia (Ocaña, 2006).

The method is applied as follows: 1) Use initially the earthquakes recorded by three or more stations; 2) Correlate all seismograms in the time domain for a particular seismic station; 3) Group by seismic families those waveforms with large correlation values; 4) Choose the best located epicenter, which will be the master event for each family; 5) Relocate all earthquakes in a group as a function of the master event; 6) Estimate the plausible fault plane with the hypocenters located in each group; 7) Compute the focal mechanism of the Master Event based on the polarity of the first P-arrivals of all records.

We applied the cross-correlation algorithm (Saccorotti *et al.*, 2002) to estimate the degree of similarity pairs of earthquakes recorded initially at stations MCUJ and AGUJ to identify the families, in some cases other stations were also used when good quality data was available. To homogenize the differences on the waveforms among located earthquakes we filtered each seismogram with a 1-15 Hz band-pass filter. We used the direct **P** and **S** phases in our analysis. To find similarities in **P** waves, we chose the vertical component and for **S** waves the N-S component since most of the arrival times of the **S** phases were determined using that component. For completeness, we also tried the program using data in the E-W component and obtained similar results. We defined a time window of 2 s starting 0.4 s before the **P**-arrival. In the case of **S**-waves, the time window was of 3 s starting 0.5 s before its arrival. The waveforms analyzed had S-P times that varied between 2 and 10 s.

The criteria to group earthquakes into certain families are as follows: 1) Correlation threshold for **P** phase; 2) Correlation threshold for **S** phase; 3) Those earthquake pairs within thresholds 1 and 2 are analyzed again and compared with respect to the other earthquakes and a correlation threshold value is set between rows with **P** and **S** phases. For the earthquakes used in this study we used the following threshold values: **P**-threshold = 0.8, **S**-threshold = 0.8, and **S*P** threshold = 0.7.

From the total 404 earthquakes initially located by Rutz-López (2007) using the Hypocenter code (Lienert *et al*., 1986), 96 were classified into 17 families; each family composed of 3 to 12 earthquakes. Figure 4 shows the waveforms for the vertical components of four representative families recorded at station MCUJ. The hypocenters of the 17 families are shown in Figure 5 (a to c). Seismograms from the MCUJ station were used to characterize and classify14 of the families, while the other three families were characterized using AGUJ station seismograms; although earthquakes were recorded at both stations, we used data from the station nearest to each family. Figure 5d shows the occurrence times of the earthquakes from the different families; although the data may not be representative of long-term behavior, since they span only one year, it shows that the activity of some families, e.g. M09, M17, M18, and M19, lasted one day only, whereas other families had longer periods of activity.

In order to have a very similar appearance at one or more stations, the earthquakes of a given family must have similar rupture mechanisms and similar paths to each station, which means that their hypocenters should cluster together. It can be seen in Figure 5 that the hypocenters determined by the initial location do not present the expected clustering, which indicates the need for relative relocation of the earthquakes in each family.

According to Wells and Coppersmith (1994) the subsurface rupture length for a magnitude 4.0 earthquake (Table 1) is 550 m which agrees with the hypothesis of same source, so relative relocation of the earthquakes of each family is necessary.

Correlating the Master Event with its family members

Three of the 17 families (A16, M08, and M16) were discarded from the analysis because we cannot adjust the arrival times in the waveforms. In Figures 6 and 7 we show the waveforms of four well-defined families (M07, M09, M14 and M15). Here the correlation program adjusted the arrival times for each earthquake in the families. We also show the correlation values obtained for each station.

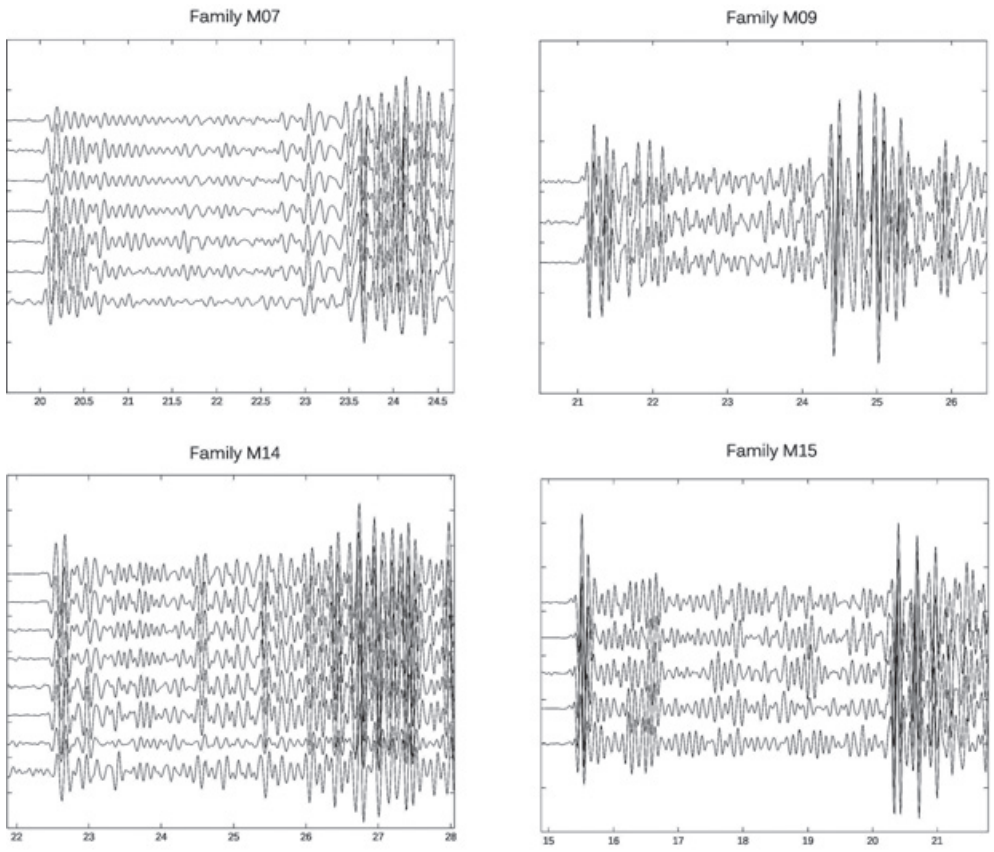

Figure 4. Waveforms showing P and S waves of four seismic families identified in the Bahía Banderas region.

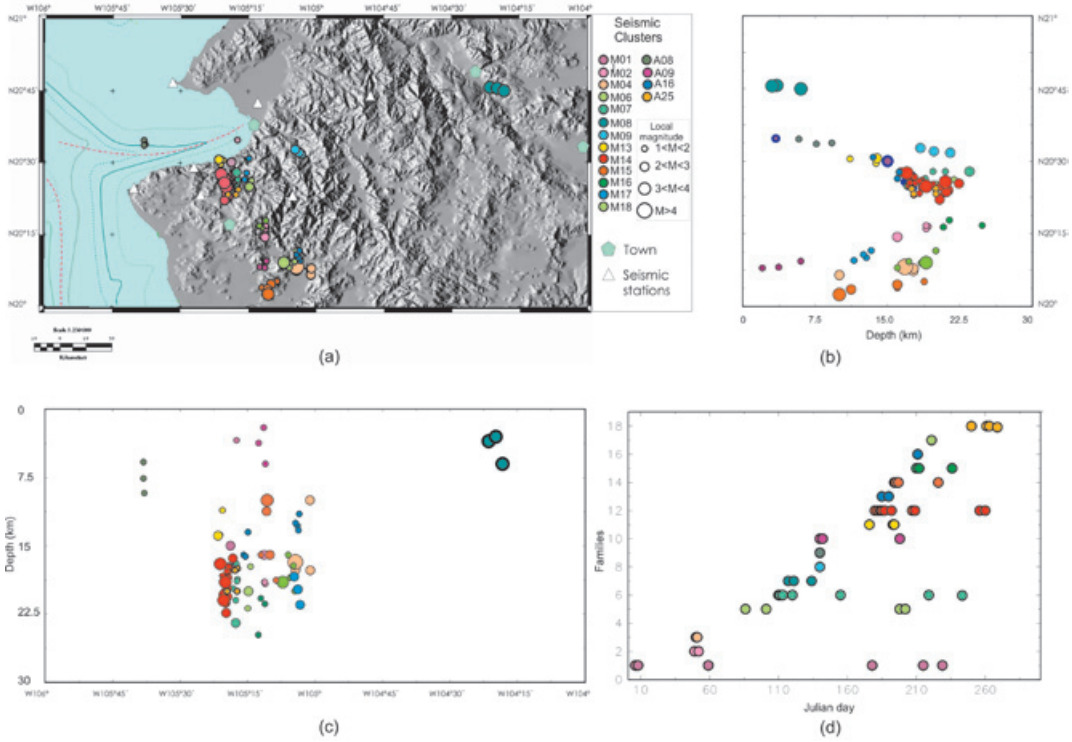

Figure 5. Seismic families identified in this work. A) Epicenters. B) Profile North-South. C) Profile East-West. D) Chronological order of occurrence, Y-axis: Number of family, X-axis: day of year.

Table 1. Hypocenter data for master event in each family; relative relocation for the earthquakes in each family; Adjusted fault plane data for each family.

M01	Date	hour	Sec	Lat	Long	Depth	mag	n lec	rms	erh	erz
Master Ev	30627	20:45	2.34	20.4135	-105.3105	19.72	1.2	8	0.12	1.5	1.5
Relocated	date	hour	x(km)	dx	y(km)	dy	z(km)	dz			
1	30228	02:45	0.31	0.064	1.434	0.227	-0.246	0.047			
2	30803	19:39	0	0.064	-0.027	0.227	0.036	0.047			
3	30817	07:28	0.375	0.064	0.083	0.227	-0.24	0.047			
4	30817	16:16	0.379	0.064	0.184	0.28	-0.194	0.059			
	Azi(°)	Dip(°)	rms	NEq							
Plane	175.3	58.5	0.015	5							

M02	Date	hour	Sec	Lat	Long	Depth	mag	n lec	rms	erh	erz
Master Ev	30218	03:51	10.36	20.2575	-105.1947	20.55	1.7	8	0.07	0.9	0.6
Relocated	date	hour	x(km)	dx	y(km)	dy	z(km)	dz			
1	30218	356	0.790	0.031	1.804	0.088	-1.914	0.067			
2	30218	414	-0.013	0.031	0.008	0.088	-0.036	0.067			
3	30218	542	-0.104	0.031	0.296	0.088	-0.415	0.067			
4	30221	1923	-0.327	0.025	-3.005	0.069	3.532	0.059			
	Azi(°)	Dip(°)	rms	NEq							
Plane	97.9	40.9	0.035	5							

M06	Date	hour	Sec	Lat	Long	Depth	mag	n lec	rms	erh	erz
Master Ev	30721	14:52	14.93	20.1312	-105.0823	17.32	3.5	8	0.35	4	2.8
Relocated	date	hour	x(km)	dx	y(km)	dy	z(km)	dz			
1	30717	535	0.071	0.133	0.18	0.517	-0.285	0.882			
2	30717	814	0.109	0.133	0.571	0.517	-0.924	0.882			
	Azi(°)	Dip(°)	rms	NEq							
Plane	16.4	3.5	0.000	4							

M07	Date	hour	Sec	Lat	Long	Depth	mag	n lec	rms	erh	erz
Master Ev	30604	15:57	38.97	20.4568	-105.3047	22.91	1.8	10	0.41	3.6	3.7
Relocated	date	hour	x(km)	dx	y(km)	dy	z(km)	dz			
1	30420	58	-0.079	0.08	-0.166	0.272	-0.038	0.063			
2	30421	340	-0.048	0.08	-0.097	0.272	-0.041	0.063			
3	30430	310	0.13	0.06	0.337	0.211	0.034	0.057			
4	30807	1651	-0.039	0.06	-0.045	0.211	-0.061	0.057			
5	30825	2156	-0.276	0.08	-0.314	0.272	-0.23	0.063			
	Azi(°)	Dip(°)	rms	NEq							
Plane	6.9	48.0	0.012	6							

M09	Date	hour	Sec	Lat	Long	Depth	mag	n lec	rms	erh	erz
Master Ev	30520	09:27	30.58	20.5418	-105.0828	18.64	2.6	20	0.25	0.8	0.6
Relocated	date	hour	x(km)	dx	y(km)	dy	z(km)	dz			
1	30520	706	-0.007	0.039	0.078	0.043	0.032	0.034			
2	30520	707	-0.013	0.082	-0.022	0.054	0.019	0.064			
	Azi(°)	Dip(°)	rms	NEq							
Plane	7.4	27.9	0.000	3							

Table 1. (Cont.)

M14	Date	hour	Sec	Lat	Long	Depth	mag	n lec	rms	erh	erz
Master Ev	30711	02:53	16.73	20.4527	-105.349	17.62	3.7	40	0.46	1	0.8
Relocated	date	hour	x(km)	dx	y(km)	dy	z(km)	dz			
1	30629	626	0.049	0.031	0.043	0.077	-0.007	0.041			
2	30629	627	0.029	0.038	0.025	0.105	0.013	0.058			
3	30629	729	0.01	0.054	0.018	0.167	0.009	0.046			
4	30701	1844	0.027	0.068	0.058	0.219	0.001	0.047			
5	30703	1436	-0.004	0.068	-0.032	0.219	0.053	0.047			
6	30704	659	0.106	0.054	0.142	0.167	0.08	0.046			
7	30706	1831	-0.032	0.068	-0.076	0.219	-0.001	0.047			
8	30726	200	-0.031	0.068	0.043	0.219	0.113	0.047			
9	30728	2303	0.096	0.054	0.092	0.167	0.092	0.046			
10	30913	643	0.067	0.054	0.016	0.167	-0.037	0.046			
11	30917	1143	0.111	0.054	0.191	0.167	-0.061	0.046			
	Azi(°)	Dip(°)	rms	NEq							
Plane	34.2	8.0	0.022	12							

M15	Date	hour	Sec	Lat	Long	Depth	mag	n lec	rms	erh	erz
Master Ev	30714	11:02	54.47	20.0477	-105.1855	11.37	3.6	32	0.39	1.3	2.6
Relocated	date	hour	x(km)	dx	y(km)	dy	z(km)	dz			
1	30713	33	-0.016	0.048	0.03	0.061	-0.308	0.21			
2	30814	1915	0.021	0.048	0.016	0.061	0.047	0.21			
3	30814	2000	0.06	0.171	0.058	0.537	-0.112	2.239			
	Azi(°)	Dip(°)	rms	NEq							
Plane	54.8	5.6	0.002	4							

M19	Date	hour	Sec	Lat	Long	Depth	mag	n lec	rms	erh	erz
Master Ev	30827	06:27	58.99	20.1898	-105.1888	6.08	2.5	18	0.36	2.5	6.7
Relocated	date	hour	x(km)	dx	y(km)	dy	z(km)	dz			
1	30827	1548	0.022	0.053	0.099	0.061	-0.085	0.182			
2	30827	1855	0.024	0.148	0.200	0.404	-0.962	2.699			
	Azi(°)	Dip(°)	rms	NEq							
Plane	13.7	1.4	0.000	3							

M20	Date	hour	Sec	Lat	Long	Depth	mag	n lec	rms	erh	erz
Master Ev	30520	15:01	38.13	20.1358	-105.1865	11.01	1.6	10	0.28	3.2	7.9
Relocated	date	hour	x(km)	dx	y(km)	dy	z(km)	dz			
1	30520	1506	0.008	0.032	0.049	0.188	0.040	0.270			
2	30520	2235	-0.012	0.032	-0.013	0.188	-0.025	0.270			
	Azi(°)	Dip(°)	rms	NEq							
Plane	158.3	32.5	0.000	3							

A09	Date	hour	Sec	Lat	Long	Depth	mag	n lec	rms	erh	erz
Master Ev	30522	20:05	37.89	20.116	-105.1772	3.49	1.7	10	0.29	7.9	10.8
Relocated	date	hour	x(km)	dx	y(km)	dy	z(km)	dz			
1	30520	1819	-0.088	0.592	0.401	2.75	0.733	4.923			
2	30717	1901	-0.076	0.592	0.83	2.75	1.293	4.923			
	Azi(°)	Dip(°)	rms	NEq							
Plane	32.9	21.7	0.000	3							

A25	Date	hour	Sec	Lat	Long	Depth	mag	n lec	rms	erh	erz
Master Ev	30907	12:39	24.74	20.3832	-105.3033	19.64	1.2	8	0.13	1.9	1.3
Relocated	date	hour	x(km)	dx	y(km)	dy	z(km)	dz			
1	30918	2357	-0.002	0.066	0.030	0.221	-0.010	0.075			
2	30920	643	0.072	0.066	0.223	0.221	-0.061	0.075			
	Azi(°)	Dip(°)	rms	NEq							
Plane	64.6	70.3	0.000	4							

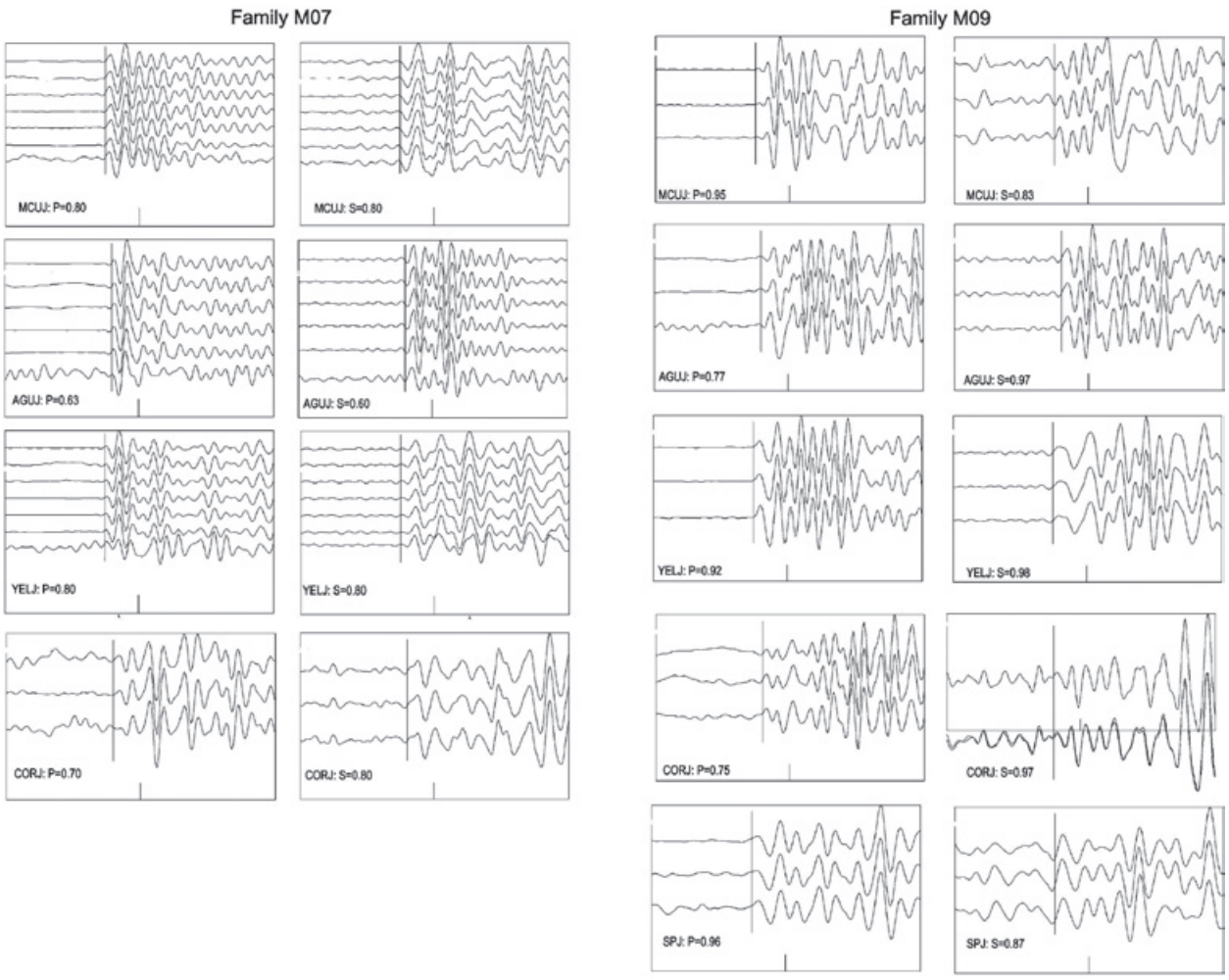

Figure 6. Wave forms (P and S) for Families 07 and 09 (Two seconds windows).

We chose as master event for each family a representative earthquake, which usually had the largest magnitude and the best determined location. The location accuracy of this event is critical because the rest of family members are relocated based on the master's hypocenter.

Family relocation relative to Master Event

With the correlation between master event and its family result we used a linear method (Console and DiGiovambattista, 1987) to find relocated hypocenters of earthquakes relative to the master event. The hypocenter coordinates and the associated errors are given in Table 1. Based in this cluster of dots, we can estimate plausible fault planes near the master event with a least squares method. Only 11 families yielded reliable fault planes. The relocation results, alignments and possible fault planes for families M01, M02, M06, M07, M09, M19, M20, A09 and A25 are shown in Figure 8. For master events of Families M14 and M15 we had an adequate number of polarity data to obtain focal mechanisms; the solutions of these focal mechanisms agree with the fault planes obtained with the least squares method (Figure 9).

Geomorphological analysis

Topographic lineaments greatly reflect the tectonic structures of the bedrock, which are enlarged in the surface by topography, drainage and vegetation (Rahiman and Pettinga, 2008). Therefore an analysis of these features was carried out in the region. Their identification along the Puerto Vallarta inland of the Jalisco north shore was made using a digital terrain model

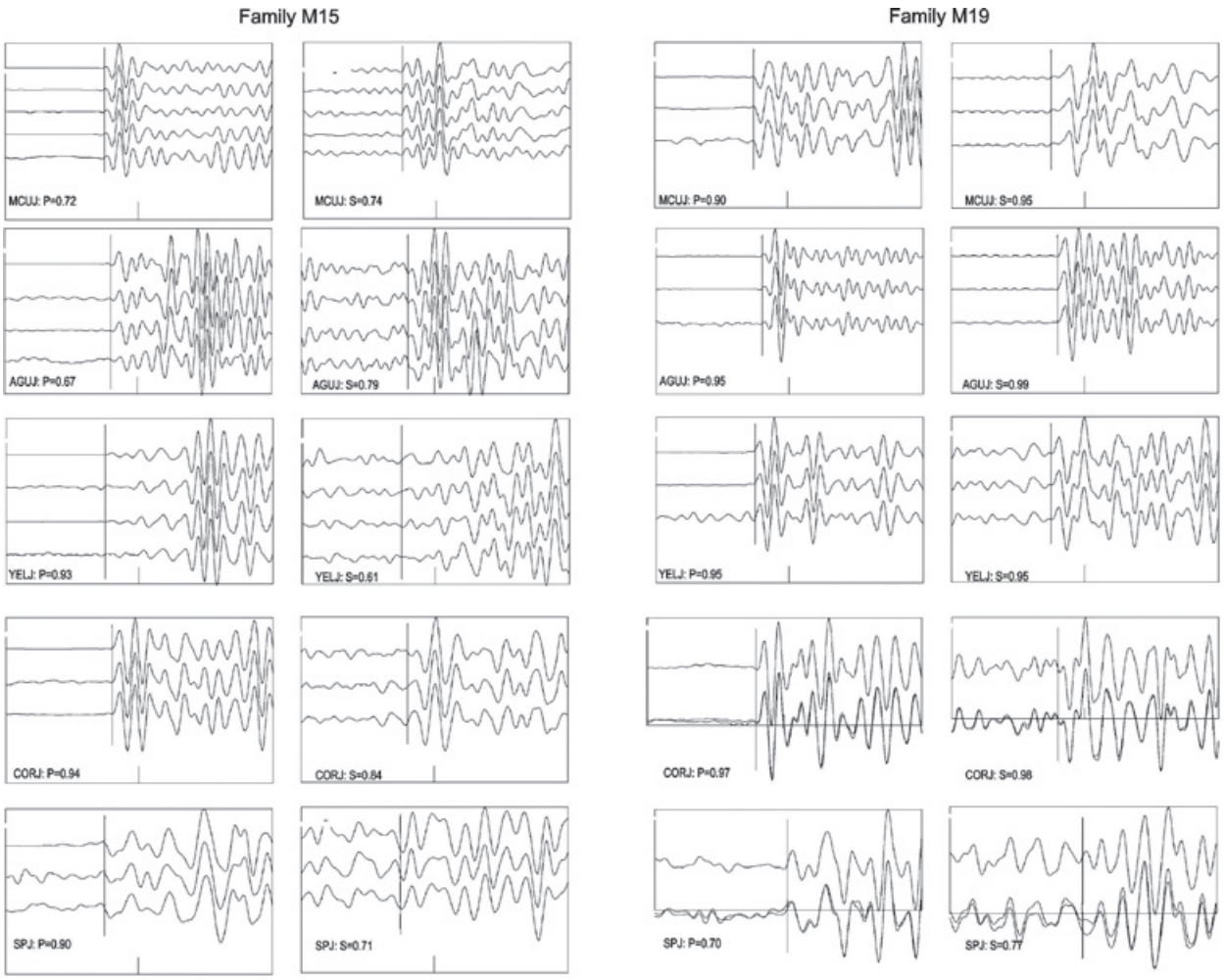

Figure 7. Wave forms (P and S) for Families 14 and 15 (Two seconds windows).

(DTM). The DTM was built based on a vector model with 20 m contour line intervals from the Instituto Nacional de Geografía e Informática and using triangle based interpolation with a 20 m grid in ErMapper ver. 7.1. The results show that the studied region is dissected by a complex lineament system that affects Mesozoic granite stocks, lavas, and Quaternary volcanoclastic sediments.

We identify parallel systems of 20 km long lineaments with preferred orientations N-S, WNW-ESE, and NE-SW. These results indicate a complex deformation fracture system that affects the studied region and could be related to active tectonism in the zone. From bathymetric studies, Álvarez (2007) propose a half-graben structure for the Banderas Canyon (a structure in the Bahía de Banderas), and propose a fault system oriented NE at north and south sectors of the bay, the faults at south of the bay do not agree with our results.

Most of the master events are located on the lineaments and the orientation of the fault planes calculated roughly agree with the direction of the lineaments (Figure 10).

Conclusions

From the available data and the analysis of cross-correlation, we define 17 families of events, which could be associated with sources mechanisms and stationary paths in an area south of Bahía de Banderas. For 14 families we obtain a relative relocation using a master event technique. The largest earthquake recorded at as many stations as possible was chosen as the master event in each family. Relocation of earthquakes in each family reduced the spatial scatter of epicenters to areas with radii less than 1 km. These 14 families have foci within the continental crust, at depths of 10-22 km, except for families M19 and A09 which are located within the upper 10 km of the crust. Using a least squares approach, we

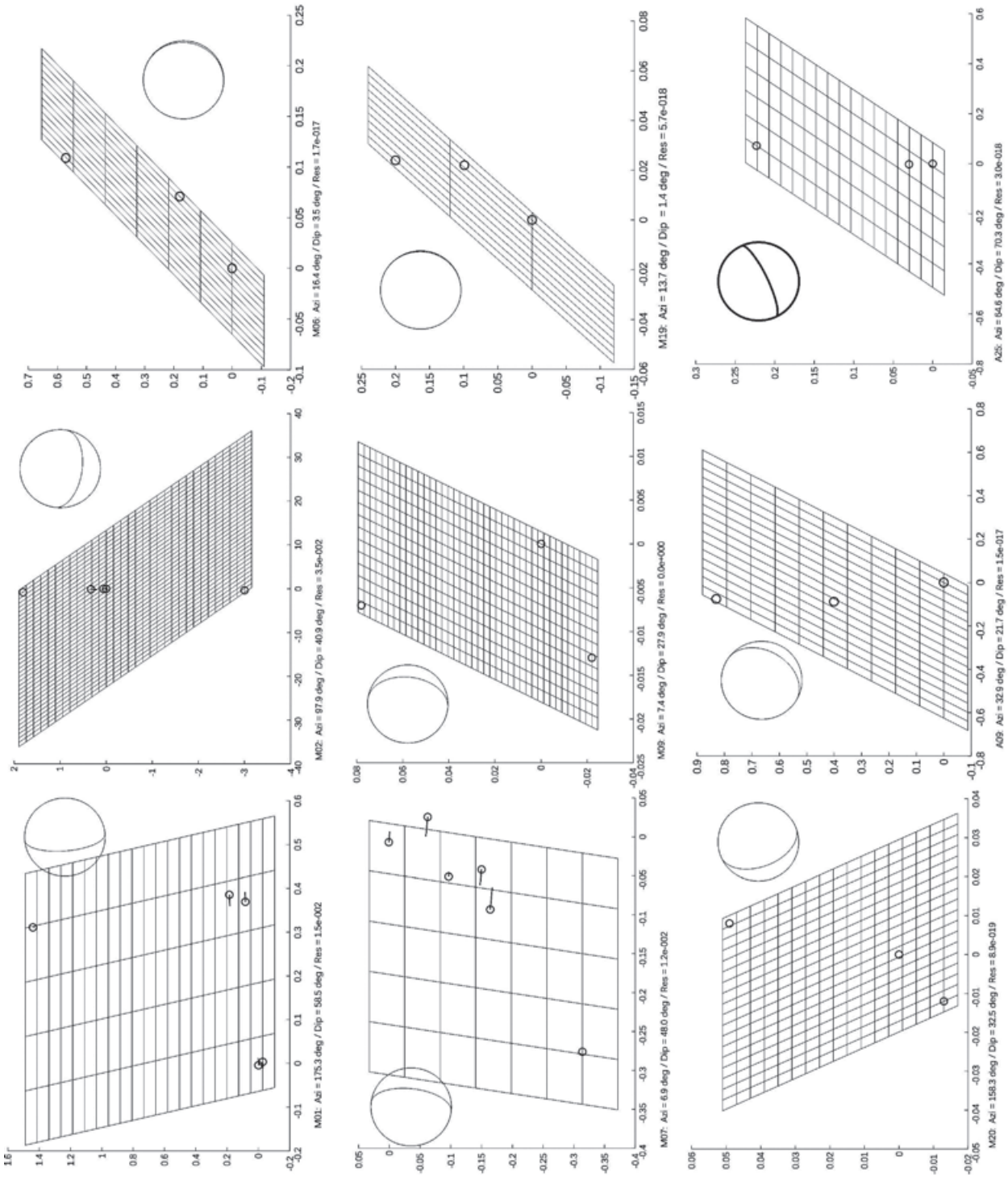

Figure 8. Fault planes for families M01, M02, M06, M07, M09,M19, M20, A25 and A09 obtained adjusting the relocated earthquakes by least squares method; projection of the plane in focal sphere.

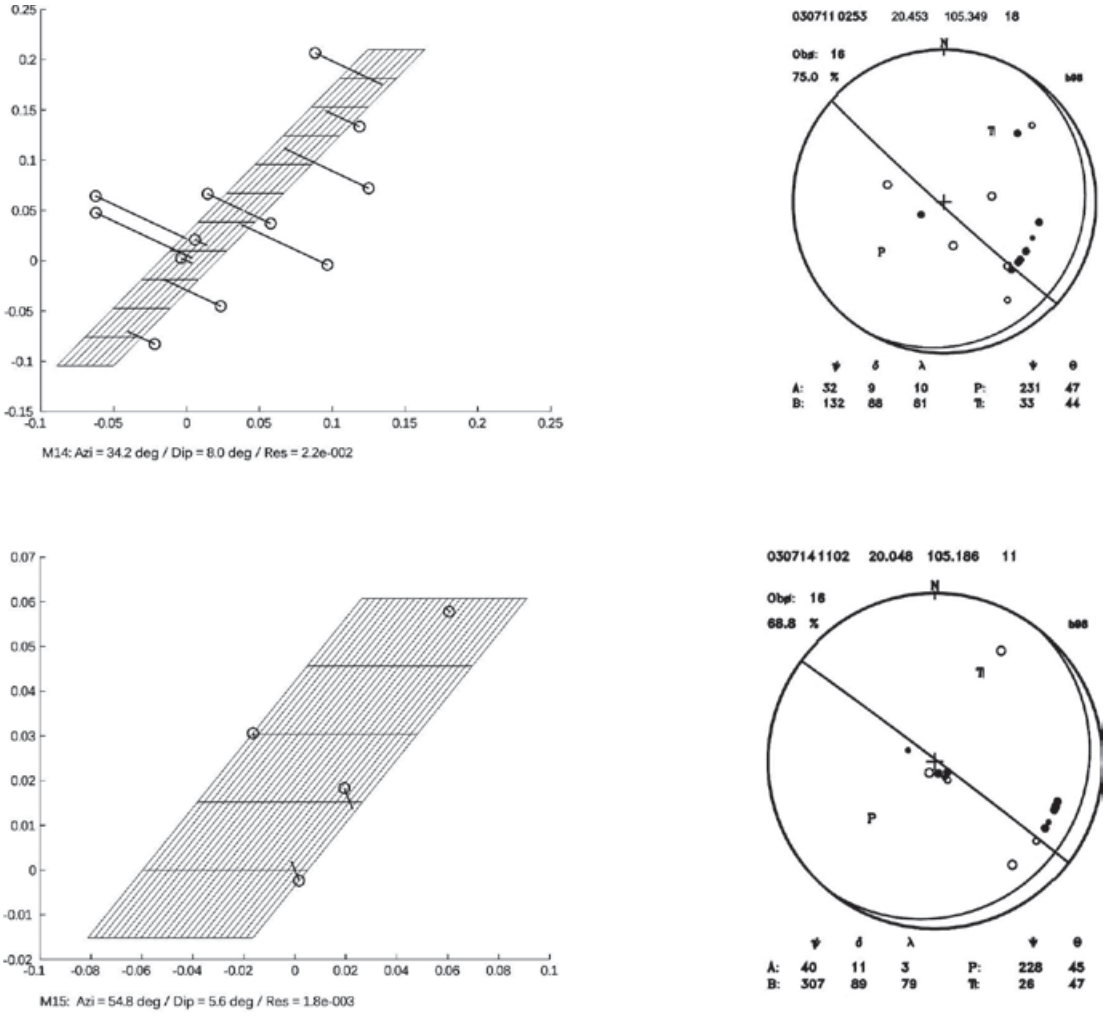

Figure 9. Fault planes obtained for families M14 and M15 and focal mechanism obtained for their master events.

could model fault planes for 11 of the families. Focal mechanisms were determined for two of the master events (M14 and M15) and in both cases they were consistent with modeled planes, which support our results.

This analysis shows the existence of 17 tectonic active sources of which 11 fault planes were identified. The hypocenter of the master event and their fault planes of these sources agree with some of lineaments structures observed in the region. A group of 7 structures are aligned parallel to the Middle America Trench, as a possible consequence of oblique subduction. These sources can be identified as asperities or barriers in active crustal lineament structures, some of them with a length greater than 20 km, that could generate an earthquake with 6.5 magnitude (Wells and Coppersmith, 1994). This represents a high seismic hazard for the region in addition to the threat of the occurrence of an interplate event in the Vallarta gap.

These studies can yield a more complete evaluation of the seismic hazard associated to crustal structures, independently of the subduction process of Rivera plate under JB, in the region of Bahía de Banderas and the northern coast of Jalisco, if the number of seismic stations is increased and operated continuously.

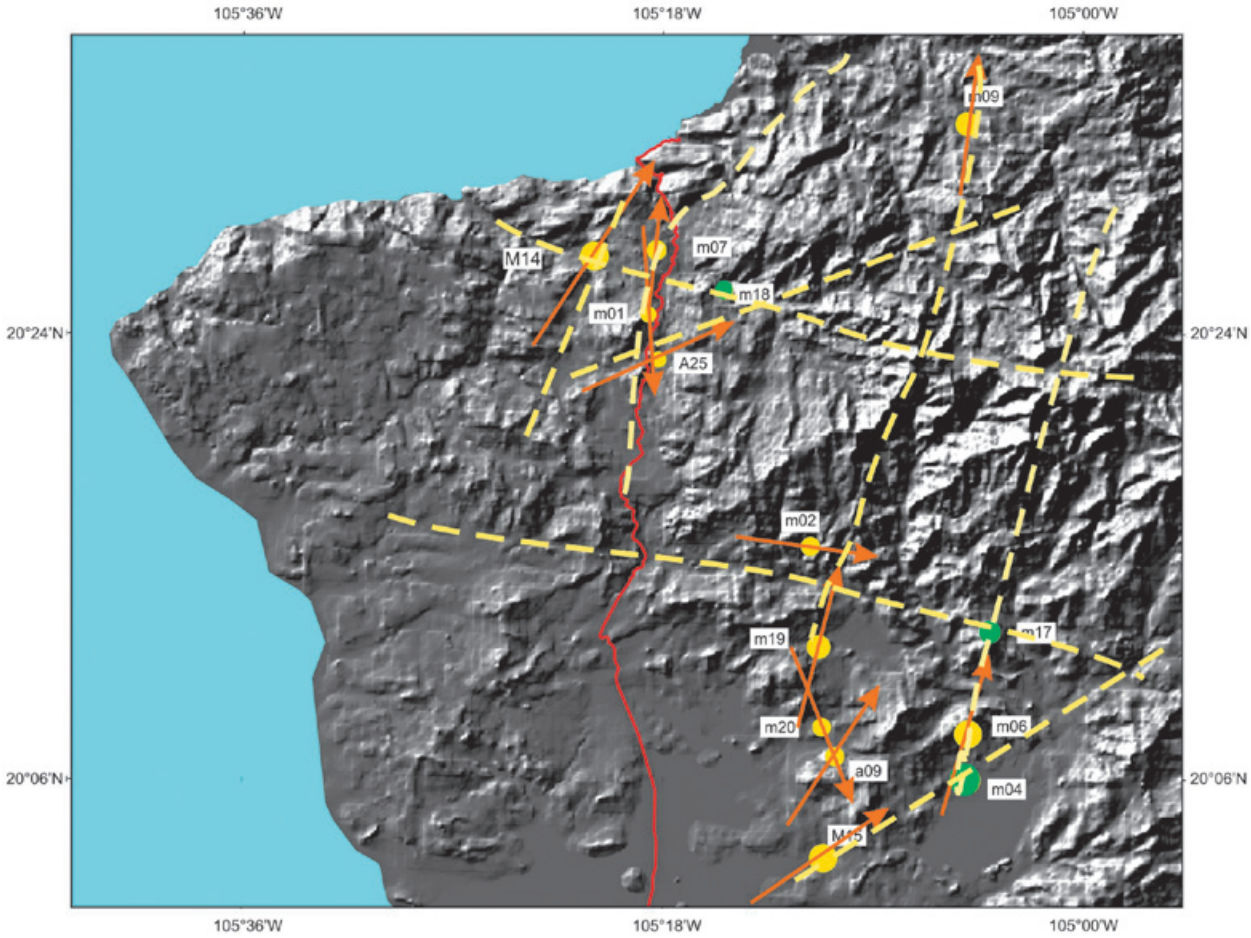

Figure 10. Digital terrain model of the region with main lineaments traced and azimuth of fault planes obtained for the different families referred to location of master event.

Bibliography

Allan J.F., Nelson J., Luhr J., Carmichael J., Wopat M., Wallace P., 1991, Pliocene-Recent rifting in SW México and associated volcanism: An exotic terrane in the making. *Am. Assoc. Petrol. Geol. Mem*., 47, 425-445.

Álvarez R., 2007, Submarine topography and faulting of Bahia de Banderas, Mexico. *Geofísica Internacional*, 46, 2, 93-116.

Console R., Di Giovambattista R., 1987, Local earthquake relative location by digital records. *Phys. Earth planet. Inter.*, 47, 43-49.

Bourgois J., Renard D., Auboin J., Bandy W., Barrier E., Calmus T., Carfantan J.C., Guerrero J., Mammerickx J., Mercier de Lepinay B., Michaud F., Sosson R., 1988, Fragmentation en cours du bord Ouest du Continent Nord Americain: Les frontières sous-marines du Bloc Jalisco (Mexique). C.R. Acad. Sci. Paris 307(II), 1121-1133.

Dañobeitia J.J., Cordoba D., Delgado-Argote L.A., Michaud F., Bartolomé R., Farran M., Carbonell M., Nuñez-Cornú F., the CORTES-P96 Working Group, 1997, Expedition Gathers New Data on Crust Beneath Mexican West Coast. EOS, *Trans. Am. Geophys. Union*, 78, 49, 565-572.

DeMets C., Stein S., 1990, Present-day kinematics of the Rivera Plate and implications for tectonics of Souhtwestern Mexico, *J. Geophys. Res*., 95, 21931-21948.

Deichmann N., García-Fernández M., 1992, Rupture geometry from high-precision relative hypocentre locations of microearthquake clusters, *Geophys. J. Int*., 110, 501-517.

Ferrari L., Pasquaré G., Venegas S., Castillo D., Romero F., 1994, Regional tectonics of

western Mexico and its implications for the northern boundary of Jalisco Block. *Geofísica Internacional*, 33,139-151.

Garduño V.H., Tibaldi A., 1991, Kinematic evolution of the continental active triple junction of the western Mexican Volcanic Belt. C.R. Acad. Sci. Paris, Série II,135-142.

Kostoglodov V., Bandy W., 1995, Seismotectonic constraints on the convergence rate between the Rivera and North American Plates. *J. Geophys. Res.*,100, B9, 17,977-17,989.

Lienert B.R., Berg E., Brazer L.N., 1986, Hypocenter: An earthquake location method using centered, scaled, and adaptively least Squares. *Bull. Seism. Soc. Am.,* 76, 771-783.

Luhr J., Nelson S., Allan J., Carmichael I., 1985, Active rifting in southwestern Mexico: Manifestations of an incipient eastward spreading-ridge jump. *Geology,* 13, 54-57.

Maurer H., Deichmann N., 1995, Microearthquake cluster detection based on waveform similarities, with an application to the western Swiss Alps. *Geophys. J. Int*., 123, 588 – 600.

Núñez-Cornú F., Prol R.M., Cupul-Magaña A., Suarez-Plascencia C., 2000, Near Shore submarine hydrothermal activity in Bahia Banderas. *Geofísica Internacional*, 39, 2,171-178.

Núñez-Cornú F., Rutz M., Nava F.A., Reyes-Davila G., Suárez-Plascencia C., 2002, Characteristics of the Seismicity in the Coast and North of Jalisco Block, MEXICO. *Phys. Earth Planet. Int.,* 132,141-155.

Núñez-Cornú F.J., Reyes-Dávila G.A., Rutz M., Trejo-Gómez E., Camarena-García M.A., Ramírez-Vazquez, C.A., 2004, The 2003 Armería, México earthquake (Mw 7.4): Mainshock and early aftershocks. *Seism. Res. Lett.,* 75, 734-743.

Núñez-Cornú F.J., Rutz-López M., Márquez-Ramírez V., Suárez Plascencia C., Trejo-Gómez E., 2010, Using an Enhaced Dataset for Reassesing the Source Region of the 2003 Armería, Mexico Earthquake. *Pure appl. Geophys.,* 168, 1293-1302. DOI 10.1007/s00024-010-0178-x.

Ocaña E., 2006, Análisis Espacio-Temporal de series sísmicas. La serie de Lorca (Murcia) de 2005. Tesis. Instituto Andaluz de Geofísica.

Rahiman I.H., Pettinga J.R., 2008, Analysis of lineaments and their relationship to Neogene fracturing, SE Viti Levu, Fiji. *Geological Society of America Bulletin*, 120, 11-12, 1544-1555.

Rosas-Elguera J., Ferrari L., Garduño-Monroy V., Urrutia-Fucugauchi J., 1996, Continental boundaries of the Jalisco Block in the Pliocene-Quaternary kinematics of western Mexico. *Geology*, 24, 10, 921-924.

Rutz-López M., 2007, Peligro Sísmico en Bahía de Banderas. M.C. Thesis, Maestria en Geofísica, Univ. de Guadalajara, 77 pp.

Saccorotti G., Carmona E., Ibáñez J.M., Del Pezzo E., 2002, Spatial characterization of Aragon, southern Spain, 1988-1989 seismic series. *Phys. Earth Planet. Int.*, 129, 13-29.

Singh S.K., Ponce L., Ninshenko S.P., 1985, The Great Jalisco, Mexico earthquakes of 1932: Subduction of the Rivera plate. *Bull. Seism. Soc. Am.,* 75, 1301-1313.

Stich D., Alguacil G., Morales J., 2001, The relative locations of multiplets in the vicinity of the Western Almería (Southern Spain) earthquake series of 1993-1994. *Geophys. J. Internt*., 146, 3, 801-812.

Wells D.L., Coppersmith K.J., 1994, New empirical relationships among, Magnitude, Rupture Length, Rupture Wide, Rupture Area and Surface Displacement. *Bull. Seism. Soc. Am.,* 84, 974-1002.

Geofísica Internacional (2013) 52-1: 73-85

Original paper

Morphology and magnetic survey of the Rivera-Cocos plate boundary of Colima, Mexico

Juan Ramón Peláez Gaviria, Carlos A. Mortera Gutiérrez*, William L. Bandy and François Michaud

Received: May 04, 2012; accepted: October 30, 2012; published on line: December 14, 2012

Resumen

La propagación del segmento Pacífico-Cocos de la dorsal East Pacific Rise (EPR-PCS) ha alterado significativamente la configuración de la placa en el extremo norte de la Trinchera Mesoamericana. Esta propagación de la dorsal, la colisión del segmento EPR-PCS con la trinchera Mesoamericana, la separación de las placas Rivera y Cocos, y la formación de la Transformada de Rivera han ocasionado un ensamble complejo de elementos morfo-tectónicos en el área del límite entre placas Rivera-Cocos, contrastante a lo típico de un límite transformante entre placas. Los datos marinos existentes de magnetismo y batimetría han sido inadecuados para resolver esta complejidad, por lo que una malla densa de datos del campo magnético total fue colectada durante las campañas oceanográficas MARTIC-04 y MARTIC-05 del buque oceanográfico B/O El PUMA en 2004 y 2006. Estos datos han clarificado considerablemente el patrón de las lineaciones magnéticas contiguas a la Trinchera Mesoamericana, e interesantemente un alto magnético en forma de *en echelon,* orientado NE-SW observandolo alejado del Graben de Manzanillo, hacia mar. Desafortunadamente, la naturaleza exacta del límite entre Rivera-Cocos permanece imprecisa. Pero estos datos muestran que el segmento de la dorsal EPR-PCS alcanza la latitud (~18.3ºN) de la actual Transformada de Rivera en la isócrona magnética $2A_3$ (~3.5Ma) y se propaga más hacia el norte, interceptando la Trinchera Mesoamericana aproximadamente en 1.7 Ma (Chron 2). En 1.5 Ma, el esparcimiento oceánico cesó a lo largo de la dorsal EPR, al norte de 18.3ºN, y la dorsal EPR-PCS desde entonces ha retrocedido hacia el sur en asociación con la propagación hacia el sur del centro de esparcimiento Moctezuma Spreading Segment (MSS). Al norte de 18.3ºN, el piso oceánico cercano a la trinchera se ha fracturado en menores bloques que presentan levantamientos, posiblemente debido a la subducción de la litosfera recién formada por el EPR-PCS.

Palabras clave: anomalías magnéticas marinas, tectónicas de placas, Dorsal 'East Pacific Rise', trinchera Mesoamericana, reconstrucciones de las placas.

Abstract

The propagation of the Pacific-Cocos Segment of the East Pacific Rise (EPR-PCS) has significantly altered the plate configuration at the north end of the Middle America Trench. This ridge propagation, the collision of the EPR-PCS with the Middle America Trench, the separation of the Rivera and Cocos plates and the formation of the Rivera Transform have produced a complex arrangement of morphotectonic elements in the area of Rivera-Cocos plate boundary, atypical of an oceanic transform boundary. Existing marine magnetic and bathymetric data has proved inadequate to unravel this complexity, thus, a dense grid of total field magnetic data were collected during campaigns MARTIC-04 and MARTIC-05 of the B/O EL PUMA in 2004 and 2006. These data have greatly clarified the magnetic lineation pattern adjacent to the Middle America trench, and have revealed an interesting *en echelon*, NE-SW oriented magnetic high offshore of the Manzanillo Graben. We interpret these new data to indicate that the EPR-PCS ridge segment reached the latitude (~18.3ºN) of the present day Rivera Transform at about Chron $2A_3$ (~3.5Ma) and propagated further northward, intersecting the Middle America Trench at about 1.7 Ma (Chron 2). At 1.5 Ma spreading ceased along the EPR north of 18.3ºN and the EPR-PCS has since retreated southward in association with a southward propagation of the Moctezuma Spreading Segment. North of 18.3ºN the seafloor near the trench has been broken into small, uplifted blocks, perhaps due to the subduction of the young lithosphere generated by the EPR-PCS.

Key words: marine magnetic anomalies, plate tectonics, East Pacific Rise, Middle America Trench, Mexico, plate reconstructions, Rivera-Cocos plate boundary.

J.R. Peláez Gaviria
C.A. Mortera Gutiérrez*
W.L. Bandy
Instituto de Geofísica
Universidad Nacional Autónoma de México
Ciudad Universitaria
Delegación Coyoacán, 04510
México D.F., México
*Corresponding author: cmortera@geofisica.unam.mx

F. Michaud
Géosciences Azur,
La Darse, BP48, 06235
Villefranche-sur-Mer, France

Introduction

The collision of the East Pacific Rise (EPR) with the western margin of the North American Plate has been recorded along the continental margin of North America from Alaska to Mexico (e.g. Atwater, 1989). The most recent collision appears off Manzanillo, Mexico (Figure 1), in the area located between the northern end of the Pacific-Cocos segment of the East Pacific Rise (EPR-PCS) and the Middle America Trench (MAT) where there exists two closely spaced triple junctions formed between the Rivera, Pacific, Cocos and North American plates (e.g. Atwater, 1970; Molnar, 1973). Thus, this site should be ideal for studying the processes associated with the approach and collision of a seafloor spreading center with a subduction zone. Unfortunately, the Rivera-Cocos plate boundary the Rivera Transform and the remnant paleo-Rivera Transform are also located near the collision zone and significantly complicate the morphologic elements associated with this collision (e.g. Bandy, 1992).

The complexity of the seafloor morphology and seafloor magnetic lineations in this area in conjunction with, for the most part, poorly navigated magnetic data and sparse multibeam coverage, has led to several proposals as to the plate configuration and tectonic history of this area (e.g., Mammerickx and Carmichael, 1989; Bourgois and Michaud, 1991; Bandy, 1992; Lonsdale, 1995; DeMets and Wilson, 1997). Thus, to better define the morphology and tectonic history of this area, total field marine magnetic data were collected during two campaigns, MARTIC04 in 2004 and MARTIC05 in 2006, aboard the B/O EL PUMA and combined with multibeam data collected during the 2002 BART/FAMEX campaigns of the NO L'Atalante. Some of the bathymetric data of the BART/FAMEX campaigns conducted in this area have been previously published (Bandy *et al.,* 2005; 2008); however, the majority of the data in the area located between the MAT and the EPR-PCS remained unpublished.

Previous Work

Several proposals exist concerning the evolution of the northernmost segment of the EPR-PCS, particularly regarding its relation to the southern limit of the Rivera plate. Discriminating between these proposals has proved difficult due to the highly complex tectonics of the zone and to the poor spatial coverage of the magnetic and multibeam bathymetric data. Many previous studies have used the seafloor morphology and the seafloor spreading magnetic lineation data to try to resolve the kinematics and deformational history of this area. Some of these studies were of a regional focus (e.g., Mammerickx and Klitgord,

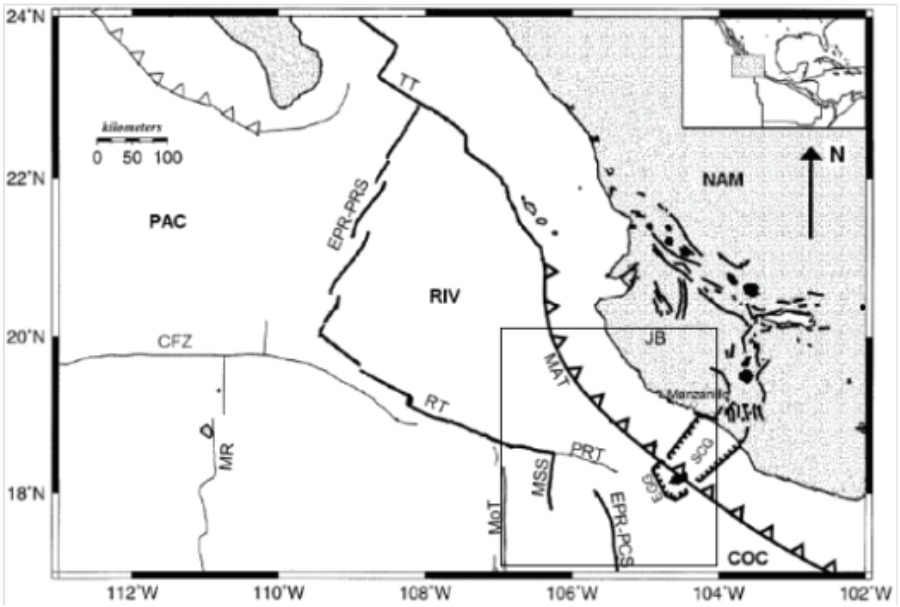

Figure 1. Morphotectonic elements of the study area. The abbreviations are: PAC = Pacific Plate; NAM = North American Plate; COC = Cocos Plate; RIV = Rivera Plate; MR = Mathematician Ridge; MoT = Moctezuma Trough; EGG = El Gordo Graben; SCG = Southern Colima Graben; JB = Jalisco Block; TT = Tamayo Transform; RT = Rivera Transform; PRT = Paleo Rivera Transform; MSS = Moctezuma Spreading Segment; EPR-PRS = East Pacific Rise Pacific-Rivera Segment; EPR-PCS = East Pacific Rise Pacific-Cocos Segment; MAT = Middle American Trench. Modified from *DeMets and Traylen* (2000).

1982; Klitgord and Mammerickx, 1982; Atwater, 1989); whereas others were focused more directly on various aspects of the kinematics of the Rivera Plate (e.g., Eissler and McNally, 1984; DeMets and Stein, 1990; Bandy, 1992; Bandy and Pardo, 1994; DeMets and Wilson, 1997; Bandy *et al.,* 1997, 1998, 2000; DeMets and Traylen, 2000; Jaramillo and Suárez, 2011) or on the complexities of the various boundaries of the Rivera Plate (e.g., Bourgois *et al.,* 1988; Bandy *et al.,* 1995, 2005, 2008; Kostoglodov and Bandy, 1995; Pardo and Suárez, 1995; Lonsdale, 1995; Michaud *et al.,* 1997, 2000, 2001; Bandy *et al.,* 2000; Bandy and Hilde, 2000; Serrato-Díaz *et al.,* 2004). Although all of these studies have made significant contributions to understanding the tectonics of the Rivera plate, they have yet to provide a clear understanding of either the recent evolution of the northernmost segment of the EPR-PCS, or the nature of the Rivera-Cocos plate boundary.

Mammerickx and Klitgord [1982] and Klitgord and Mammerickx [1982] showed that the magnetic lineations of the EPR formed since 5 Ma document a relocation of seafloor spreading from the Mathematician Ridge to the present location of the EPR as the EPR propagated northward from the Orozco Facture Zone to the area of the Rivera Transform. They proposed that the propagation ceased at about 3.5 Ma (Figure 2A) and that the northward extent of the propagation was at the Rivera Transform. In contrast, Bandy (1992) (see also Bandy and Hilde, 2000) proposed that the EPR-PCS propagated north of the Rivera Transform, reaching its northern limit near the MAT at ~1.77Ma (Figure 2B). They also proposed that at 1.5 Ma (Figures 2C and 2D), the part of this spreading center located north of the Rivera Transform was abandoned/decapitated by the formation of the Rivera Transform, a proposal that is consistent with the subsequent findings of Lonsdale (1995). Michaud *et al.* (2001) proposed that the EPR-PCS may have extended even further northward than that proposed by Bandy (1992) and that the ridge segment north of the Rivera Transform has since been subducted beneath the Jalisco Block (Figure 2C).

The nature of the boundary between the Rivera and Cocos plates, as well as the relative motion across the boundary, is also controversial and various proposals have been presented. These proposals can be classified into three main groups. The first group proposes that the boundary is a generally NE-SW oriented sinistral transform boundary, the exact orientation and location being somewhat different in the various proposals (Atwater, 1970; Molnar, 1973; Reid, 1976; Nixon, 1982; Eissler and McNally, 1984; Mammerickx and Carmichael, 1989; DeMets and Stein, 1990; Lonsdale, 1995). A variant on this proposal is that of DeMets and Wilson (1997) who proposed that the boundary is a difuse zone of left lateral, NNE-SSW oriented shearing. The second group (Bandy, 1992; Kostoglodov and Bandy, 1995; Bandy *et al.,* 1995, 1998, 2000; Bandy and Hilde, 2000; Serrato-Díaz *et al.,* 2004) proposes that El Gordo Graben is the tip of a rift between the Rivera and Cocos plates and that this rift is currently propagating SW towards the EPR, resulting in a situation that is analogous

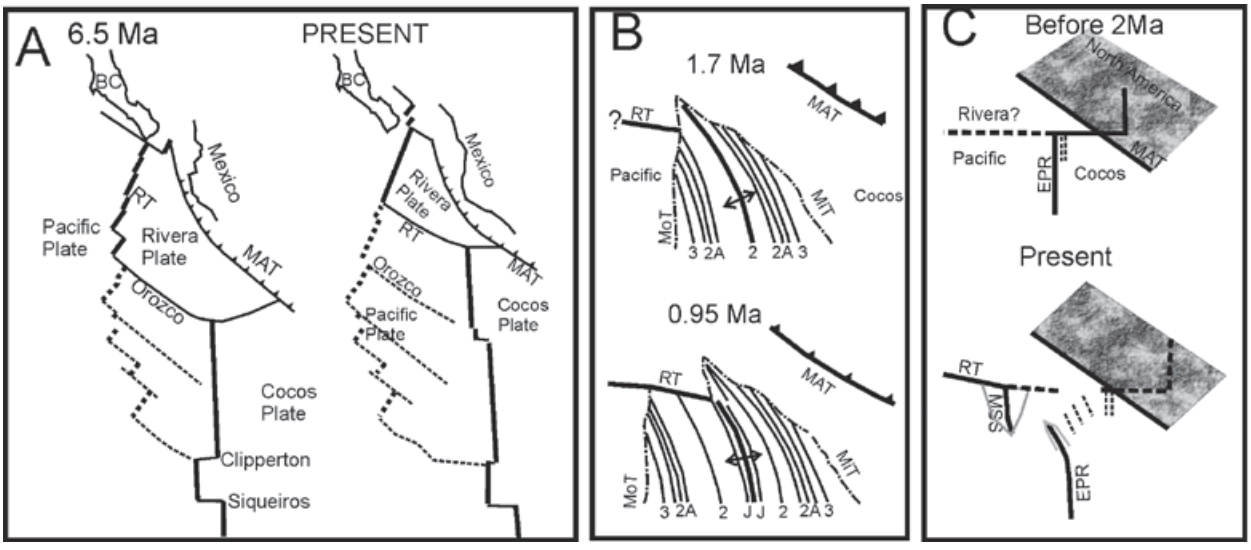

Figure 2. Previous models for the evolution of the area between the EPR, RT and MAT off Manzanillo. A) Mammerickx and Klitgord (1982) for the periods 6.5 Ma and the present day. (B) Bandy and Hilde (2000) for 1.7 Ma and 0.95 Ma. (C) Michaud *et al*. (2001) for the periods 2 Ma and the present day.

to the present day Galapogos triple junction (Lonsdale, 1988). The divergence between the Rivera and Cocos plates is proposed by Bandy (1992) to be the result of the ridge-trench collision off the southern tip of Baja California at about 8 Ma (Lonsdale, 1991) and subsequent pivoting of the Rivera plate away from the rest of the Cocos Plate, a proposal that is consistent with the results of recent seismic studies (Yang, *et al.,* 2009; León Soto *et al.,* 2009). The third group proposes that it is a diffuse boundary between the Cocos and North American plates (Michaud and Bourgois, 1995; Michaud *et al.,* 1997).

Data and Methods

Two primary data sets were used in this study. The first consists of the previously unpublished total field magnetic data obtained during the MARTIC04 (October 28-November 9, 2004) and MARTIC05 (January 10-31, 2006) campaigns of the B/O EL PUMA. The ship tracks along which the magnetic data was collected are shown in Figure 3. The second data set consists of the multibeam data collected in the study area during the BART/FAMEX campaigns of the NO L'Atalante conducted in 2002: these data are previously unpublished except near the Moctezuma Spreading Center (MSS) where they have been published in Bandy *et al*. (2008). These data were supplemented with data from the following sources: Ridge Project database, United States National Geophysical Data Center (NGDC), USGS and Harvard earthquake databases. The ages of the lithosphere in the study area were determined from the seafloor marine magnetic lineations, constrained by one recent radiometric age determination of one seafloor sample dredged during MARTIC04 (Canet *et al.,* 2008). The details of this age determination are given in Schaaf *et al.* (manuscript in preparation).

Total field marine magnetic data were collected using a GEOMETRICS G877 marine proton precession magnetometer which has a resolution of 0.1 nT (Geometrics, Inc., 2001). To avoid ship effects, the sensor was towed 250 meters behind the B/O EL PUMA, which has a length of 50 meters. A measurement was taken every 2 seconds. The locations of the measurements have been corrected for layback as the data were being recorded using the GEOMETRICS MAGLOG light program.

To correct for the diurnal variation during MARTIC-04, a permanent base station was installed (19º 7' 20.68'' N y 104º 23' 59.36'' W) within the 'El Naranjo' campus of the Universidad del Mar de Colima, Manzanillo, Colima. Readings were taken with the Sintrex Envimag proton precession magnetometer at 5 min intervals. A magnetic storm began on November 7 and

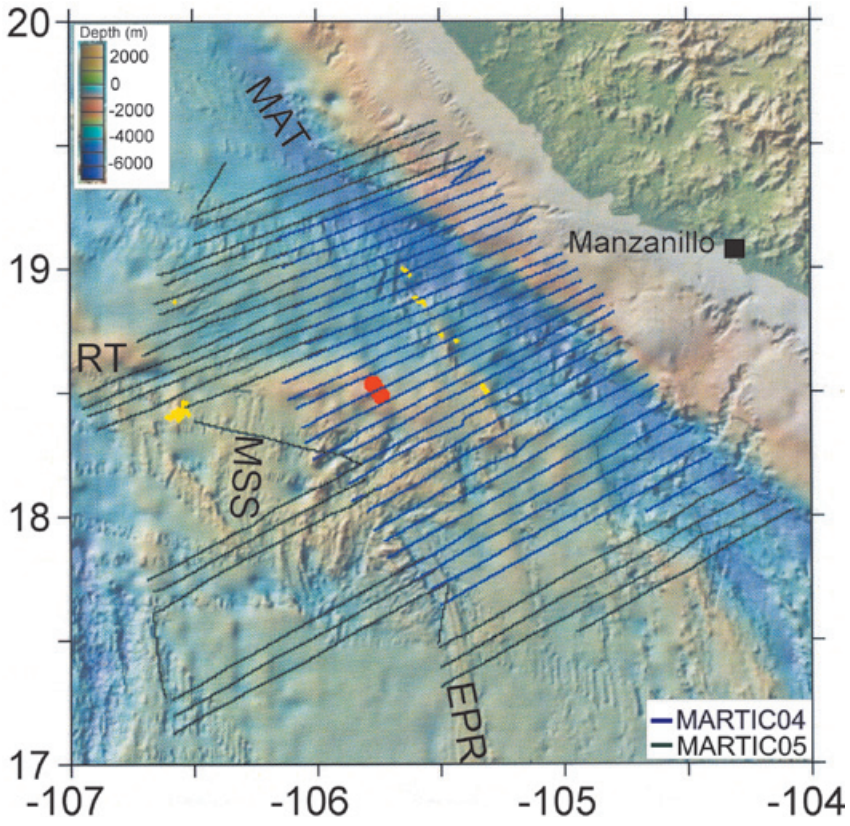

Figure 3. Map of the ship tracks along which the magnetic data was collected. The tracks of MARTIC04 are shown in blue and those of MARTIC05 are shown in green. Dredge sites are shown in red (samples obtained and age dated) and yellow (no sample obtained). Background bathymetry map from GeoMapApp (www.geomapapp.org).

data collected during the storm were not used. The base station magnetometer was down on November 1 and November 2. For these two days, the magnetic record from the permanent observatory at Teoloyucan, México was used to make the diurnal corrections, after having been shifted to fit the Colima data. More information on the treatment of the base station data can be found in Peláez Gaviria (2008).

To correct for the diurnal variation during MARTIC-05, a permanent base station was set up in the UNAM Biological Reserve, Chamela, Jalisco (19º 29' 56.1'' N y 105º 02' 32.1'' W). Readings were taken at 1 minute intervals using a GEOMETRICS G856AX proton precession magnetometer.

The selection criteria for both base stations were that the stations were located (1) in an area having a low magnetic gradient (<4.5 nT/m), (2) less than 150 km from the study area, (3) more than 60 meters from buildings, roads, power lines, or any other objects that might generate magnetic noise (Breiner, 1973).

After removing the diurnal variation the data were next corrected for ship's heading following the methods presented by Bullard and Mason (1961), Whitmarsh and Jones (1969) and Buchanan *et al*. (1996). Next, these values were reduced to magnetic anomaly values by subtracting out the value of the main field using the IAGA IGRF-10 Model which was obtained from the United States National Geophysical Data Center.

The multi-beam bathymetric data of the 2002 BART/FAMEX campaigns were collected with a dual SIMRAD EM-12 multi-beam system and the raw data was processed using the CARAIBES software while onboard by IFREMER technicians to produce a 200 x 200 meter grid of bathymetric values. These values were combined with existing multibeam data to produce a new bathymetry map (Figure 4).

Results

The new map of the seafloor magnetic anomaly lineations (Figure 5) indicates that in the southern part of the study area, the recent magnetic anomalies are for the most part continuous and undisrupted south of 17.6°N, consistent with the seafloor morphology (Figure 4). North of 17.6°N, in the area immediately west of the EPR-PCS, the older lineations are unidentifiable as they have been disrupted both by the recent southward propagation of the MSS and the recent northward propagation of the northern tip of the EPR-PCS. The lineations are also unidentifiable in the area located between the active tip of the EPR-PCS and the Paleo-Rivera Transform.

East of the EPR-PCS two abandoned ridge segments are identified (segments P1 and P2, Figure 5). The magnetic lineations indicate that seafloor spreading along ridge segment P1 ceased just after the time of anomaly 1R as Anomaly J is observed to both sides of P1. This is slightly older than that proposed by Bandy *et al.* (2008) who proposed that P1 was abandoned at 0.7 Ma based on the anomaly pattern along the MSS. The time of abandonment of P2 is not determinable from the magnetic data. However, P2 is most likely associated with a southward cessation of spreading along the EPR-PCS and therefore, seafloor spreading along P2 most likely ceased within the past 0.78 m.y.

Between P1 and the MAT, anomalies 3_1 to 1R are observed within the study area. Anomalies 3_1 to $2A_2$ terminate at the southern boundary of the El Gordo Graben, whereas anomalies1R and J extend undisrupted northward to the latitude of the paleo-Rivera Transform. Anomaly $2A_1$ and Anomaly 2 also appear to extend northward to 18.5°N. However, in contrast to anomalies 1R and J, anomalies 2 and $2A_1$ are disrupted, particularly in the area just west of the El Gordo Graben at 18.0°N where both anomalies exhibit a significant decrease in their magnitudes. On the north flank of this area of decreased magnitude, Anomaly $2A_1$ may be deflected westward (i.e. the crust appears to be rotated clockwise). On the south flank of this area of decreased magnitude, Anomaly 2 also appears to bend slightly westward. This pattern of disruption is consistent with the proposal of Bandy (1992) that the El Gordo Graben is the tip of a SW propagating rift situated between the Rivera and Cocos plates.

Also to the east of the EPR, Anomaly $2A_1$ exhibits a prominent westward deflection at 18.4°N where it approaches a prominent, ENE-WSW elongated, magnetic high (henceforth is termed the "Manzanillo Magnetic Lineament"). This westward bend suggests that the area of the Manzanillo Magnetic Lineament may be located within a generally east-west trending sinistral shear couple.

Consistent with previous studies (e.g. Lonsdale, 1995), the older magnetic lineations located north of the Rivera Transform, lineations $4A_1$ to $5N_2$, are deflected westward as they approach the Rivera Transform, in good agreement with the bathymetric data (Figure 4). In contrast, the new data shows that none of the lineations located east of $5N_2$ are deflected westward; instead they exhibit a slight eastward deflection as they approach the Manzanillo Magnetic Lineament. This is also observed in the bathymetric data where a difference in the seafloor morphology is observed to either side of 105.8ºW north of the Rivera Fracture Zone/

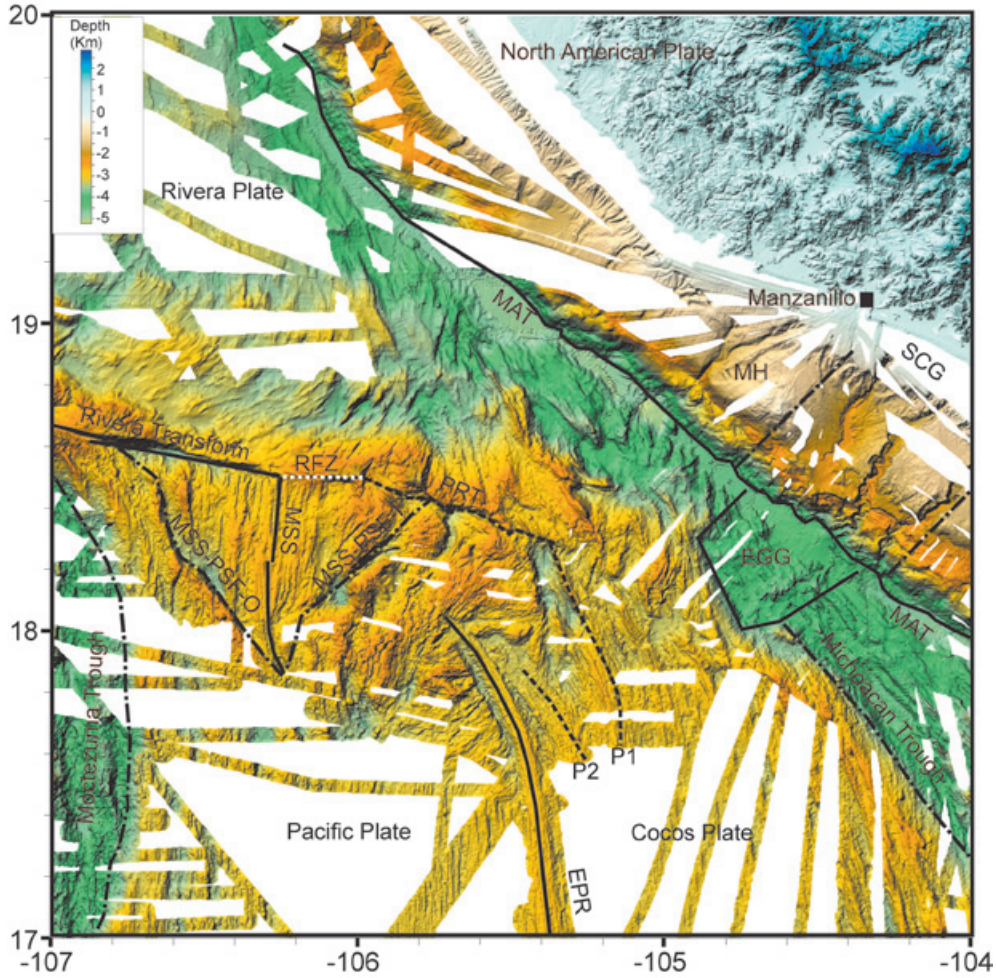

Figure 4. Principle morphotectonic elements superimposed on bathymetry. The bathymetry map was constructed using the available multibeam, including previously unpublished data from the 2002 FAMEX/BART campaigns. Abreviations are: RFZ = Rivera Fracture Zone; MH = Manzanillo horst; MSS-PSF-O = Outer Pseudo-Fault associated with the propagation of the Moctezuma Spreading Segment; MSS-PSF-I = Inner Pseudo-Fault associated with the propagation of the Moctezuma Spreading Segment; P1 y P2: relict spreading segments of the EPR. Other abbreviations are those used in Figure 1.

paleo-Rivera Transform (terminology from Bandy *et al.* (2008)). The broad positive anomaly located just east of Anomaly $5N_2$ has been tentatively identified as Anomaly 2 by Bandy (1992). This anomaly terminates against the west end of the Manzanillo Magnetic Lineament) and it intersects the MAT off Chamela, Jalisco (at 19.3°N).

The Manzanillo Magnetic Lineament consists of two ENE-WSW segments which are offset in a right-stepping manner in the trench. This lineament is aligned with the Manzanillo graben (e.g., Bandy *et al.,* 1993) and its projection is towards the port of Manzanillo. It is tempting to associate this lineament with a transform boundary between the Rivera and Cocos plates, however the lineament does not coincide with any bathymetric feature typically associated with a major transform plate boundary (Figures 4 and 6). Further, the right-stepping offset of the two segments of the lineament indicates that if it were a transform, the sense of motion would be dextral. This is in contrast to the sinistral sense of motion indicated by the deflection of Anomaly 2 across the lineament as noted above. Hence, the origin of this lineament is uncertain.

The bathymetry in this area can be divided into several morphotectonic zones (Figure 6). Several of these zones have been described in previous studies. These include: (1) zones A which are clearly formed in relation to the propagation of the EPR-PCS and MSS (Mammerickx,1984; Bandy, 1992; and Bandy *et al.,* 2008); (2) zones F (west of the Moctezuma Trough and east of the Michoacan trough) are the old crust created at the Mathematician Ridge through which the EPR propagated (Mammerickx and Klitgord, 1982;

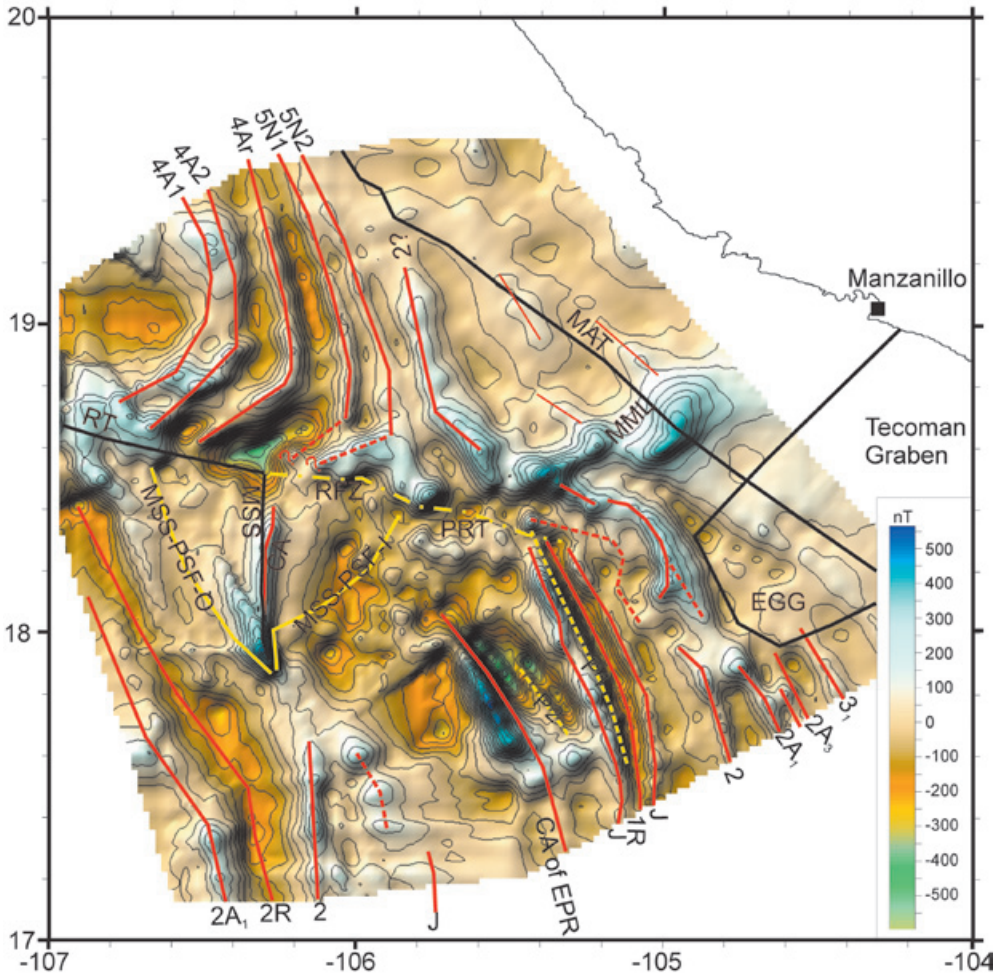

Figure 5. Magnetic anomaly map. The principle morphotectonic elements are superimposed to aid in the interpretation. Number on the lineations are the lineation identifications. MML = Manzanillo Magnetic Lineament. See figures 1 and 4 for definitions of the other abbreviations.

Klitgord and Mammerickx, 1982); and (3) Zone B is the old crust formed at the Rivera Rise which is bent westward as it approaches the Rivera Transform. This bending has been proposed to be due to shearing during the initial formation of the Rivera Transform (Lonsdale, 1995).

Several previously undiscribed morphotectonic zones can be seen in the new bathymetric map. The first of these, Zone C, confirms that the EPR-PCS has indeed propagated north of the paleo-Rivera transform as proposed by Bandy (1992). The western limit of this zone is clearly marked by a change in seafloor fabric as well as by a prominent escarpment (the tectonic pseudofault of the propagator) that is down-dropped to the east (Figure 4). The seafloor spreading fabric within zone C trends NNW-SSE and unlike the seafloor fabric in zone B to the west, the seafloor fabric does not bend westward as it approaches the paleo-Rivera Transform. This spreading fabric is cut by two short, parallel, NNE-SSW striking faults near the MAT at 19°N (Figure 4). The eastern tectonic pseudofault of Zone C is not entirely clear, but may correspond to the NNW-SSE bathymetric ridge located between -105.2° and -105.4°. The age of the seafloor within zone C on its western side (see Figure 3 for location) has been dated as 1.4 ± 0.7 Ma and 1.3 ± 0.3 Ma (Schaaf *et al*., 2009), consistent with the proposal that the broad, anomaly located east of anomaly $5N_2$ may indeed be Anomaly 2.

The new bathymetric data also indicates that the MAT in this area can be subdivided into three morphologic zones (D1, D2 and E on Figure 6). A prominent east-west oriented, down-to-the-north escarpment (for reasons ex-plained in the next section, this escarpment is called the Paleo-Transformada de Colima or the PCoT) separates zone D1 to the north from zone D2. North of the PCoT the flat trench floor widens

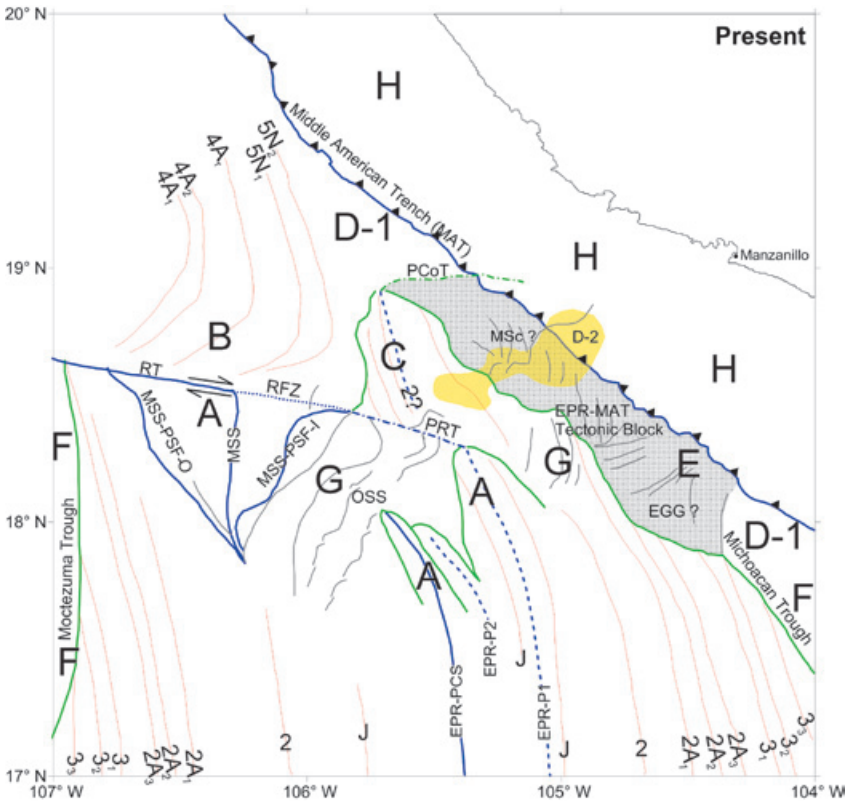

Figure 6. Magnetic anomaly lineations superimposed on a schematic representation of the different morphotectonic zones in the study area. See text for details. PCoT = Paleo-Colima Transform, OSS = Overlapping Spreading System, MSc = Manzanillo Escarpment, Morphologic zone H is the Continental Shelf. See figures 1 and 4 for definitions of the other abbreviations.

abruptly. Zone E is the El Gordo Graben area (Bourgois *et al.,* 1988) which is a zone of high heat flow (Khutorskoy *et al*., 1994) and thinned oceanic crust (Serrato–Diaz *et al.,* 2004). Zone D-2 is a previously unrecognized zone containing seamounts, fault scarps (the most prominent of which is herein referred to as the Manzanillo Escarpment) oriented perpendicular to the strike of the trench and small bathymetric ridges that rise above the sediment cover. Zones D-1 are the typical trench morphotectonic domains. The morphologic complexities of zones D-2 and E are most likely associated with deformation within the Rivera-Cocos Plate Boundary. It is also important to note that zone D-2 contains the Manzanillo Magnetic Lineation.

The part of Zone G located just west and NW of the El Gordo Graben, was first identified near the trench by Michaud *et al.* (2000). The seafloor in this zone is oriented clockwise of that exhibited by the crust formed at the EPR-PCS. Michaud *et al*. (2000) propose that this difference in reorientation may reflect older crust formed along the EPR-PCS prior to 1.5 Ma. Alternatively, it may in reflect the disruption of young crust formed at the EPR-PCS due to the SW propagation of the El Gordo Graben towards the EPR (Bandy, 1992), or more generally, to disruption related to the development of the Rivera-Cocos plate boundary.

Tectonic history of the Rivera-Cocos plate boundary

The results of this study in conjunction with the results of prior studies indicate that the complex morphology in the boundary between the Rivera and Cocos plates is the result of the effects of (1) the northward propagation of the EPR-PCS through the older, pre-existing seafloor formed at the Rivera Rise and its eventual collision with the MAT off Chamela, (2) the subsequent decapitation of the EPR-PCS during the initial formation of the Rivera Transform, (3) deformation associated with the formation of the Rivera-Cocos plate boundary, and (4) reorganizations of both the location and directions of propagation (i.e. several episodes of self-decapitation (Macdonald *et al.,* 1988) or cyclic rift failure (Wilson, 1990) and the formation of the MSS).

The new revision of the magnetic anomalies, the new age date and the new multibeam bathymetric data confirm the presence of a relict spreading center that propagated past the latitude of the El Gordo Graben terminating at the MAT (~19.2ºN) at ~1.7Ma (Figure 7). At this time the

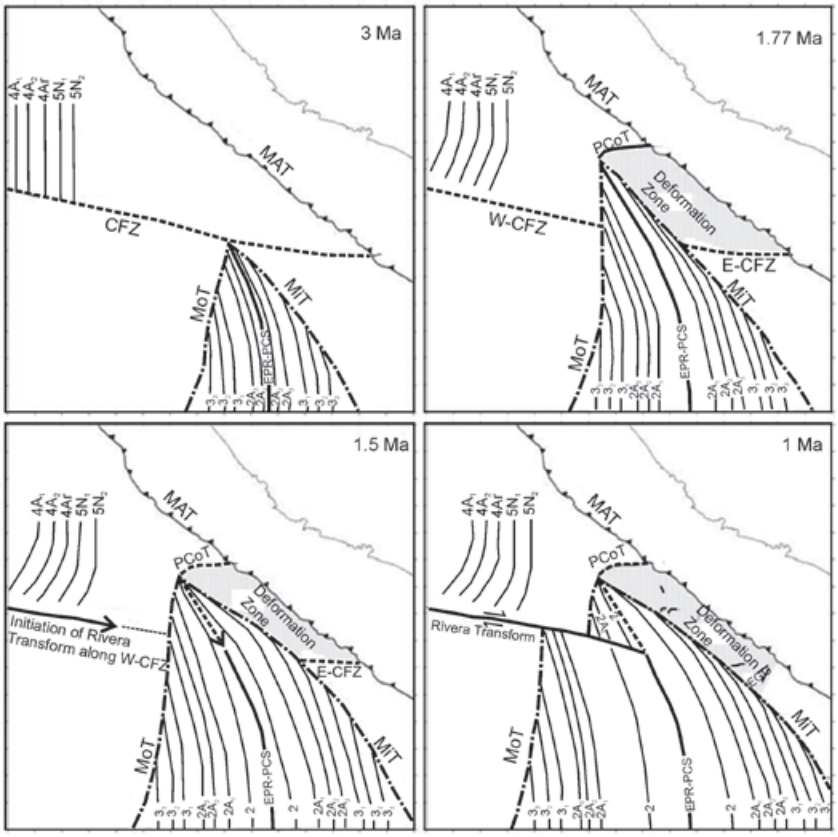

Figure 7. Schematic representations of the tectonic evolution from 3 Ma to 1.0 Ma.

PCoT may have formed in a manner proposed by Michaud *et al.* (2000). Specifically, prior to the southward cessation of spreading, the PCoT may have formed as a transform linking the tip of the EPR-PCS with the MAT. If so, the presence of the PCoT implies that a segment of the EPR has been subducted below the Jalisco margin north of Chamela (see Figure 2b). Shortly after 1.7Ma, the spreading center was abandoned perhaps as a gradual southward progressing cessation of spreading, or as an abrupt decapitation due to the formation of the Rivera Transform at 1.5 Ma.

Between 1.5 and 0.7 Ma the EPR-PCS stabilized at the present-day relict spreading center P1 and the Rivera Transform-EPR eastern junction was located at the northern tip of P1. It is very tempting to propose that the Manzanillo Magnetic Lineament was a transform boundary between the Rivera and Cocos plates during this time. However this is unclear as the western extent of this lineament lies to the north of the junction of the paleo-Rivera Transform with P1 and the morphology associated with this lineament is not convincingly that of a major plate boundary transform. Alternatively, since 1.5 Ma the area east of the decapitated EPR tip, west of the MAT, south of the PCoT and north of the inferred East Clarion Fracture Zone (E-CFZ), appears to have been broken into small crustal blocks that have been rotated and uplifted: the Manzanillo Magnetic Lineation, and its associated Manzanillo Escarpment, may be a result of this deformation.

At about 0.7 Ma the plate boundary again became unstable and the EPR-PCS once again began to retreat southward undergoing at least two episodes of self-decapitation which resulted in relict rift P1 and the present day rift tip which has recently been propagating northward and may be decapitated in the future. In conjunction with this new period of southward cessation of spreading along the EPR-PCS, the MSS has propagated southward since its inception at 0.7 Ma (Bandy, 1992; Bandy *et al.,* 2008) which has led to the present-day morphology illustrated in Figure 6.

Clearly, the present-day morphotectonic elements are not those typically observed for major transform plate boundaries, and as a result the nature of the boundary remains unclear. The deformation of the bathymetry and magnetic lineations west of the El Gordo Graben are clearly consistent with a SW propagating zone of extension between the Rivera and Cocos plates as proposed by Bandy (1992). However, this alone would not explain the strike slip focal mechanism solutions

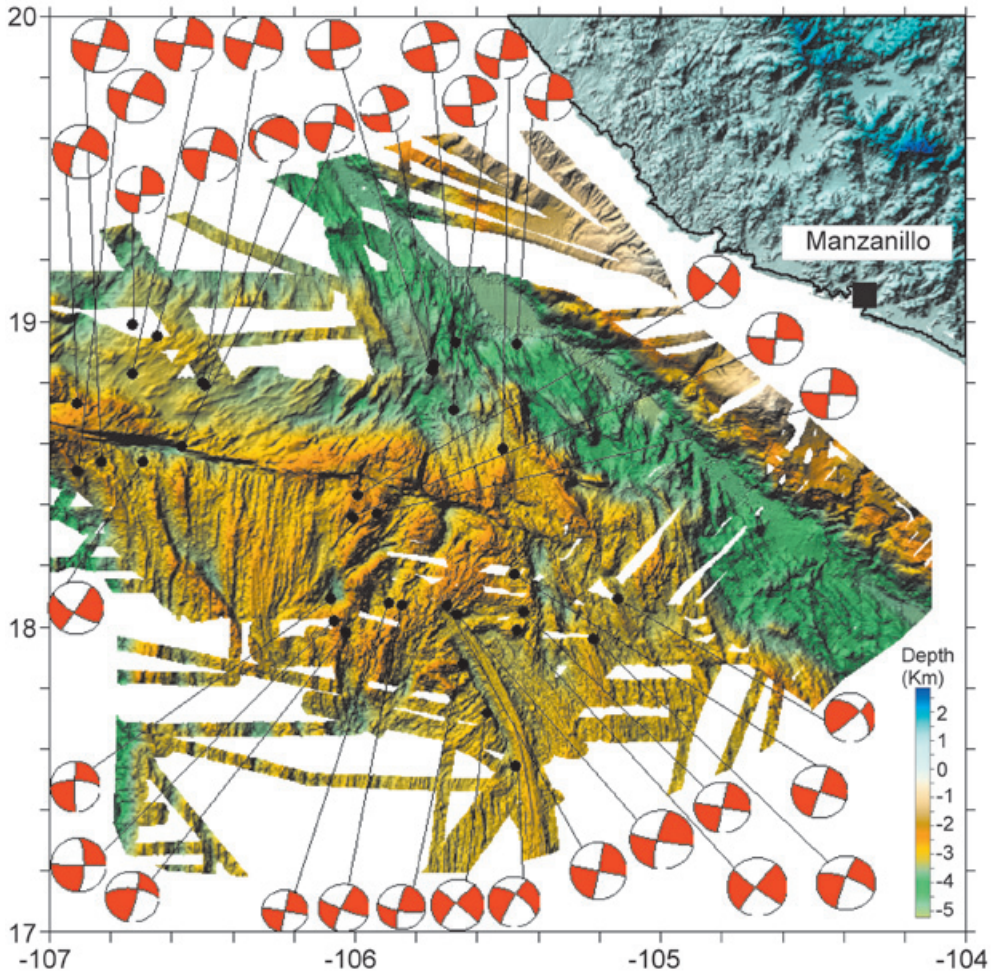

Figure 8. Earthquake Centroid Moment Tensor solutions (as of July 2007) superimposed on the new bathymetry map. Note the strike slip mechanisms within the area just seaward of the MAT. Focal mechanism solutions obtained from the USGS (http://neic.usgs.gov/neis/sopar/) and the Centroid Moment Tensor Catalogue (2007) (http://www.globalcmt.org/CMTsearch.html).

for events occurring in this region (Figure 8). Alternatively, the most prominent deviation in the magnetic lineations occurs north of the El Gordo graben, at the Manzanillo Magnetic lineament. However, the orientation of this lineament is not consistent with the orientation of the nodal planes of the focal mechanisms of earthquakes occurring in this area; this magnetic lineation does not poses a transform morphology; and it does not cut across morphotectonic zone C (i.e. it does not connect with either the MSS or with the EPR-PCS). Thus, it does not appear to be the present day boundary. Given the magnetic and morphologic signature of this area, the present day Rivera-Cocos boundary, if it exists, appears to be a broad zone of deformation, extending from the El Gordo Graben, at which it appears to be extensional, to 19°N where is appears to be subjected to either N-S or E-W oriented shear stresses.

Conclusions

The principle conclusions of this study are:

(1) The development of the Rivera-Cocos plate boundary is influenced by the evolution of the EPR-PCS and its close proximity to the MAT as well as by the formation of the Rivera Transform.

(2) A prominent high amplitude, en echelon, magnetic anomaly oriented roughly perpendicular to the MAT is observed between 18.4°N and 18.8°N. This anomaly (the Manzanillo Magnetic Lineament) consists of two, right-stepping, en-echelon segments and is aligned with the Manzanillo Trough formed within the continental slope and shelf area of the overriding North American plate. Anomaly $2A_1$ bends sharply westward as it approaches this lineament from the south indicated that it marks a crustal discontinuity.

(3) The origin of the Manzanillo Magnetic Lineament is uncertain. It connects with neither the MSS nor the active EPR-PCS, thus, it does not appear to be an active plate boundary. The lineament coincides with the Manzanillo Escarpment: however, this morphologic feature is not typical of a transform plate boundary. Thus, it does not appear to be an older, presently inactive plate boundary.

(4) The anomalies on the Rivera plate north of the Manzanillo Magnetic Lineation exhibit a slight eastward bend as they approach this lineation, in sharp contrast to lineations of the Rivera plate to the west (e.g., Anomalies $5N_2$, $5N_1$, 4Ar, etc.) which bend sharply westward as they approach the Rivera Transform/Paleo-Rivera Transform.

(5) The EPR-PCS propagated northward, past the present day location of the Rivera Transform, intersecting the MAT at about 1.7 Ma. The present day location of the ridge trench intersection is off Chamela, Jalisco at 19.2ºN.

(6) At 1.5 Ma, spreading ceased north of the present day location of the Rivera Transform, perhaps being decapitated by the formation of the Rivera Transform.

(7) Since 1.5 Ma the EPR-PCS has undergone an overall southward cessation of spreading, during which short pulses of northward ridge propagation and subsequent abandonment occurred, leaving behind several relict rift tips.

(8) The morphotectonic elements of the boundary zone do not clearly define the nature of the plate boundary, however these elements in conjunction with earthquake focal mechanisms of events occurring in the boundary zone suggest that the boundary is a broad zone where N-S extension is occurring in the southern part of this zone, whereas the northern part of the zone is dominated by shear stresses.

Acknowledgments

We thank the Captain, crew and administrative staff of the BO El PUMA for their help during the collection of the marine magnetic data; G. Suárez for helpful discussions; Peter Schaaf, Margarita López and the staff of the Geochronology Laboratory of CICESE who dated the basalt sample, the Coordinación Académica de Buques Oceanográficos (CABO), UNAM for providing the ship time during the MARTIC04 and MARTIC05 campaigns, Esteban Hernández and the staff of the UNAM Geomagnetic Observatory in Teoloyucan, Mexico for their help in establishing and maintaining the magnetic base stations data deployed for this work. The MARTIC04 and MARTIC05 campaigns were funded by UNAM-DGAPA grants IN117305-2, IN116505, IN114410, IN102507 and IN104707-3, CONACyT grant F50235 and Instituto de Geofísica, UNAM grant G111. The BART- FAMEX campaigns of the N.O. L'Atalante were funded by grants from the Centre National de la Recherche Scientifique (CNRS), France and CONACyT grant #T36681, Mexico. Partial funding during the analysis phase was also provided by CONACyT grant #50235-F. We thank the reviewers for their comments which helped improve the clarity of the manuscript.

Bibliography

Atwater T., 1970, Implications of plate tectonics for the Cenozoic tectonic evolution for western North America. GSA Bull., 81, 3513-3536.

Atwater T., 1989, Plate tectonic history of the northeast Pacific and western North America, In *The Eastern Pacific Ocean and Hawaii: Geology of North America*, Vol. N, (eds. Winterer, E.L., Hussong, D.M., and Decker, R.W.) (GSA, Boulder, Colorado, USA.) pp. 21-72.

Bandy W.L., 1992, Geological and Geophysical Investigation of the Rivera-Cocos Plate Boundary: Implications for Plate Fragmentation. Ph.D. Dissertation, Texas A&M University, College Station, Texas, 195p.

Bandy W., Pardo, M., 1994, Statistical examination of the existence and relative motion of the Jalisco and Southern Mexico Blocks. *Tectonics,* 13*,* 4, 755–768.

Bandy W. L., Hilde, T.W.C., 2000, Morphology and recent history of the ridge propagator system located at 18ºN, 106ºW, In *Cenozoic Tectonics and Volcanism of Mexico*, Special Paper 334, (eds. Delgado-Granados, H., Aguirre Diaz, G., and Stock, J.M.) (Geological Society of America, Boulder, Colorado), pp 29-40.

Bandy W.L., Mortera-Gutiérrez C.A., Urrutia-Fucugauchi J., 1993, Gravity Field of the southern Colima graben, Mexico. *Geofísica Internacional,* 32, 561-567.

Bandy W.L., Mortera-Gutiérrez C., Urrutia-Fucugauchi J., Hilde T.W.C., 1995, The subducted Rivera-Cocos plate boundary: Where is it, what is it, and what is its relationship to the Colima rift?. *Geophys. Res. Lett.,* 22, 3075-3078.

Bandy W.L., Kostoglodov V., Singh S.K., Pardo M., Pacheco J., Urrutia-Fucugauchi J., 1997, Implications of the October 1995 Colima-Jalisco Mexico earthquake on the Rivera-North America Euler vector. *Geophys. Res. Lett.,* 24, 485-488.

Bandy W.L., Kostoglodov V., Mortera-Gutiérrez C.A., 1998, Southwest migration of the Instantaneous Rivera-Pacific Euler pole Since 0.78 Ma. *Geofísica Internacional,* 37, 153-169.

Bandy W.L., Hilde T.W.C., Yan C.-Y., 2000, The Rivera-Cocos plate boundary: Implications for Rivera-Cocos relative motion and plate fragmentation, In *Cenozoic Tectonics and Volcanism of Mexico*, Special Paper 334, (eds. Delgado-Granados, H., Aguirre Diaz, G., and Stock, J.M.) (Geological Society of America, Boulder, Colorado), pp 1-28.

Bandy W.L., Michaud F., Bourgois J., Calmus T., Dyment J., Mortera-Gutiérrez C.A., Ortega-Ramírez J., Pontoise B., Royer J.-Y., Sichler B., Sosson M. Rebolledo-Vieyra M., Bigot-Cormier F., Díaz-Molina O., Hurtado-Artunduaga A.D., Pardo-Castro G., Trouillard-Perrot C., 2005, Subsidence and strike-slip tectonism of the upper continental slope off Manzanillo, Mexico. *Tectonophysics,* 398(3-4), 115-140.

Bandy W.L., Michaud F., Dyment J., Mortera-Gutiérrez C.A., Bourgois J., Calmus T., Sosson M., Ortega-Ramírez J., Royer J.-Y., Pontoise B., Sichler B., 2008, Multibeam bathymetry and sidescan imaging of the Rivera transform-Moctezuma spreading segment junction, northern East Pacific rise: New constraints on Rivera-Pacific relative plate motion. *Tectonophysics,* 454 (1-4), 70-85, doi: 10.1016/j.tecto.2008.04.013.

Bourgois J., Michaud F., 1991, Active fragmentation of the North American Plate at the Mexican triple junction area off Manzanillo. *Geo-Marine Lett.,* 11, 59-65.

Bourgois J., Renard V., Aubouin J., Bandy W., Barrier E., Calmus T., Carfantan J.-C., Guerrero J., Mammerickx J., Mercier de Lepinay B., Michaud F., Sosson M., 1988, Active fragmentation of the North American plate: offshore boundary of the Jalisco block off Manzanillo. *C.R. Acad. Sci. Paris,* Serie 2, 307, 1121-1130.

Breiner S., 1973, *Applications manual for portable magnetometers* (Geometrics, San Jose, California, USA).

Buchanan S. K., Scrutton R.A., Edwards R.A., Whitmarsh R.B., 1996, Marine magnetic data processing in equatorial regions off Ghana. *Geophys. J. Int.,* 125, (1), 123–131.

Bullard E.C., Mason R.G., 1961, The magnetic field astern of a ship. *Deep Sea Research,* 8, (1), 20-27.

Canet C., Prol-Ledesma R.M., Bandy W.L., Schaaf P., Linares C., Tauler E., Mortera-Gutiérrez C., 2008, Mineralogical and geochemical constraints on the origin of ferromanganese crusts from the Rivera Plate (western margin of Mexico). *Marine Geology,* 251, 47-59.

Centroid Moment Tensor Catologue, www.seismology.harvard.edu/CMTsearch.html (last accessed July 2007).

DeMets C., Traylen S., 2000, Motion of the Rivera plate since 10 Ma relative to the Pacific and North American plates and the mantle. *Tectonophysics,* 318, 119–159.

DeMets C., Wilson D.S., 1997, Relative motions of the Pacific, Rivera, North American, and Cocos plates since 0.78 Ma. *J. Geophys. Res.,* 102, (B2), 2789–2806.

DeMets C., Stein S., 1990, Present-day kinematics of the Rivera Plate and implications for tectonics in southwestern Mexico. *J. Geophys. Res.*, 95, (B13), 21931–21948.

Eissler H.K., McNally K.C., 1984, Seismicity and tectonics of the Rivera Plate and implications for the 1932 Jalisco, Mexico, Earthquake. *J. Geophys. Res.,* 89, (B6), 4520–4530.

Geometrics, Inc., 2001, *G-877 Marine Magnetometer 25165-OM Rev. A Operation Manual*, (Geometrics, Inc., San Jose, CA, USA).

Jaramillo S.H., Suárez, G., 2011, The 4 December 1948 Islas Marías, Mexico earthquake (Mw 6.4): reverse faulting beneath the Tres Marias escarpment and implications for the Rivera-North American relative plate motion. *Geofísica Internacional,* 50, 3*,* 313-317*.*

Khutorskoy M.D., Delgado-Argote L.A., Fernández R., Kononov V.I., Polyak B.G., 1994, Tectonics of the offshore Manzanillo and Tecpan basins, Mexican Pacific, from heat flow, bathymetric and seismic data. *Geofísica Internacional,* 33*,* 161-185.

Klitgord K.D., Mammerickx J., 1982, Northern East Pacific Rise: Magnetic anomaly and bathymetric framework. *J. Geophys. Res.,* 87, (B8), 6725–6750.

Kostoglodov V., Bandy W.L., 1995, Seismotectonic constraints on the convergence rate between the Rivera and North American plates. *J. Geophys. Res.,* 100, 17977-17989.

León Soto G., Ni J.F., Grand S.P., Sandvol E., Valenzuela R.W., Guzmán Speziale M., Gómez

González J.M., Domínguez Reyes, T., 2009, Mantle flow in the Rivera-Cocos subduction zone. *Geophys. J. Int.,* 179*,* 1004-1012.

Lonsdale P., 1995, Segmentation and disruption of the East Pacific Rise in the mouth of the Gulf of California. *Marine Geophysical Researches,* 17, 323-359.

Lonsdale P., 1991, Structural patterns of the Pacific floor offshore peninsular California, in *The Gulf and Peninsula Province of the Californias*, American Association of Petroleum Geologists Memoir 47 (ed. Dauphin and Simoneit), AAPG, Tulsa, Oklahoma, pp. 87-125.

Lonsdale P., 1988, Structural pattern of the Galapagos microplate and evolution of the Galapagos triple junction. *J. Geophys. Res.,* 93, 13,551-13,574.

Macdonald K.C., Haymon R.M., Miller S.P., Sempere J.-C., Fox P.J., 1988, Deep-tow and Sea Beam studies of dueling propagating ridges on the East Pacific Rise near 20º40'S. *J. Geophys. Res., 93,* 2875-2898. doi:10.1029/JB093iB04p02875.

Mammerickx J., 1984, The morphology of propagating spreading centers. *J. Geophys. Res.,* 89, 1817-1824.

Mammerickx J., Carmichael I.S.E., 1989, A spreading incursion in the continent near the Rivera plate and Jalisco Block? (abstract). *Eos Trans. Am. Geophys. Union,* 70, 1318-1319.

Mammerickx J., Klitgord K.D., 1982, Northern East Pacific Rise: Evolution from 25 m.y. B.P. to the present. *J. Geophys. Res.,* 87, (B8)*,* 6751–6759.

Michaud, F., and Bourgois, J., 1995, Is the Rivera Fracture Zone a transform fault as currently accepted?. C.R. Acad. Sci. Paris, Série II, 321, 521-528.

Michaud F., Royer J.-Y., Bourgois J., Mercier de Lepinay B., Petit Liaudon G., 1997, the Rivera fracture zone revisited. *Marine Geology,* 137, 207-225.

Michaud F., Dañobeitia J., Carbonell R., Bartolomé R., Cordoba D., Delgado Argote L., Núñez-Cornú F., Monfret T., 2000, New insights into the subducting ocean crust in the Middle American Trench off western Mexico (17º-19ºN). *Tectonophysics,* 318*,* 187-200.

Michaud F., Dañobeitia J., Bartolomé Carbonell R., Delgado Argote L., Cordoba D., Monfret T., 2001, Did the East Pacific Rise subduct beneath the North America Plate (western Mexico)?. *Geo*-Marine *Letters,* 20, 3, 168-173.

Molnar P., 1973, Fault plane solutions of earthquakes and direction of motion in the Gulf of California and on the Rivera Fracture Zone. *GSA Bull.,* 84, 1651-1658.

Nixon G.T., 1982, The relationship between Quaternary volcanism in central Mexico and the seismicity and structure of subducted ocean lithosphere. *GSA Bull.,* 93, (6), 514-523.

Peláez Gavaria J.R., 2008, Análisis de las anomalías magneticas marinas en el limite sur de la placa de Rivera, frente a Colima, Mexico, Thesis, Universidad Nacional Autonoma de Mexico, 122pp.

Pardo M., Suárez G., 1995, Shape of the subducted Rivera and Cocos plates in southern Mexico: Seismic and tectonic implications. *J. Geophys. Res.,* 100, (B7), 12,357–12,373.

Reid I.D., 1976, The Rivera Plate: A Study in Seismology and Plate Tectonics, Ph.D. Dissertation, University of California, San Diego, 288pp.

Schaaf P., Bandy W., Mortera C., Michaud F., Ruffet G., 2009, Mid ocean ridge basalts from the Pacific Rivera Plate, Mexico: Heterogeneous geochemistry and geochronology (abstract), International Lateinamerika-Kolloquium 2009 Abstracts and Program, Göttingen, April 7-9, 255-256.

Serrato–Díaz G., Bandy W.L., Mortera-Gutiérrez C.A., 2004, Active rifting and crustal thinning along the Rivera-Cocos plate boundary as inferred from Mantle Bouguer gravity anomalies. *Geofísica Internacional,* 43, 361-381.

Whitmarsh R.B., Jones M.T., 1969, Daily variation and secular variation of the geomagnetic field from shipboard observations in the Gulf of Aden. *Geophys. J. Int.,* 18, (5), 477–488.

Wilson D.S., 1990, Kinematics of overlapping rift propagation with cyclic rift failure. *Earth and Planetary Science Letters,* 96, (3-4), 384-392.

Yang T., Grand S.P., Wilson D., Guzman-Speciale M., Gómez-González J.M., Domínguez-Reyes T., Ni J., 2009, Seismic structure beneath the Rivera subduction zone from finite-frequency seismic tomography. *J. Geophys. Res.,* 114*,* B01302, doi: 10.1029/2008/JB005830.

Geofísica Internacional (2013) 52-1: 87-92

Original paper

A possible case of Sporadic Aurora in 1843 from Mexico

José Manuel Vaquero*, María Cruz Gallego and Fernando Domínguez-Castro

Received: September 09, 2012; accepted: October 22, 2012; published on line: December 14, 2012

Resumen

Recientemente, algunos autores han mostrado que algunas auroras pueden ser observadas a latitudes relativamente bajas cuando la actividad geomagnética es baja o moderada. Este tipo tan especial de aurora recibe el nombre de "aurora esporádica". Presentamos y analizamos en este trabajo un posible caso de "aurora esporádica" observada desde México el 19 de abril de 1843. Además, estudiamos la actividad solar y auroral alrededor de este evento.

Palabras clave: Aurora esporádica, actividad geomagnética, actividad solar, México, historia de la Geofísica.

Abstract

In recent years, some authors have shown that some auroras can be observed at relatively low latitude when the geomagnetic activity is quiet or moderate. This very special type of aurora is called "sporadic aurora". We present and analyze in this work a possible case of "sporadic aurora" observed in Mexico on the 19 April 1843. Moreover, we study the solar and auroral activity around this event.

Key words: Sporadic aurora, geomagnetic activity, solar activity, Mexico, history of Geophysics.

J.M. Vaquero*
Departamento de Física
Centro Universitario de Mérida
Universidad de Extremadura
Av. Santa Teresa de Jornet, 38
06800 Mérida, España
*Corresponding author: jvaquero@unex.es

M.C. Gallego
Departamento de Física
Universidad de Extremadura
Badajoz, España

F. Domínguez-Castro
Departamento de Física
Universidad de Extremadura
Badajoz, España

Introduction

In general, low-latitude auroras are related to great events of space weather, usually associated with huge Coronal Mass Ejection (CME). Vázquez *et al*. (2006) show that low-latitude aurorae occur mainly in the decaying phase of the solar cycle, as defined by the sunspot number, coinciding with the maximum of the Open Magnetic Field (OMF) that is a better descriptor of the state of the heliosphere. Nowadays, the studies of these episodes are important because they provide additional information on potentially damaging space weather events (Lanzerotti, 2007). In fact, there are some studies of important space weather events in the past. Some of them can be highlighted such as the cases that have occurred on 2 September 1859 (Cliver, 2006; Tsurutani *et al*., 2003; Ribeiro *et al*., 2011), 24–25 October 1870 (Vaquero *et al*., 2008), 25 September 1909 (Silverman, 1995), 14–15 May 1921 (Silverman and Cliver, 2001), and 25 January 1938 (Barlow, 1938; Botley, 1938; Bernhard, 1938; Hess *et al*., 1938).

However, Silverman (2003) provided sufficient data to demonstrate that an auroral phenomenon can be observed at low-latitude under conditions of quiet to moderate magnetic activity. This infrequent phenomenon was called "sporadic aurora" by Silverman (2003) and constitutes a puzzle in magnetospheric physics. Later, Willis *et al*. (2007) demonstrated that at least 29 out of the 42 Chinese and Japanese auroral observations (from 1840 to 1911) occurred at times of weak or moderate geomagnetic activity (*aa* or *Ak* index ≤ 50). Moreover, Vaquero *et al*. (2007) presented a case of "sporadic aurora" observed from Spain on the 29 December 1845.

Therefore, we have some reports of "sporadic aurora" in USA (Silverman, 2003), Asia (Willis *et al*., 2007), and Spain (Vaquero *et al*., 2007) but records of this phenomenon from other places of the world are not available. The aim of this paper is to present a possible case of "sporadic aurora" observed from Mexico on the 19 April 1843.

Historical record

Mexico is a country with an interesting historical and scientific heritage, despite its location far from main centers of scientific research in the 18th and 19th centuries (located generally in European countries as England, France or Germany). Some examples can be cited in the branch of solar physics as the historical sunspot observations preserved in its archives (Vaquero, 2004; Vaquero and Moreno-Corral, 2008) or the records of the great aurora observed in 1789 (Vázquez *et al*., 2006).

The record of an aurora borealis seen from Mexico on 19 April 1843 appears in a book entitled *"Apuntes para la Historia del Gobierno del General D. Antonio López de Santa-Ana"* (Notes for the History of the Government of General Antonio López de Santa Anna) (Bustamente, 1845, p. 136). Full text of this report is reproduced in original ancient Spanish in Appendix. The author of this book was Carlos María de Bustamante (Oaxaca, 4 November 1774 – Ciudad de México, 21 September 1848) a lawyer, journalist and politician. He published several newspapers as *Diario de Mexico, El Juguetillo* or *Correo Americano del Sur* all of them with ideas in favor to the independence. He was member of the parliament by Chilpancingo.

According to this report, Mr. Soyano, professor of philosophy of the Seminary- College, observed a light in the sky to the north on the night of 19 Apri. Despite the weather and clouds, the light was visible. This light was observed from 21:00 to 23:00 approximately (Local Time). Although the clouds did not allow to see its exact form, the observer indicates that it was a semicircle whose center was in the direction NNO1/4. The reporter indicated that it was not the zodiacal light. The phenomenon was not caused by the light of the moon, nor by flashes of lightning. This was clearly an aurora borealis.

Discussion

This record can be associated to a sporadic aurora establishing that the phenomenon was observed under conditions of quiet to moderate magnetic activity and from a low-latitude place.

We would like to compare the date of this aurora observed in Mexico with geomagnetic activity to establish clearly that it is a sporadic aurora. However, note that the more usual magnetic indexes are not availables for early dates. For example, Ak index is only available since 1844 (Nevanlinna and Kataja, 1993; Nevanlinna, 2004) and aa index is only available from 1868 (Mayaud, 1980). Therefore, we can compare the observation date with the geomagnetic IDV index (Svalgaard and Cliver, 2005, 2010), available from 1835, and with some proxies of geomagnetic activity, namely sunspot number and the number of auroras observed at middle latitudes.

Figure 1 shows the Inter-Diurnal Variability (IDV) index from 1835 until 1855 introduced by Svalgaard and Cliver (2005) and improved by Svalgaard and Cliver (2010). IDV is computed as the average difference from one day to the next between hourly mean values of the horizontal component, H (measured one hour after midnight), without regard to sign. The most interesting characteristic of IDV index is that correlate highly with the near heliospheric magnetic field (HMF) strength B. Data provided by Svalgaard and Cliver (2010) shown low

values of the IDV index (and, therefore, low values of the HMF strength B) around the date of observation of the event considered here.

Figure 2 shows the yearly number of auroras observed in middle latitudes according to Křivský and Pejml (1988). Auroral activity during the period 1830-1870 was relatively high with peak values in the years 1830, 1841, 1850, 1859 and 1870 (Figure 2, upper panel). Auroral activity was relatively low in early and late 19th century, corresponding with secular solar activity minima. In the year 1843, auroral activity was low with only 39 auroras observed (Figure 2, lower panel).

As similar picture is obtained from the sunspot numbers (Figure 3). We use two different versions of the sunspot number: International Sunspot Number (Clette *et al*., 2007) and Group Sunspot Number (Hoyt and Schatten, 1998). Figure 3 (upper panel) shows these solar indexes from 1820 to 1860 corresponding to solar cycles 7, 8 and 9. Solar activity around 1843 was low or very low. In October and November 1842, sunspot number values were in the range 30-40. However, the values decrease to10 approximately after December 1842. The values corresponding to April 1843, when the aurora was observed from Mexico, are very low: 9.5 (ISN) and 7 (GSN). Obviously, the low solar activity corresponding to the year 1843 can also be checked in sunspot areas (Vaquero *et al*., 2004).

Long-term variation of the geomagnetic latitude of Mexico for the last two millennia was studied in Vázquez *et al*. (2006) varying between low values of 14º and 30º N. The geomagnetic latitude of México in 1843 was 29.5º N approximately.

Conclusion

We have presented a historical record that clearly describes the aurora borealis seen from Mexico on 19 April 1843. However, geomagnetic, solar and auroral activity during this time was low according to the evolution of the IDV index, sunspot number and the number of auroras observed at middle latitudes respectively. Furthermore, the geomagnetic latitude of Mexico at that time was low (approximately 29.5° N). Therefore, we think that this is a case of "sporadic aurora".

Acknowledgements

Support from the Junta de Extremadura (Research Group Grant No. GR10131) and Ministerio de Economía y Competitividad of the Spanish Government (AYA2011-25945) is gratefully acknowledged.

Appendix

Original text (in ancient Spanish) describing the aurora:

En la noche del 19 de abril observó el Lic. Soyano, catedrático de filosofía de este colegio Seminario, una luz apacible (son sus palabras) cerca de las nueve de la noche por el rumbo del Norte, y á pesar de la obscuridad de la noche y de las nubes, vibraba notablemente. Su duracion, que fué hasta cerca de las once, no me dejó dudar que no era una ilusion, aunque las nubes gruesas impedían ver con exactitud sus contornos, pues sin embargo, se percibia que su figura se acercaba á la del círculo, cuyo centro estaba en el NN. O. 1/4, y cuya mitad inferior ocultaba el orizonte. Ella no podía ser

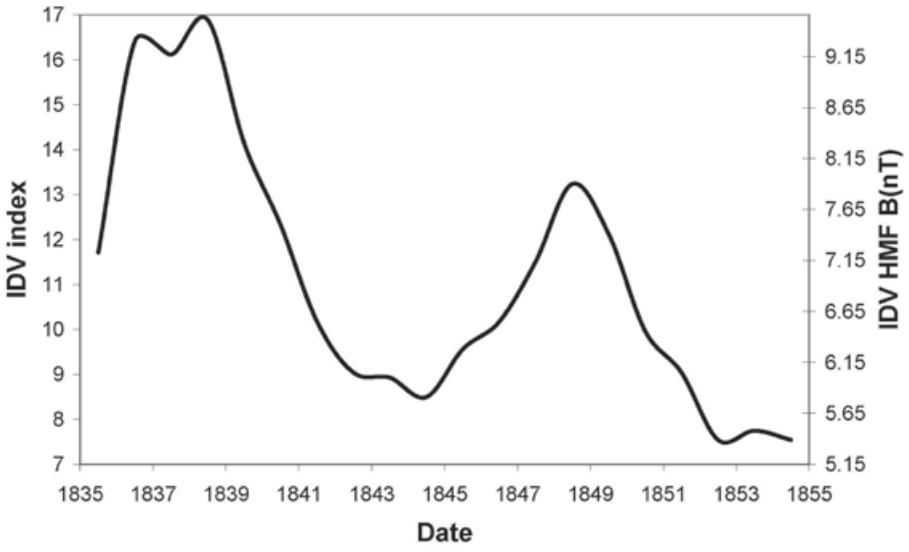

Figure 1. IDV index measured from 1835 until 1855. Right axis indicates the estimated heliospheric magnetic field from IDV index.

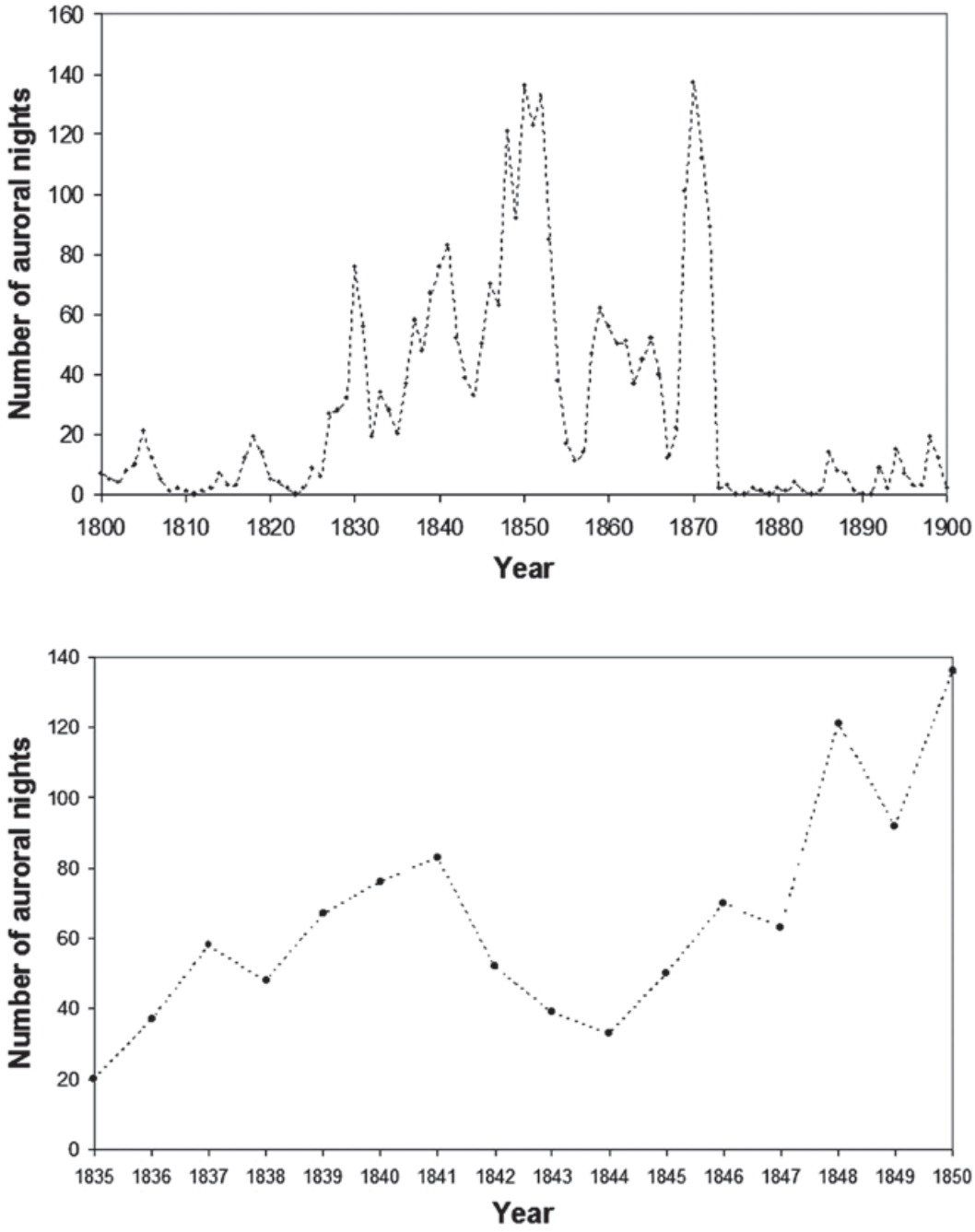

Figure 2. Yearly number of auroras observed in middle latitudes according to Křivský and Pejml (1988) catalogue during the 19th century (upper panel) and the period 1835-1850 (lower panel).

luz zodiacal, pues ni aparece su forma circular, ni por el Norte; tampoco de la luna porque ésta se encontraba oculta, ni causada por los relámpagos, pues estos eran intermitentes y aquella constante; éstos iluminaban todo el cielo, aquella solo el Norte, y tan lejos de causar la impresion en parte para percibirla, resulta que era una aurora boreal. Esta reflexion, y la de que la aurora boreal figura su situacion y sus vibraciones, convienen cabalmente á la letra con las de todos los fisicos estar de acuerdo cuando la describen, y todo ello me induce á creer que fué una verdadera aurora boreal.

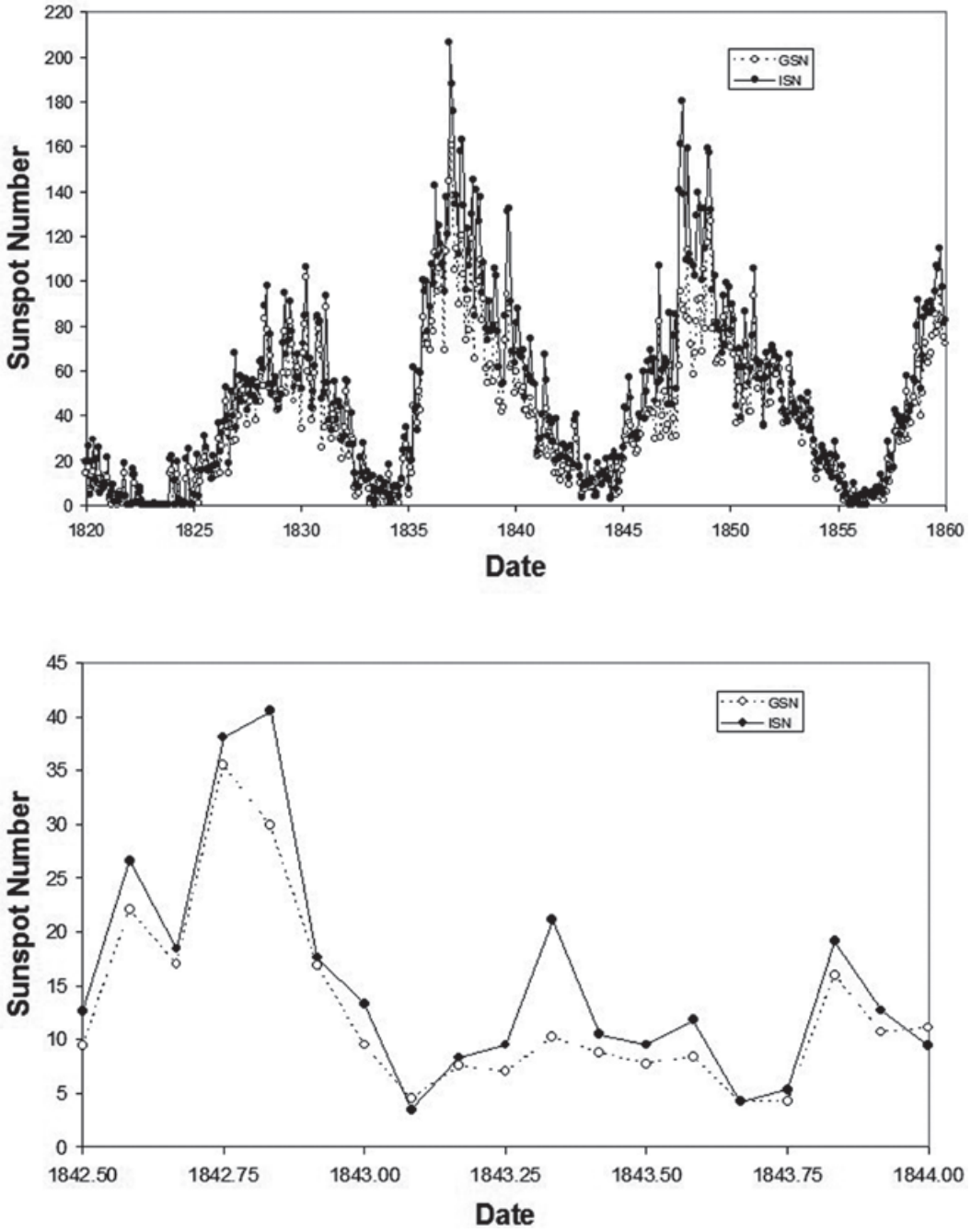

Figure 3. Monthly sunspot numbers from 1820 to 1860 (upper panel) and July 1842 - January 1844 (lower panel).

Bibliography

Barlow E.W., 1938, The auroral display of January 25–26, 1938, Q. J. R. Meteorol. Soc., 63, 215–219.

Bernhard H.J., 1938, Northern lights come south, The Sky, 2, 10.

Botley C.M., 1938, Some human reactions to the great aurora of January 25– 26, 1938, Q. J. R. Meteorol. Soc., 63, 449– 450.

Bustamente C.M. de, 1845, Apuntes para la historia del Gobierno del General D. Antonio López Santa-Ana (Mexico: Imprenta de J. M. Lara).

Clette F., Berghmans D., Vanlommel P., Van der Linden R.A.M., Koeckelenbergh A., Wauters L., 2007, From the Wolf number to the International Sunspot Index: 25 years of SIDC. *Adv. Space Res*, 40, 919–928.

Cliver E.W., 2006, The 1859 space weather event: Then and now, *Adv. Space Res*., 38, 119–129.

Hess V.F., Steinmaurer R., Demmelmair A., 1938, Cosmic rays and the aurora of January 25–26, *Nature*, 141, 686–687.

Hoyt D.V., Schatten K.H., 1998, Group sunspot numbers: A new solar activity reconstruction, *Sol. Phys*., 179, 189– 219.

Křivský L., Pejml K., 1988, Solar Activity, Aurorae and Climate in Central Europe in the last 1000 Years. Publications of the Astronomical Institute of the Czechoslovak Academy of Sciences Publication No. 75.

Lanzerotti L., 2007, Value of historical space weather events, Space Weather, 5, S06005, doi:10.1029/2007SW000342.

Mayaud P.N., 1980, Derivation, Meaning, and Use of Geomagnetic Indices, Geophysical Monograph 22, American Geophysical Union, Washington, D.C.

Nevanlinna H., 2004, Results of the Helsinki magnetic observatory 1844–1912, Annales Geophysicae, 22, 1691–1704.

Nevanlinna H., Kataja E., 1993, An extension of the geomagnetic activity index series aa for two solar cycles (1844–1868), *Geophys. Res. Lett.*, 20, 2703–2706.

Ribeiro P., Vaquero J.M., Trigo R.M., 2011, Geomagnetic records of Carrington's storm from Guatemala, *J. Atmos. Sol. Terr. Phys*, 73, 308–315.

Silverman S.M., 1995, Low latitude auroras: The storm of 25 September 1909, *J. Atmos. Terr. Phys*., 57, 673– 685.

Silverman S.M., Cliver E.W., 2001, Low-latitude auroras: The magnetic storm of 14 – 15 May 1921, *J. Atmos. Sol. Terr. Phys*., 63, 523– 535.

Silverman S.M., 2003, Sporadic auroras, *J. Geophys. Res*., 108, A4, 8011, doi: 10.1029/2002JA009335.

Svalgaard L., Cliver E.W., 2005, The IDV index: Its derivation and use in inferring long-term variations of the interplanetary magnetic field strength, J. Geophys. Res., 110, A12103, doi:10.1029/2005JA011203.

Svalgaard L., Cliver E.W., 2010, Heliospheric magnetic field 1835–2009, *J. Geophys. Res*., 115, A09111, doi:10.1029/2009JA015069.

Tsurutani B.T., González W.D., Lakhina G.S., Alex S., 2003, The extreme magnetic storm of 1 – 2 September 1859, *J. Geophys. Res*., 108, A7, 1268, doi:10.1029/2002JA009504.

Vaquero J.M., 2004, On the solar activity during the year 1784, *Solar Physics*, 219, 379-384.

Vaquero J.M., Gallego M.C., Sánchez-Bajo F., 2004, Reconstruction of a monthly homogeneous sunspot area series since 1832, *Solar Physics,* 221, 1, 179-189.

Vaquero J.M., Moreno-Corral M.A., 2008, Historical Sunspot Records from Mexico, *Geofísica Internacional* 47, 189-192.

Vaquero J.M., Trigo R.M., Gallego M.C., 2007, Sporadic aurora from Spain, *Earth Planets Spac*e, 59, e49–e51.

Vaquero J.M., Valente M.A., Trigo R.M., Ribeiro P., Gallego M.C., 2008, The 1870 space weather event: Geomagnetic and auroral records, *J. Geophys. Res*., 113, A08230, doi:10.1029/2007JA012943.

Vázquez M., Vaquero J.M., Curto J.J., 2006, On the Connection between Solar Activity and Low-Latitude Aurorae in the Period 1715–1860, Solar Physics 238, 405–420.

Willis D.M., Stephenson F.R., Fang H., 2007, Sporadic aurorae observed in East Asia, Annales Geophysicae, 25, 417–436.